# NAVAL POSTGRADUATE SCHOOL
## Monterey, California


# THESIS

NUMERICAL SIMULATION OF ATMOSPHERIC FLOW ON VARIABLE GRIDS USING THE GALERKIN FINITE ELEMENT METHOD

by

Donald E. Hinsman

March 1983

Thesis Advisor: R. T. Williams

UNCLASSIFIED

SECURITY CLASSIFICATION OF THIS PAGE (When Date Entered)

| REPORT DOCUMENTATION PAGE | | READ INSTRUCTIONS BEFORE COMPLETING FORM |
|---|---|---|
| 1. REPORT NUMBER | 2. GOVT ACCESSION NO. | 3. RECIPIENT'S CATALOG NUMBER |
| 4. TITLE (and Subtitle)<br>Numerical Simulation of Atmospheric Flow on Variable Grids Using the Galerkin Finite Element Method | | 5. TYPE OF REPORT & PERIOD COVERED<br>Doctoral Dissertation; March, 1983<br>6. PERFORMING ORG. REPORT NUMBER |
| 7. AUTHOR(s)<br>Donald E. Hinsman | | 8. CONTRACT OR GRANT NUMBER(s) |
| 9. PERFORMING ORGANIZATION NAME AND ADDRESS<br>Naval Postgraduate School<br>Monterey, CA 93940 | | 10. PROGRAM ELEMENT, PROJECT, TASK AREA & WORK UNIT NUMBERS |
| 11. CONTROLLING OFFICE NAME AND ADDRESS<br>Naval Postgraduate School<br>Monterey, CA 93940 | | 12. REPORT DATE<br>March, 1983<br>13. NUMBER OF PAGES<br>143 |
| 14. MONITORING AGENCY NAME & ADDRESS(if different from Controlling Office) | | 15. SECURITY CLASS. (of this report)<br>UNCLASSIFIED<br>15a. DECLASSIFICATION/DOWNGRADING SCHEDULE |

16. DISTRIBUTION STATEMENT (of this Report)

Approved for public release, distribution unlimited.

17. DISTRIBUTION STATEMENT (of the abstract entered in Block 20, if different from Report)

18. SUPPLEMENTARY NOTES

19. KEY WORDS (Continue on reverse side if necessary and identify by block number)

Galerkin Finite Element Method, variable grid, triangular subdivision, rectangular subdivision, moving finite elements, small-scale forcing

20. ABSTRACT (Continue on reverse side if necessary and identify by block number)

A hypothesis is made that the Galerkin Finite Element Method (GFEM) offers a viable option to the traditional Finite Difference Method (FDM) for numerical weather prediction. The shallow water barotropic primitive equations are the forecast equations for all experiments. The hypothesis is tested by observing simple, analytic atmospheric wave propagation on

DD FORM 1473 EDITION OF 1 NOV 65 IS OBSOLETE

20. Abstract (continued)

uniform and variable mesh grids. Second, a strongly forced solution simulating small scale nonlinear interactions is evaluated for both the GFEM and FDM. Finally, a variable, moving grid for a GFEM model is compared to a uniform, higher resolution GFEM model for a strong vortex in a mean flow. The GFEM shows a better propagation for simple atmospheric waves and better prediction to a forced nonlinear solution than the FDM model. A moving variable grid follows an area of strong gradients while not generating noise in the transition zone.

Approved for public release, distribution unlimited.

# Numerical Simulation of Atmospheric Flow on Variable Grids Using the Galerkin Finite Element Method

by

Donald E. Hinsman
Commander, United States Navy
B.S., U.S. Naval Academy, 1968
M.S., Naval Postgraduate School, 1975

Submitted in partial fulfillment of the
requirements for the degree of

DOCTOR OF PHILOSOPHY

from the

NAVAL POSTGRADUATE SCHOOL
March 1983

## ABSTRACT

A hypothesis is made that the Galerkin Finite Element Method (GFEM) offers a viable option to the traditional Finite Difference Method (FDM) for numerical weather prediction. The shallow water barotropic primitive equations are the forecast equations for all experiments. The hypothesis is tested by observing simple, analytic, atmospheric wave propagation on uniform and variable mesh grids. Second, a strongly forced solution simulating small scale nonlinear interactions is evaluated for both the GFEM and FDM. Finally, a variable, moving grid for a GFEM model is compared to a uniform, higher resolution GFEM model for a strong vortex in a mean flow. The GFEM shows a better propagation for simple atmospheric waves and better prediction to a forced nonlinear solution than the FDM model. A moving variable grid follows an area of strong gradients while not generating noise in the transition zone.

TABLE OF CONTENTS

LIST OF TABLES

LIST OF FIGURES

ACKNOWLEDGMENTS

I wish to thank everyone involved in supporting me during my studies. In particular, I want to thank the United States Navy for selecting me to attend the Naval Postgraduate School in the Doctoral Studies Program. My mentor, Dr. Terry Williams, has placed his faith in me, guiding me through this long process and to him I owe unending words of thanks. My Doctoral Committee has been a source of consultation and encouragement and I am very proud to have had each of them on my committee. Dr. Andrew Staniforth (Recherche en Prevision Numerique, Atmospheric Environment Service, Dorval, Quebec) dedicated much time and knowledge and his thoughts greatly aided me in bringing this dissertation to fruition. To those who have preceded me here at the Naval Postgraduate School in the finite element research, Richard Kelley, Mark Older and Edward Woodward, I want to thank for leaving a legacy of accomplishment. Additionally, thanks are extended to Dr. Frank Winninghoff who coded and ran the finite difference model.

Three friends have greatly influenced me during my studies and a special thanks is most appropriate. Mr. Pat Gallacher was my sounding board and computer expert whenever I needed him, and without his efforts I would never have finished on time. My closest friend, Major Jack Hayes, was

my alterego. Together we studied, together we took exams and together we passed. It would never have been possible without Jack. Finally, I want to give my love to my wife who has unselfishly supported me. She typed this manuscript. She has been my guiding light throughout my life. Her overwhelming zeal for life has been my inspiration and to her I dedicate this dissertation.

# I. INTRODUCTION

Proper simulation of atmospheric flow is the main objective of numerical weather prediction. The foundation of numerical weather prediction is a set of equations including the momentum, thermodynamic, moisture and continuity equations for modeling the atmosphere. Through computer simulation, numerical weather prediction predicts a future state based on initial conditions describing the atmosphere. A successful forecast model must include small scale processes. Transports, conversions and exchanges of mass, momentum and energy occurring on the small scale represent important features which must be properly simulated. Feedbacks from the proper representation of these small features can sometimes markedly influence the larger scale solutions. Representation of the effects of small scale processes can be accomplished directly through increased spatial resolution. Continued increases in the spatial resolution will eventually allow the desired process to be resolved properly. However, a doubling of resolution generally requires an eight fold increase in computational effort. The value of increased spatial resolution must ultimately be measured by its contribution to the overall forecast. A level of confidence in the forecast must be achieved that the process is resolved near that particular

grid resolution. The grid resolution could be uniformly fine in the forecast domain. The computational effort for uniform fine mesh models could be far in excess of available resources. An alternative to a uniform fine mesh is a variable mesh where the fine mesh covers only regions of interest or high activity.

The conventional numerical weather prediction forecast scheme, the finite difference method, approximates the partial differential equations with a truncated Taylor series. It has performed admirably when forecasting the larger scales of motion. Technological improvements in computing power coupled with better understanding of the atmosphere now allow the smaller scales to be forecast.

An alternate method for numerical weather prediction, the GFEM approximates the partial differential equations while minimizing the error between the actual equations and their approximation. This best fit logically leads one to the expectation that the GFEM will better model the smaller scales than the finite difference schemes. This research will demonstrate practical aspects of the GFEM theoretically possible.

In this dissertation, the GFEM will be evaluated to determine its potential to model atmospheric flow. Equivalent GFEM and FDM models will be utilized to compare the two methods. Simulations of small scale processes explicitly resolved on uniform and variable grids will be investigated.

Rigorous experiments will demonstrate both GFEM and FDM responses for forcing near the grid length scale. Finally, a demonstration will be made of a GFEM moving variable mesh which moves with the small scale process or feature, and thereby allows the fine mesh to resolve the highly active region initially and throughout the forecast period.

## II. HYPOTHESIS

Numerical weather prediction has steadily improved in the simulation of atmospheric flow. Large scale flows have been adequately represented by finite difference models for several decades. Galerkin-type formulations (Cullen, 1974b; Hinsman, 1975; Staniforth and Mitchell, 1978; Cullen and Hall, 1979; Staniforth and Daley, 1979; MacPherson and Aksel, 1980; and Sasaki and Reddy, 1980) have been shown to be competitive with finite difference models, but have not shown a marked improvement. Comparing the current operational models at selected large computer centers, one finds that two are Galerkin and three are finite difference (Galerkin: National Meteorological Center and Canadian Meteorological Center; and finite difference: Fleet Numerical Oceanography Center, Air Force Global Weather Center and European Center for Medium Range Weather Forecasting. However, all centers have ongoing research with Galerkin models and there are indications that these will give better long range forecasts. The dichotomy arises because the Galerkin applications have not vindicated themselves with a marked increase in accuracy, but rather have shown equivalent accuracies. Staniforth and Mitchel (1977) stated that ultimately the best global/hemispheric models will be a spectral model. The spectral model is based on

the Galerkin procedure and the use of trigonometric functions is particularly appealing for hemispheric or global grids. However, where non-uniform grids are required, the GFEM is a more logical choice.

Marked improvements in regional forecasts will not come from better large-scale models, but rather from models that can simulate smaller atmospheric features. The National Weather Service Limited Fine Mesh Model is an improvement over the hemispheric model, partly because it has higher resolution and can resolve smaller phenomena. These smaller features can also affect the large scale flow. Numerical meteorologists have realized this for years and have attempted to model these features.

The GFEM has the potential to increase efficiently the spatial resolution for the purpose of simulating accurately the small-scale processes. If a variable mesh is to be employed, then it should be evaluated by proper simulation of a small-scale feature. In previous research (Staniforth and Mitchell, 1978), the refined grid was tested by propagating synoptic-scale waves into the finer grid and demonstrating that the wave could move into the finer grid without generation of significant noise. These conditions represent a prerequisite. If synoptic-scale waves cannot move freely into and through the variable grid, then advection interactions will not occur properly in the fine grid.

However, one must also show that a smaller scale atmospheric feature can be properly resolved or developed in the fine mesh area. This will be a milestone. The efforts of Staniforth and Mitchell (1978) and Staniforth and Daley (1979) have stressed the movement of synoptic scale features into the fine mesh area but have not demonstrated improved resolution of smaller scale atmospheric features in the fine mesh area.

The hypothesis is that the GFEM is a viable option for numerical weather prediction when simulating atmospheric flow on variable grids. Three separate features of the GFEM will be explored. Each feature will establish the credentials of the GFEM as a viable option. Each feature is intimately related to the proper representation of a small-scale phenomenon. The cost effectiveness of the GFEM, when evaluated in these contexts, will provide a measure of the potential contribution of the method.

## A. FEATURES

The following three specific features will be explored to support the hypothesis.

### 1. Variable Grid

Investigations of a suitable alternative to the finite difference models for a variable grid will be performed. Two basic subdivisions are available--triangular or rectangular. Staniforth and Mitchell (1978) employed the

variable rectangular grid as shown in Figure 1. The grid contained some areas of finer resolution which were not in the verification area. Two points associated with having variable resolution in peripheral regions arise:

(a) Unnecessary computational overhead is required; and

(b) Undesirable phase changes occur as the wave propagates in the peripheral regions.

Older (1981) and Woodward (1981) developed a transformation procedure to vary smoothly the resolution for a channel domain from a coarse to a fine area in a triangular subdivision. A uniform equilateral subdivision is shown in Figure 2. The use of triangles allows the increased resolution to occur only where desired and not in peripheral regions. Two possible choices of triangles include the right and the equilateral. Hinsman (1975) utilized equilateral triangles while Cullen (1974b) utilized near-equilateral triangles. Both reported excellent wave propagation. Kelley and Williams (1976) utilized right triangles and experienced very noisy solutions. Woodward (1981) duplicated Kelley and Williams effort with equilateral triangles and found a major reduction in the noise.

The differing geometries and results thus far reported mandate a further review of triangular subdivisions. It is not obvious which subdivision is most suitable. A distinct advantage of the rectangular subdivision is that it allows

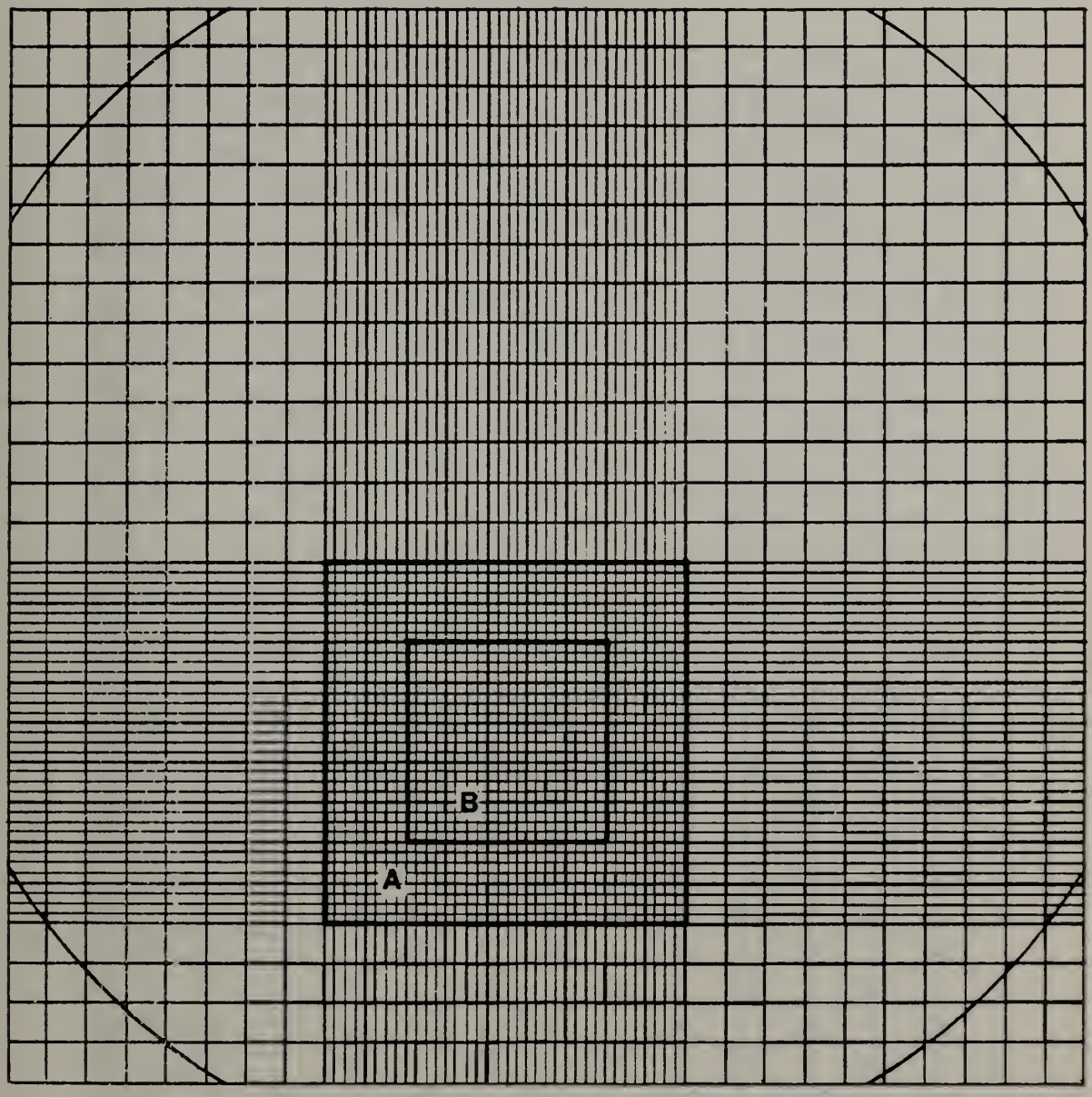


Fig. 1. Rectangular subdivision of the Northern Hemisphere on a polar stereographic projection (Staniforth and Mitchell, 1978).

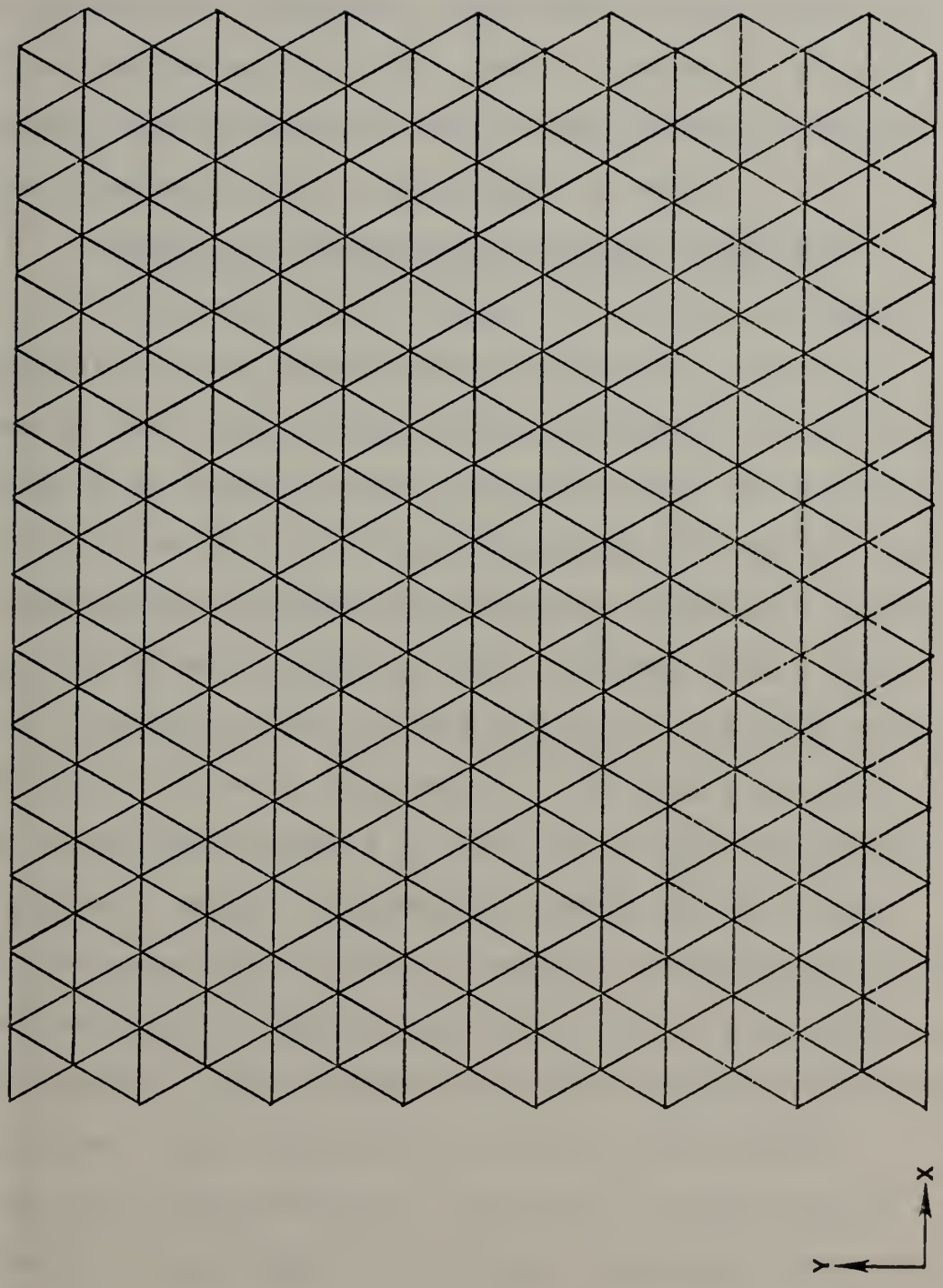


Fig. 2. Triangular subdivision for a channel in Cartesian coordinates (Woodward, 1981).

algorithms to be developed which take full advantage of vector processors. However, both subdivisions afford the luxury of obtaining a variable grid. Therefore, similar experiments performed on each type subdivision will point out the advantages and disadvantages of each.

2. Numerical Simulation of Physical Processes

The variable grid chosen as the most suitable alternative will be tested while simulating a physical process to show that a small-scale atmospheric feature can be properly portrayed in the fine mesh area. As stated in Chapter II, the ability of variable grids to resolve small scale atmospheric features has not been rigorously tested. The ability to move synoptic scale features into a finer mesh is a prerequisite and must be shown. The main crux of the problem is what is happening in the fine mesh area. A proper scheme must resolve a small scale feature near the smallest grid length. Schoenstadt (1980) and Williams (1981) indicated that the most responsive schemes were either a staggered finite element grid with primitive variables or an unstaggered finite element grid with vorticity/divergence formulation. This research will utilize the latter.

The simulated process will be that of a mass source analogous to that found in the upper atmosphere above a hurricane or on the leading side of a strong trough. The source will appear in the continuity equation. A known wave

form will be assumed and the required source to support the wave form will be analytically derived. The expression for the wave form will allow control of the scale of the process so that a near-grid scale phenomena can be simulated.

3. Moving Grid

The ability to move the fine grid so that it remains centered on an atmospheric circulation will also be demonstrated. This capability will further enhance the applicability of the GFEM for atmospheric simulation. If it is shown that small-scale forcings are properly reflected in the flow, and the grid can be moved with the forcing disturbance, then the GFEM has great potential for atmospheric prediction.

# III. THE DEVELOPMENT OF THE GFEM

The hypothesis in Chapter II proclaims the GFEM as a viable option for simulating atmospheric flow. An understanding of the history and principles of the GFEM will give further insight for the expected improved performance as compared to the conventional FDM.

The origin of the GFEM can be traced to the seventeenth century work by Leonhard Euler. His work established the branch of mathematics known as calculus of variation. He recognized that there existed a partial differential equation (PDE) associated with the minimization of a functional. This PDE has been appropriately named the Euler-Lagrange equation. Solving the PDE was equivalent to determining a stationary value of the functional. In the late nineteenth century, Lord Rayleigh furthered the variational calculus by representing the dependent variable as a mathematical expression, typically as a power series. The stationarity of the solution allowed determination of the unknown coefficients of the power series. His work was generalized in the early twentieth century by W. Ritz and the procedure has since been referred to as the Rayleigh-Ritz method. A limitation in the solution by the Rayleigh-Ritz method is the fullness of the matrix to be inverted. Shortly after Ritz completed his work, Galerkin developed a procedure

using weighted residuals which had a wider application than classical variational calculus. The residual is made orthogonal to a function, called the test function, and thereby is minimized. While the Rayleigh-Ritz procedure applies to the functional of an associated Euler-Lagrange equation, the Galerkin procedure pertains to any PDE. The methods produce identical results when applied to equivalent extremum problems.

The Galerkin procedure was unknowingly well established by the end of World War II. The rapid technological advances made during and after the war, coupled with the emergence of the computer, led the aircraft industry to develop new numerical procedures for solving stress problems in aircraft design. A successful technique was developed and mathematicians realized, long after the fact, that the Galerkin procedure was being utilized.

The GFEM is a commonly used subset of the set of Galerkin procedures. After subdivision into a set of elements, the domain resembles a completed jigsaw puzzle, and hence leads to the terminology "finite elements." Figures 1 and 2 are samples of such subdivisions. The dependent variables of the PDE are represented as a linear combination of known functions, which are usually low order polynomials. The same function is employed as the test function. When substituted into the PDE, these approximations leave a residual. Minimizing the residual completes the procedure.

The functions are globally zero except where the dependent variables are defined near each individual node. The product of functions remains zero except where the representing and test functions are both non-zero. This makes the method attractive for computer implementation. It removes the matrix "fullness" problem found with the Rayleigh-Ritz approach. The minimization process lies at the heart of the expected improved performance. Each term of the PDE has been simultaneously approximated and the error in those approximations has been minimized.

# IV. MODEL DESCRIPTION

Two different barotropic shallow-water models will be employed to test the hypothesis in Chapter II. Each model will have the identical domain, boundary and initial conditions. The difference will lay with the partial differential equation approximation. In one model, a Galerkin approximation to the partial differential equation will be used, while the other model will use a finite difference approximation. Two versions of the Galerkin model will be evaluated. The first version will have triangular subdivisions and basis functions, while the other will have rectangular subdivisions and basis functions.

## A. GALERKIN FINITE ELEMENT MODEL

The system of equations referred to as the shallow-water equations consists of three equations with three forecast variables $\phi$, u and v. The equations are written

$$\frac{\partial \phi}{\partial t} + u\frac{\partial \phi}{\partial x} + v\frac{\partial \phi}{\partial y} + \phi\left(\frac{\partial u}{\partial x} + \frac{\partial v}{\partial y}\right) = 0 \qquad (4\text{-}1)$$

$$\frac{\partial u}{\partial t} + u\frac{\partial u}{\partial x} + v\frac{\partial u}{\partial y} - fv + \frac{\partial \phi}{\partial x} = 0 \qquad (4\text{-}2)$$

$$\frac{\partial v}{\partial t} + u\frac{\partial v}{\partial x} + v\frac{\partial v}{\partial y} + fu + \frac{\partial \phi}{\partial y} = 0 \qquad (4\text{-}3)$$

Here $\phi$ is the geopotential height,

u is the east/west component of the wind,

v is the north/south component of the wind, and

f is the Coriolis parameter

By expanding $\phi$ into a mean ($\Phi$) and a deviation ($\phi'$) the equations can be written

$$\frac{\partial \phi'}{\partial t} + \Phi D + \frac{\partial}{\partial x}(u\phi') + \frac{\partial}{\partial y}(v\phi') = 0 \qquad (4\text{-}4)$$

$$\frac{\partial u}{\partial t} + \frac{\partial \phi'}{\partial x} + \frac{\partial K}{\partial x} - vQ = 0 \qquad (4\text{-}5)$$

$$\frac{\partial v}{\partial t} + \frac{\partial \phi'}{\partial y} + \frac{\partial K}{\partial y} + uQ = 0 \qquad (4\text{-}6)$$

here D is the divergence

K is the kinetic energy (per unit mass), and

Q is the absolute vorticity.

The primes will be dropped for the rest of the paper for clarity.

Cullen and Hall (1979) showed that the accuracy of the GFEM solution was better for the vorticity-divergence formulation of the shallow-water equations than for an increase in resolution with the primitive formulation. Williams and Schoenstadt (1980) noted that staggered variable formulation of the primitive equations and the unstaggered vorticity-divergence formulation gave the best treatment of geostrophic adjustment for small-scale features.

The vorticity-divergence form of the shallow-water equations also allows the use of a semi-implicit time scheme. This scheme artificially slows the propagation speed of the fastest gravity waves, which allows a much larger time step than one could expect for a normal Courant-Fredrich-Lewy (CFL) stability criterion. This scheme thus offsets some of the extra computational expense required to solve the system of equations assembled at each time step.

The vorticity/divergence form of the equations is

$$\frac{\partial \phi}{\partial t} + \phi D + \frac{\partial}{\partial x}(u\phi) + \frac{\partial}{\partial y}(v\phi) = 0 \qquad (4\text{-}7)$$

$$\frac{\partial \zeta}{\partial t} + \frac{\partial}{\partial x}(uQ) + \frac{\partial}{\partial y}(vQ) = 0 \qquad (4\text{-}8)$$

$$\frac{\partial D}{\partial t} + \nabla^2\phi + \nabla^2 K - \frac{\partial}{\partial x}(vQ) + \frac{\partial}{\partial y}(uQ) = 0 \qquad (4\text{-}9)$$

Here $\nabla^2$ is the Laplacian operator and $\zeta$ is the $(\frac{\partial v}{\partial x} - \frac{\partial u}{\partial y})$ relative vorticity.

The velocity can be written as the sum of the rotational and irrotational components as

$$\underset{\sim}{V} = \underset{\sim}{V}_\psi + \underset{\sim}{V}_\chi$$

where $\underset{\sim}{V}_\psi = \underset{\sim}{K} X \nabla\psi$ and $\underset{\sim}{V}_\chi = \nabla\chi$

The equations can be rewritten using

$$D = \frac{\partial u}{\partial x} + \frac{\partial v}{\partial y} = \nabla^2\chi$$

and

$$\zeta = \frac{\partial v}{\partial x} - \frac{\partial u}{\partial y} = \nabla^2\psi$$

resulting in

$$\frac{\partial \phi}{\partial t} + \Phi \nabla^2 \chi = - \frac{\partial}{\partial x}(u\phi) - \frac{\partial}{\partial y}(v\phi) \qquad (4\text{-}10)$$

$$\frac{\partial}{\partial t}\nabla^2 \psi = - \frac{\partial}{\partial x}(uQ) - \frac{\partial}{\partial y}(vQ) \qquad (4\text{-}11)$$

$$\frac{\partial}{\partial t}\nabla^2 \chi + \nabla^2 \phi = \frac{\partial}{\partial x}(vQ) - \frac{\partial}{\partial y}(uQ) - \frac{\partial}{\partial x}\frac{\partial K}{\partial x} - \frac{\partial}{\partial y}\frac{\partial K}{\partial y} \qquad (4\text{-}12)$$

Equation (4-12) can be further manipulated

$$\nabla^2\left(\frac{\partial \chi}{\partial t} + \phi\right) = \frac{\partial}{\partial x}\left((vQ) - \frac{\partial K}{\partial x}\right) - \frac{\partial}{\partial y}\left((uQ) + \frac{\partial K}{\partial y}\right) \qquad (4\text{-}13)$$

The domain of integration is a channel with east-west periodicity. The boundary condition at a wall is

$$\underset{\sim}{V} \cdot \underset{\sim}{N} = 0$$

where $\underset{\sim}{N}$ is an outward pointing normal vector. Along the northern and southern walls, the v component is equal to zero, so that the v equation of motion (4-3) reduces to

$$\frac{\partial \phi}{\partial y} = - fu$$

The zonal and meridional components of the wind can be written as non-divergent and irrotational components as

$$u = - \frac{\partial \psi}{\partial y} + \frac{\partial \chi}{\partial x}$$

and

$$v = \frac{\partial \psi}{\partial x} + \frac{\partial \chi}{\partial y}$$

Then, along the north/south walls where v equals zero, the boundary condition is

$$\frac{\partial \psi}{\partial x} + \frac{\partial \chi}{\partial y} = 0 \qquad (4\text{-}14)$$

The above condition is imposed by setting

$$\psi = \text{a constant} \tag{4-15}$$

when solving the vorticity equation and

$$\frac{\partial \chi}{\partial y} = 0 \tag{4-16}$$

when solving the divergence equation. This is an overspecification but (4-14) would be difficult to apply. The initial conditions which will be presented later are specifically selected to satisfy (4-15) and (4-16).

The semi-implicit scheme is implemented by evaluating all the terms on the left hand side of the equations as an average at time levels $(t + \Delta t)$ and $(t - \Delta t)$ or with a centered time difference as appropriate. All the terms on the right hand side are evaluated at time level t. The equations become

$$\frac{\partial \phi}{\partial t} + \Phi(\nabla^2 \chi(t+\Delta t) + \nabla^2 \chi(t-\Delta t)) = -\frac{\partial}{\partial x}(uQ) - \frac{\partial}{\partial y}(vQ) \tag{4-17}$$

$$\nabla^2 \frac{\partial \psi}{\partial t} = -\frac{\partial}{\partial x}(uQ) - \frac{\partial}{\partial y}(vQ) \tag{4-18}$$

$$\nabla^2\left(\frac{\partial \chi}{\partial t} + \phi(t+\Delta t) + \phi(t-\Delta t)\right) = \frac{\partial}{\partial \chi}((vQ) - \frac{\partial K}{\partial x}) - \frac{\partial}{\partial y}((uQ) + \frac{\partial K}{\partial y}) \tag{4-19}$$

The divergence equation (4-19) can be solved for $\chi$ at $(t + \Delta t)$ and substituted into the equation (4-17) to yield

$$\nabla^2 \bar{\phi} - \frac{\bar{\phi}}{\Phi(\Delta t)^2} = \frac{\partial}{\partial x}((vQ) - \frac{\partial K}{\partial x}) - \frac{\partial}{\partial y}((uQ) + \frac{\partial K}{\partial y})$$
$$- \frac{\phi(t-\Delta t)}{\Phi(\Delta t)^2} + \frac{1}{\Delta t} \nabla^2 \chi(t-\Delta t) + \frac{1}{\Phi \Delta t}\left(\frac{\partial}{\partial x}(\phi u) + \frac{\partial}{\partial y}(\phi v)\right) \tag{4-20}$$

where the overbar denotes an average of $t + \Delta t$ and $t - \Delta t$. The system of three equations in three unknowns has been reduced to two Poisson equations and one Helmholtz equation to be solved at each time step.

The solution procedure involves solving the $\phi$ equation (4-20) for a new $\bar{\Phi}$. The divergence equation (4-19) is then solved for $\bar{\Phi} + \frac{\partial \chi}{\partial t}$ and by subtraction for $\frac{\partial \chi}{\partial t}$. Finally, the vorticity equation (4-18) is solved for $\frac{\partial \psi}{\partial t}$. There are two options as to which variables will be history-carrying: either $\phi$, $\psi$ and $\chi$ or $\phi$, u and v. The choice was made to use $\phi$, u and v as history-carrying variables. They are updated after each time step following Staniforth and Mitchell (1977) by

$$\phi(t+\Delta t) = 2\bar{\phi} - \phi(t-\Delta t) \tag{4-21}$$

$$u(t+\Delta t) = 2\Delta t\left(\frac{\partial}{\partial x}\frac{\partial \chi}{\partial t} - \frac{\partial}{\partial y}\frac{\partial \psi}{\partial t}\right) + u(t-\Delta t) \tag{4-22}$$

$$v(t+\Delta t) = 2\Delta t\left(\frac{\partial}{\partial y}\frac{\partial \chi}{\partial t} + \frac{\partial}{\partial x}\frac{\partial \psi}{\partial t}\right) + v(t-\Delta t) \tag{4-23}$$

Implementation of the GFEM is accomplished as described in Chapter III. The north and south latitudes are input parameters, and the north/south distance is subdivided into N equal parts, where N is also an input parameter. The east/west increment is a function of the north/south increment, as explained in the section describing the individual

experiments. The Coriolis parameter will be a constant equal to the mid-channel value.

The triangular and rectangular domain subdivisions will be demonstrated in the experiment sections. An appropriate approximating function for the rectangular subdivision is a bilinear function. In either case, the forecast equations in Galerkin form are

$$\int(\nabla^2\bar{\phi}_j V_j - \frac{\bar{\phi}_j V_j}{\Phi(\Delta t)^2})V_i = \int(\frac{\partial}{\partial x}((vQ)_j V_j - \frac{\partial}{\partial x} K_j V_j))V_i$$

$$- \int(\frac{\partial}{\partial y}((uQ)_j V_j + \frac{\partial}{\partial y} K_j V_j))V_i + \int \frac{1}{\Phi\Delta t}(\frac{\partial}{\partial x}(\phi u)_j V_j + \frac{\partial}{\partial y}(\phi v)_j V_j)V_i$$

$$- \int \frac{\phi_j}{\Phi(\Delta t)^2}(t-\Delta t)V_j V_i + \int \frac{1}{\Delta t}\nabla^2\chi_j(t-\Delta t)V_j V_i \qquad (4\text{-}24)$$

$$\int \nabla^2 \frac{\partial \psi}{\partial t}{}_j V_j V_i = - \int(\frac{\partial}{\partial x}(uQ)_j V_j)V_i - \int(\frac{\partial}{\partial y}(vQ)_j V_j)V_i \qquad (4\text{-}25)$$

$$\int \nabla^2(\frac{\partial}{\partial t} \chi_j V_j + \bar{\phi}_j V_j)V_i = \int(\frac{\partial}{\partial x}((vQ)_j V_j - \frac{\partial K}{\partial x}{}_j V_j))V_i$$

$$- \int(\frac{\partial}{\partial y}((uQ)_j V_j + \frac{\partial K}{\partial y}{}_j V_j))V_i \qquad (4\text{-}26)$$

Here the integral sign implies an area integral over the domain, the j subscript denotes Einstein summation for the dependent variables and the i subscript is the ith nodal equation.

The strength of the GFEM is that the spatial derivatives of the dependent variables become derivatives of the known approximating function and, therefore, are known exactly at each node. When using piecewise continuous linear functions, the first derivatives are piecewise discontinuous and second derivatives are not defined. Therefore, the second derivatives must be handled in a different fashion,

$$\int \nabla^2(V_j V_i) = \int \left(\frac{\partial^2}{\partial x^2}(V_j V_i) + \frac{\partial^2}{\partial y^2}(V_j V_i)\right)$$

$$\int \frac{\partial^2}{\partial x^2} V_j V_i = \int \frac{\partial}{\partial x}\left(\frac{\partial}{\partial x} V_j V_i\right) - \int \frac{\partial V_j}{\partial x} \frac{\partial V_i}{\partial x}$$

$$= \oint \frac{\partial}{\partial x} V_j V_i \Big|_e^w - \int \frac{\partial V_j}{\partial x} \frac{\partial V_i}{\partial x}$$

$$\int \frac{\partial^2}{\partial y^2} V_j V_i = \int \frac{\partial}{\partial y}\left(\frac{\partial V_j}{\partial y} V_i\right) - \int \frac{\partial V_j}{\partial y} \frac{\partial V_i}{\partial y}$$

$$= \oint \frac{\partial V_j}{\partial y} V_i \Big|_S^N - \int \frac{\partial}{\partial y} V_j \frac{\partial}{\partial y} V_i$$

where the $\oint$ implies a line integral along the east/west or north/south boundaries. The east/west line integrals are zero because of periodicity, but the north/south line integrals add additional terms to the equations and are satisfied by the boundary conditions. The Laplacian terms become

$$\int \nabla^2 V_j V_i = -\int \frac{\partial}{\partial x} V_j \frac{\partial}{\partial x} V_i - \int \frac{\partial}{\partial y} V_j \frac{\partial}{\partial y} V_i + \oint \frac{\partial}{\partial y} V_j V_i \Big|_S^N$$

This integration-by-parts procedure allows the use of a linear function while approximating second derivatives. The final form of the forecast equations is

$$-\int (\bar{\phi}_j \frac{\partial V}{\partial x} j \frac{\partial V}{\partial x} i + \bar{\phi}_j \frac{\partial V}{\partial y} j \frac{\partial V}{\partial y} i + \frac{\bar{\phi}_j V_j V_i}{\Phi(\Delta t)^2}) =$$

$$\int (\frac{\partial}{\partial x}((vQ)_j V_j - K_j \frac{\partial V}{\partial x} j)) V_i$$

$$-\int (\frac{\partial}{\partial y}((uQ)_j V_j + K_j \frac{\partial K}{\partial y} j)) V_i + \int \frac{1}{\Phi \Delta t}((\phi u)_j \frac{\partial V}{\partial x} j + (\phi v)_j \frac{\partial V}{\partial y} j) V_i$$

$$-\int \frac{\phi_j}{\Phi(\Delta t)^2}(t-\Delta t) V_j V_i + \int \frac{1}{\Delta t}(u_j(t-\Delta t)\frac{\partial V}{\partial x} j + v_j(t-\Delta t)\frac{\partial V}{\partial y} j) V_i$$

$$-\oint f_o u_j V_j V_i \Big|_S^N \qquad (4\text{-}27)$$

$$-\int (\frac{\partial \psi}{\partial t} j \frac{\partial V}{\partial x} j \frac{\partial V}{\partial x} i + \frac{\partial \psi}{\partial t} j \frac{\partial V}{\partial y} j \frac{\partial V}{\partial y} i) = -\int ((uQ)_j \frac{\partial V}{\partial x} j) V_i$$

$$-\int ((vQ)_j \frac{\partial V}{\partial y} j)\, V_i \qquad (4\text{-}28)$$

$$-\int (\frac{\partial \chi}{\partial t} j \frac{\partial V}{\partial x} j \frac{\partial V}{\partial x} i + \frac{\partial \chi}{\partial t} j \frac{\partial V}{\partial y} j \frac{\partial V}{\partial y} i + \bar{\phi}_j V_j V_i) =$$

$$\int (\frac{\partial}{\partial x}((vQ)_j V_j - K_j \frac{\partial V}{\partial x} j)) V_i$$

$$-\int (\frac{\partial}{\partial y}((uQ)_j V_j + K_j \frac{\partial V}{\partial y} j)) V_i \qquad (4\text{-}29)$$

Here the Helmholtz equation (4-27) has utilized

$$\nabla^2 \chi = \text{DIVERGENCE} = \frac{\partial u}{\partial x} + \frac{\partial v}{\partial y}$$

and

$$\frac{\partial \phi}{\partial y} = - u f_o$$

along the walls.

The line integral along the north and south boundary has been dropped from the vorticity ecuation (4-28), since the value of $\psi$ on the boundaries is a constant and therefore the value of $\frac{\partial \psi}{\partial t}$ is zero. The line integral along the north and south boundary has been dropped from the divergence equation (4-29), because the value of the normal derivative along the north/south walls is zero, as stipulated by the boundary conditions. The initial conditions will also satisfy the condition that the normal derivative of $\chi$ is zero along the north/south walls.

## B. FINITE DIFFERENCE MODEL

The comparison model to the GFEM model is an adaptation of the staggered, primitive-equation model as described in Section 7-4 of Haltiner and Williams (1980). The equations are in the flux form and employ Scheme C as shown in Section 7-3 of Haltiner and Williams (1980). The baroclinic model described there has been coded to perform in a barotropic mode.

Since the GFEM is written in differentiated form, vorticity and divergence have been diagnosed from the primitive variables in the finite difference model to allow appropriate comparisons.

## C. NUMERICAL METHODS

Although no attempt is made to optimize computational efficiency in this research model, the GFEM must utilize efficient numerical techniques to be considered a viable option for numerical weather prediction. Various solution procedures are available for the GFEM system of equations. Successive over-relaxation was employed during the early research stages. Several problems arose which indicated a need for a better solution procedure. The successive over-relaxation procedure resulted in a bias if the sweeping during each pass was in the same direction. Alternating the direction alleviated that particular problem, but the number of passes required to achieve a desired level of accuracy became prohibitive. A second approach employed a direct solver using a Gaussian elimination procedure. The matrices from the Galerkin procedure are decomposed into upper and lower block tri-diagonal matrices. A preprocessing, representing the forward substitution stage, can be done once. The back substitution must be done each time a solution is desired. The coefficients necessary for this back substitution are stored in an efficient manner. The particular

algorithm is called a "skyline" solver and is described in detail in Bathe and Wilson (1976). Skyline refers to the compact method of storing only those coefficients required. This method has the desired level of accuracy and a high degree of computational efficiency. Staniforth and Mitchell (1977) employed another direct solver method called, the conjugate- gradient method. This method is very computationally efficient, even when the non-constant coefficient Helmholtz equation is involved. The theoretical operation count indicates that for very large domains with many degrees of freedom, the conjugate-gradient method will be much better than the other direct solver mentioned above. The Gauss elimination procedure was utilized instead of the conjugate-gradient method for reasons of expediency.

Numerical integration of the three forecast equations involves solving first a Helmholtz equation for $\phi$, second a Poisson problem for $\psi$ and finally a Poisson problem for $\chi$. The boundary conditions and the equations are well posed for the first two equations. However, the normal derivative of $\chi$ is equal to zero for the last Poisson equation and requires special attention. The solution plus a constant is also a solution. Since only derivatives of $\chi$ are required, the shape of the field is much more important than the actual value of $\chi$. To avoid computer round off errors, the average value of the terms on the right hand side of (4-29) is removed at each time step. This sets the constant to

zero and does not allow the solution to grow by a constant each iteration.

The current technology of large mainframe computers incorporates vector processing. Utilization of this ability can be achieved when the system of equations can be vectorized. The GFEM is derived in vector formulation and is easily vectorized.

## D. INITIAL CONDITIONS

### 1. Simple Atmospheric Waves

The initial conditions must allow a relative amount of control for the desired input parameters as well as satisfy the boundary conditions. The forecast model history-carrying variables are $\phi$, u and v. The analytic expression for the streamfunction, $\psi$, is

$$\psi = A \sin^2 \frac{\pi y}{W} \sin \frac{2\pi n x}{L} - \bar{U}(y-y_{mid}) + \frac{\Phi}{f_o} \qquad (4\text{-}30)$$

where A = amplitude of the perturbation,

W = width of the channel,

L = length of the channel,

n = wave number,

$\bar{U}$ = mean flow speed, and

$y_{mid}$ = middle point of the channel

The first term in the expression is the perturbation. The second term represents the north/south slope necessary to support a mean flow of $\bar{U}$. The third term is the mean depth term. The geopotential height, $\phi$, is related geostrophically to the streamfunction, $\psi$, by

$$\phi = f_o \psi \tag{4-31}$$

By use of a trigonometric identity, the streamfunction is written as

$$\psi = \frac{A}{2}(1 - \cos\frac{2\pi y}{w})\sin\frac{2\pi n x}{L} - \bar{U}(y-y_{mid}) + \frac{\Phi}{f_o} \tag{4-32}$$

The vorticity is given by

$$\zeta = 2\alpha_1{}^2 A \sin\alpha_2 x \cos 2\alpha_1 y - \alpha_2{}^2 \frac{A}{2}\sin\alpha_2 x + \alpha_2{}^2 \frac{A}{2}\sin\alpha_2 x \cos 2\alpha_1 y \tag{4-33}$$

where

$$\alpha_1 = \frac{\pi}{W}$$

$$\alpha_2 = \frac{2\pi n}{L}$$

The divergence is determined through a linearized form of the quasi-geostrophic divergence equation from Chapter 3-2 of Haltiner and Williams (1980), in the form

$$\nabla^2 D - \frac{f_o^2}{\Phi} D = \frac{f_o}{\Phi} \bar{U}\frac{\partial}{\partial x}\nabla^2\psi \tag{4-34}$$

The right-hand side of this equation becomes

$$\cos \alpha_2 x \left[\left(\frac{f_o}{\Phi}\bar{U} 2\alpha_1{}^2 A\alpha_2 + \frac{f_o}{\Phi}\bar{U}\alpha_2{}^3\frac{A}{2}\right)\cos 2\alpha_1 y - \frac{f_o}{\Phi}\bar{U}\alpha_2{}^3\frac{A}{2}\right] \qquad (4\text{-}35)$$

Assuming a solution form for divergence on the left-hand side

$$D = \cos \alpha_2 x(C_1 \cos 2\alpha_1 y + C_2)$$

the constants $C_1$ and $C_2$ become

$$C_1 = -\left(\frac{f_o}{\Phi}\bar{U} 2\alpha_1{}^2 A\alpha_2 + \frac{f_o}{\Phi}\bar{U}\alpha_2{}^3\frac{A}{2}\right)/\left(4\alpha_1{}^2 + \alpha_2{}^2 + \frac{f_o}{\Phi}{}^2\right)$$

and

$$C_2 = \frac{f_o}{\Phi}U\alpha_2{}^3\,\frac{A}{2}/\left(\alpha_2{}^2 + \frac{f_o}{\Phi}{}^2\right)$$

Using $\nabla^2\chi = D$ and assuming a solution form for $\chi$ as

$$\chi = \cos\alpha_2 x(C_3 \cos 2\alpha_1 y + C_4) \qquad (4\text{-}36)$$

then $C_3$ and $C_4$ become

$$C_3 = -C_1/(4\alpha_1{}^2 + \alpha_2{}^2)$$

and

$$C_4 = -C_2/\alpha_2{}^2$$

Observe that $\psi$ equals a constant and $\frac{\partial \chi}{\partial y}$ equals zero along the north/south walls. With the expressions for stream-function, (4-32), and velocity potential, (4-36), appropriate formulae for u and v can be derived.

$$u = \bar{U} - \sin \alpha_2 x(A\alpha_1 \sin 2\alpha_1 y + \alpha_2(C_3 \cos 2\alpha_1 y + C_4)) \quad (4\text{-}37)$$

and

$$v = \cos \alpha_2 x(\alpha_2 \frac{A}{2}(1-\cos 2\alpha_1 y) - 2C_3 \alpha_1 \sin 2\alpha_1 y) \quad (4\text{-}38)$$

and $\phi$ is given by equations (4-31) and (4-32).

2. Source Term

The addition of a source term into the continuity equation will test the resolvability of the GFEM model for a source. The source is constructed to represent a small-scale meteorological phenomenon to provide a measure of the response of the GFEM model to forcing near the smallest grid scale. The source initial conditions must be able to describe a small-scale feature embedded in a large synoptic situation. The initial conditions are derived by choosing a desired solution and then back substituting to derive the form of the source required. This is a unique approach when adding a source term. First, a source, S, is added to the continuity equation in the form of

$$\frac{\partial \phi}{\partial t} + u\frac{\partial \phi}{\partial x} + v\frac{\partial \phi}{\partial y} + \phi(\frac{\partial u}{\partial x} + \frac{\partial v}{\partial y}) = S\phi \quad (4\text{-}39)$$

Following the scale analysis of Chapter 3-2 in Haltiner and Williams (1980),a new quasi-geostrophic potential vorticity equation is formed with the source term included,

$$(\frac{\partial}{\partial t} + u_\psi \frac{\partial}{\partial x} + v_\psi \frac{\partial}{\partial y})(\zeta - \frac{f\phi}{\Phi}) + f S = 0$$

Solving for S leaves

$$S = (\frac{\partial}{\partial t} - \frac{\partial \psi}{\partial y}\frac{\partial}{\partial x} + \frac{\partial \psi}{\partial x}\frac{\partial}{\partial y})(\frac{f\psi}{\Phi} - \frac{1}{f}(\frac{\partial^2 \psi}{\partial x^2} + \frac{\partial^2 \psi}{\partial y^2})) \qquad (4\text{-}40)$$

The technique for testing the source term is to pick a streamfunction and then solve for the source term which will satisfy that streamfunction. The particular streamfunction evaluated will be a steady state solution. The source in this case is

$$S = \frac{1}{f_o}(\frac{\partial \psi}{\partial y}\frac{\partial}{\partial x}(\frac{\partial^2 \psi}{\partial x^2} + \frac{\partial^2 \psi}{\partial y^2}) - \frac{\partial \psi}{\partial x}\frac{\partial}{\partial y}(\frac{\partial^2 \psi}{\partial x^2} + \frac{\partial^2 \psi}{\partial y^2})) \qquad (4\text{-}41)$$

The particular form of the streamfunction is

$$\psi = -\bar{U}(y - y_{mid}) - A\sin^2\frac{\pi y}{W} e^{-\frac{1}{R}\sin^2(\frac{\pi x}{L})} \qquad (4\text{-}42)$$

where R is a constant. The use of the exponential allows a variation in the scale whereby a small scale feature can be embedded in a larger flow pattern. Substitution of this particular $\psi$ into the expression for the source yields

$$S = \frac{1}{f_o}(\bar{U} + \frac{A\pi}{W}\sin\frac{2\pi y}{W}e^{-\frac{1}{R}\sin^2\frac{\pi x}{L}})(\frac{1}{R}\frac{\pi}{L}\sin\frac{2\pi x}{L}e^{-\frac{1}{R}\sin^2\frac{\pi x}{L}}$$

$$(\frac{A}{R}(\frac{\pi}{L})^2\sin^2\frac{\pi y}{W}(2\cos\frac{2\pi x}{L} - \frac{1}{R}\sin^2\frac{2\pi x}{L}) - 2A(\frac{\pi}{W})^2\cos\frac{2\pi y}{W})$$

$$+ e^{-\frac{1}{R}\sin^2\frac{\pi x}{L}}(\frac{A}{R}(\frac{\pi}{L})^2\sin^2\frac{\pi y}{W}(\frac{4\pi}{L}\sin\frac{2\pi x}{L} + \frac{2\pi}{RL}\sin\frac{4\pi x}{L})))$$

$$- \frac{1}{f_o}(\frac{A}{R}\frac{\pi}{L}\sin^2(\frac{\pi y}{W})e^{-\frac{1}{R}\sin^2\frac{\pi x}{L}}\sin\frac{2\pi x}{L})$$

$$(e^{-\frac{1}{R}\sin^2\frac{\pi x}{L}}\sin\frac{2\pi y}{W}(\frac{A}{R}(\frac{\pi}{L})^2(\frac{\pi}{W})(2\cos\frac{2\pi x}{L} - \frac{1}{R}\sin^2\frac{2\pi x}{L})$$

$$+ 4A(\frac{\pi}{W})^3)) \qquad (4\text{-}43)$$

## E. NONLINEAR EFFECTS

Cullen (1974a) discussed the requirement to simulate the cascade of energy to unresolved wavelengths. To avoid accumulation of energy in the shortest resolvable wavelengths, he developed a two-step method for computing the nonlinear terms. Implementation of the two-step method can be accomplished efficiently. In the formal development of the model equations, there are several nonlinear terms. The two-step method involves projecting both variables in a nonlinear term into Galerkin space and then performing the

multiplication. This procedure insures the best approximation to that nonlinear term in a weighted-mean sense. Additionally, the computational effort for the two-step method is much less than the one-step method which involves computation of all the possible interaction coefficients.

## F. STABILITY CRITERION

The stability criterion for the forecast equations is

$$\Delta t \leq \frac{1}{\frac{|\bar{U}|}{\Delta x} + f}$$

This is more restrictive than a normal Courant-Fredrich-Lewy (CFL) condition. It is made up of the normal CFL criterion based on advection plus another effect due to rotation (inertial motion). It provides an upper boundary to the maximum allowable time step when using a semi-implicit scheme. In this research, time steps in excess of an hour are easily used. Care must be taken not to exceed the stability criterion when larger mean flows are experienced or when moving to higher latitudes (larger f).

A more detailed discussion of the derivation of the stability criterion can be found in Appendix A.

# V. EXPERIMENTS AND RESULTS

Experiments will be performed involving the features in Chapter II to test the hypothesis. Four separate experiments will be performed. The first experiment will establish the overall performance characteristics of three specified models. The next three experiments will address each specific feature supporting the hypothesis.

Standards of comparison must be established for each experiment. The basic comparison will be achieved through harmonic analysis of the initial and forecast fields. The harmonic analysis is a double Fourier decomposition. The harmonic analysis requires that the data be on a uniform grid. Because of the triangular and variable grids, an interpolation is necessary. A fifth degree polynomial surface fitting routine from the International Mathematics and Statistics Library (IMSL) was employed to interpolate data on the non-uniform grids to a uniform spacing. First, a harmonic analysis is performed along columns of constant x to obtain the y structure of the initial conditions. Then a harmonic analysis of the amplitudes of each y wave number along rows gives a true double harmonic analysis. This double transform approach is necessary due to the initial conditions. The use of $\sin^2 \frac{\pi y}{W}$ in the y direction is the same as using $(1.0 - \cos \frac{2\pi y}{W})$. The boundary conditions are

satisfied by a sine wave in the y direction. Therefore, an infinite sine series is needed to represent the cosine function.

The theoretical movement of each wave is obtained from an analysis of the shallow-water equations. The analysis in Section 2-6 of Haltiner and Williams (1980) predicts the wave speed as

$$C = \bar{U} + \frac{(f/H)\frac{\partial H}{\partial y}}{\mu^2 + f^2/gH} \qquad (5\text{-}1)$$

where

$C$ equals wave speed,

$H$ equals height, and

$\mu$ x direction wave number.

By generalizing the streamfunction to a two-dimensional wave form

$$\psi = A \sin \frac{n\pi y}{W} \cos \mu(x-ct) \qquad (5\text{-}2)$$

and after further manipulation, the wave speed becomes

$$C = \bar{U}(1/(1 + f_o^2/\Phi(\mu_x^2 + \mu_y^2)))$$

where

$\Phi$ equals average geopotential height,

$\mu_x$ equals x direction wave number, and

$\mu_y$ equals y direction wave number.

## A. EXPERIMENT 1

Establishing wave propagation characteristics on a uniform grid will illuminate the properties of each model. Three models will be compared:

1. A triangular subdivision GFEM model;
2. A rectangular subdivision GFEM model; and
3. An equivalent finite difference model.

The GFEM models will use the differentiated form of the shallow-water equations with a semi-implicit scheme. The finite difference model uses the undifferentiated form on a staggered grid with a centered (leapfrog) time scheme. The triangular subdivision uses equilateral triangles. The relationship between base and height for an equilateral triangle is

$$\text{BASE} = 2 \times \text{HEIGHT}/\sqrt{3}$$

The x distance therefore has the same relationship to the y distance

$$\Delta x = 2\,\Delta y/\sqrt{3}$$

To perform comparisons of similar models, the same x, y relationship is retained for the rectangular and finite difference models.

The basic difference between the rectangular and triangular models will be in the approximating polynomials. The rectangular polynomials are bilinear while the

triangular polynomials are linear. The higher order polynomials should provide an increase in accuracy. During the integration process, many integrals require evaluation. Numerical quadrature could be utilized, however, a more efficient method is available through the use of natural coordinates. Quadrature with no error can be accomplished by formula with this method. A detailed description of the natural coordinate method is delineated in Appendix B for both triangles and rectangles.

Diagrams for the grids for the triangular, rectangular and finite difference models are shown in Figures 2, 3 and 4 respectively. The domain is 4896.0 km in the y direction and 5653.0 km in the x direction. Each model has 12 increments in the x and y directions. This gives 156 degrees of freedom. All tests will be for a 48 hour time integration, a mean flow of 10 m/s and a mean depth of 1000 meters. A perturbation of 1 m/s will be added to the geopotential field, which includes the mean height plus the north/south slope required for the 10 m/s mean flow. This small perturbation will focus on the linear aspects of the model's capabilities. Experiments described below will evaluate larger perturbations, and hence the nonlinear interactions. Models are evaluated for wave numbers 1, 2, 3 and 4.

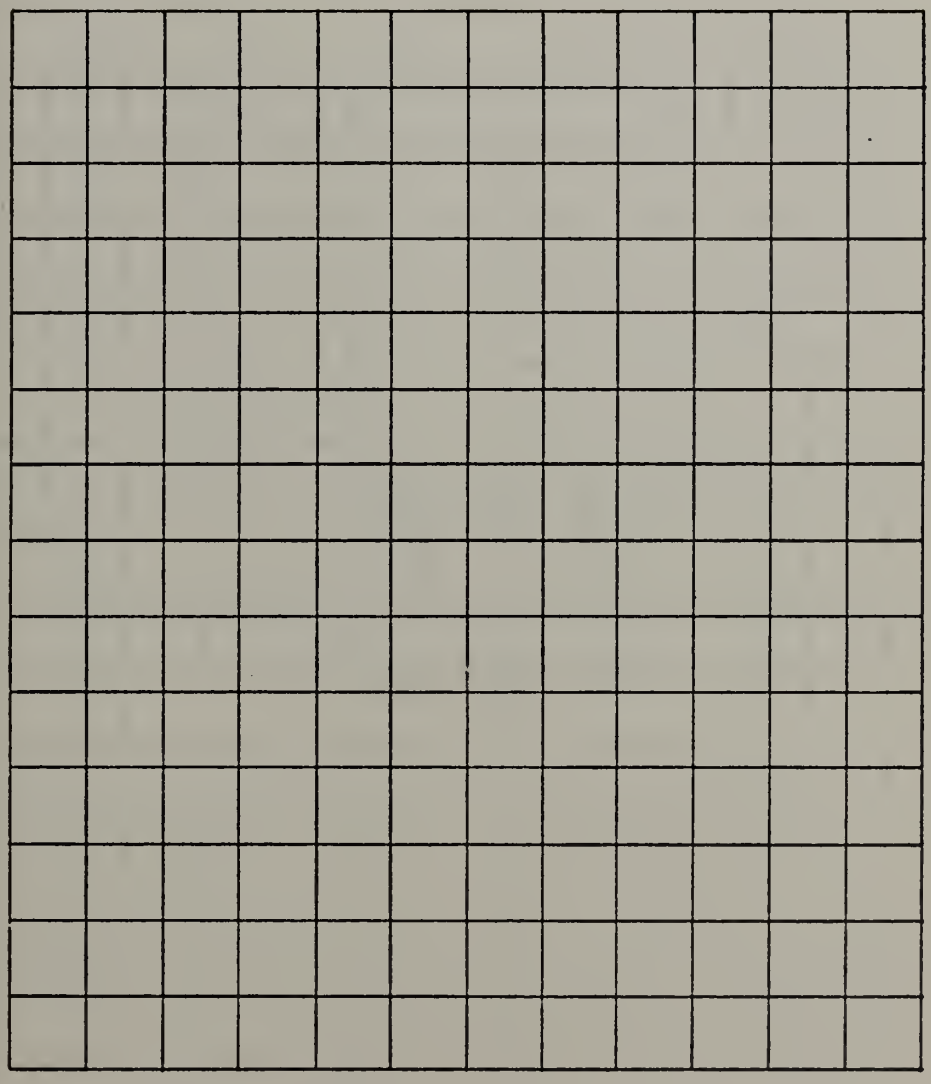

Fig. 3. Rectangular uniform subdivision for a channel in Cartesian coordinates.

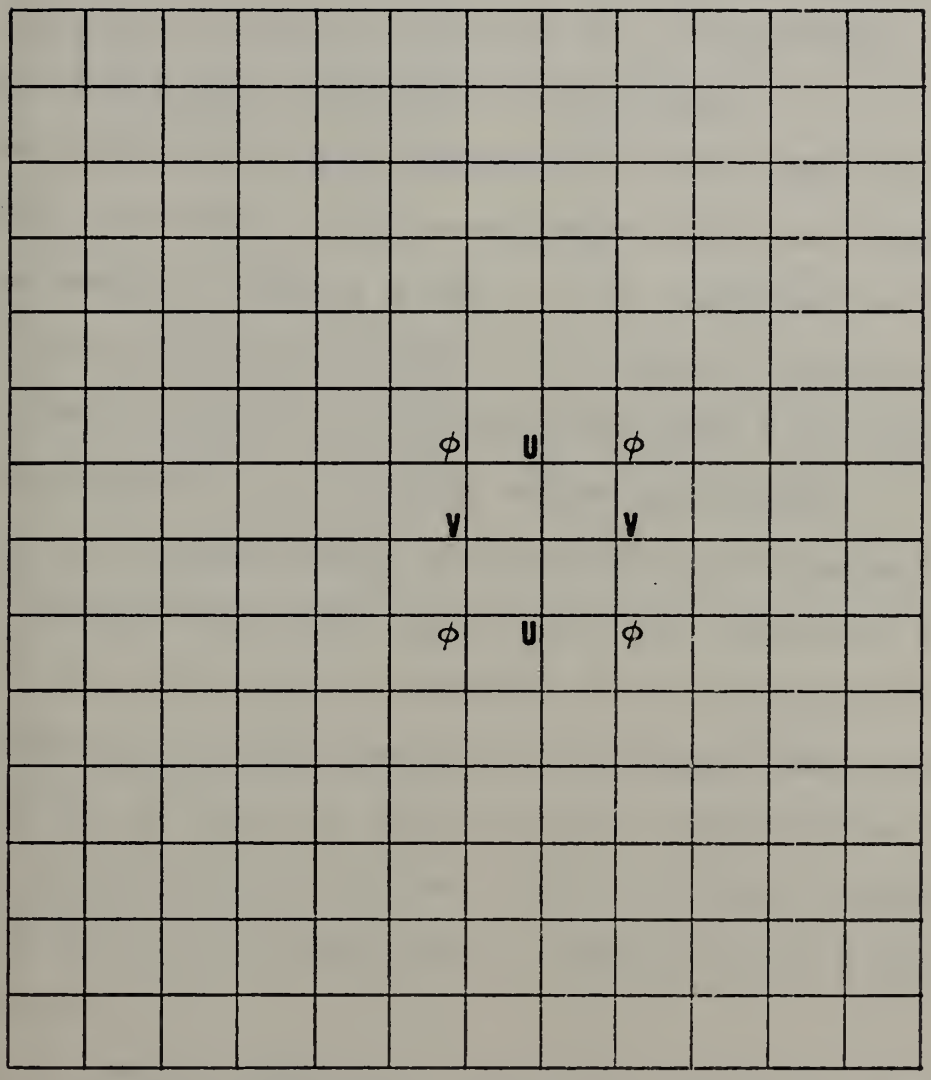


Fig. 4. Finite difference uniform grid for a channel in Cartesian coordinates.

B. RESULTS 1

The propagation characteristics of the GFEM models and the finite difference model on a uniform grid will be evaluated. Graphical displays will highlight synoptic characteristics. Harmonic analysis will show phase propagation and wave amplitude distributions.

The initial and 48-h forecasts for the conditions stated in experiment 1 with wave number one on a triangular grid are shown in Figures 5 and 6. The southeast/northwest orientation in the forecast fields is due to the sine waveform in the y direction. This waveform with model boundary conditions requires an infinite number of y modes. Fortunately, the amplitudes of the higher wave numbers are small. Consequently, there are only a few important modes. The multiple modes cause a skewness in the solutions for all three models since the y-modes have different phase speeds. Additionally, an analytic expression for the solution requires an infinite sum of the modes. For this reason, no true solution has been computed to compare with the GFEM and FDM models.

The divergence equation is the most sensitive equation of the three forecast equations. A mean depth of 1000 meters was chosen because the divergence is large. Therefore, a critical evaluation of the sensitivity of the GFEM model to this important meteorological parameter can be

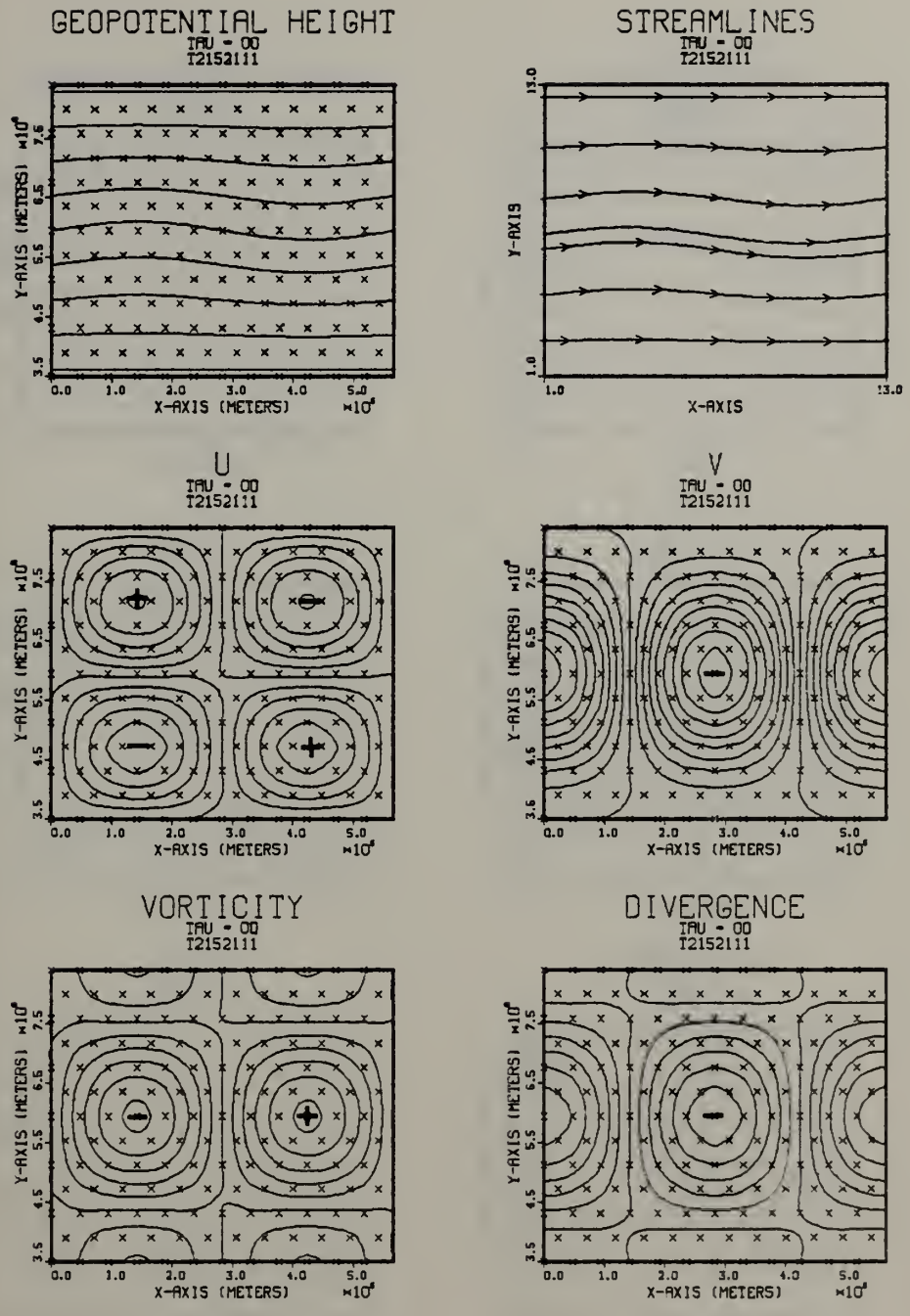


Fig. 5. Initial conditions for the GFEM model with a triangular subdivision and wave number one. Contour intervals are 600 $m^2/s^2$ for geopotential height, .2 m/s for u and v, $.6 \times 10^{-6}$ $s^{-1}$ for vorticity and $.2 \times 10^{-7} s^{-1}$ for divergence. Nodal points are denoted by an x.

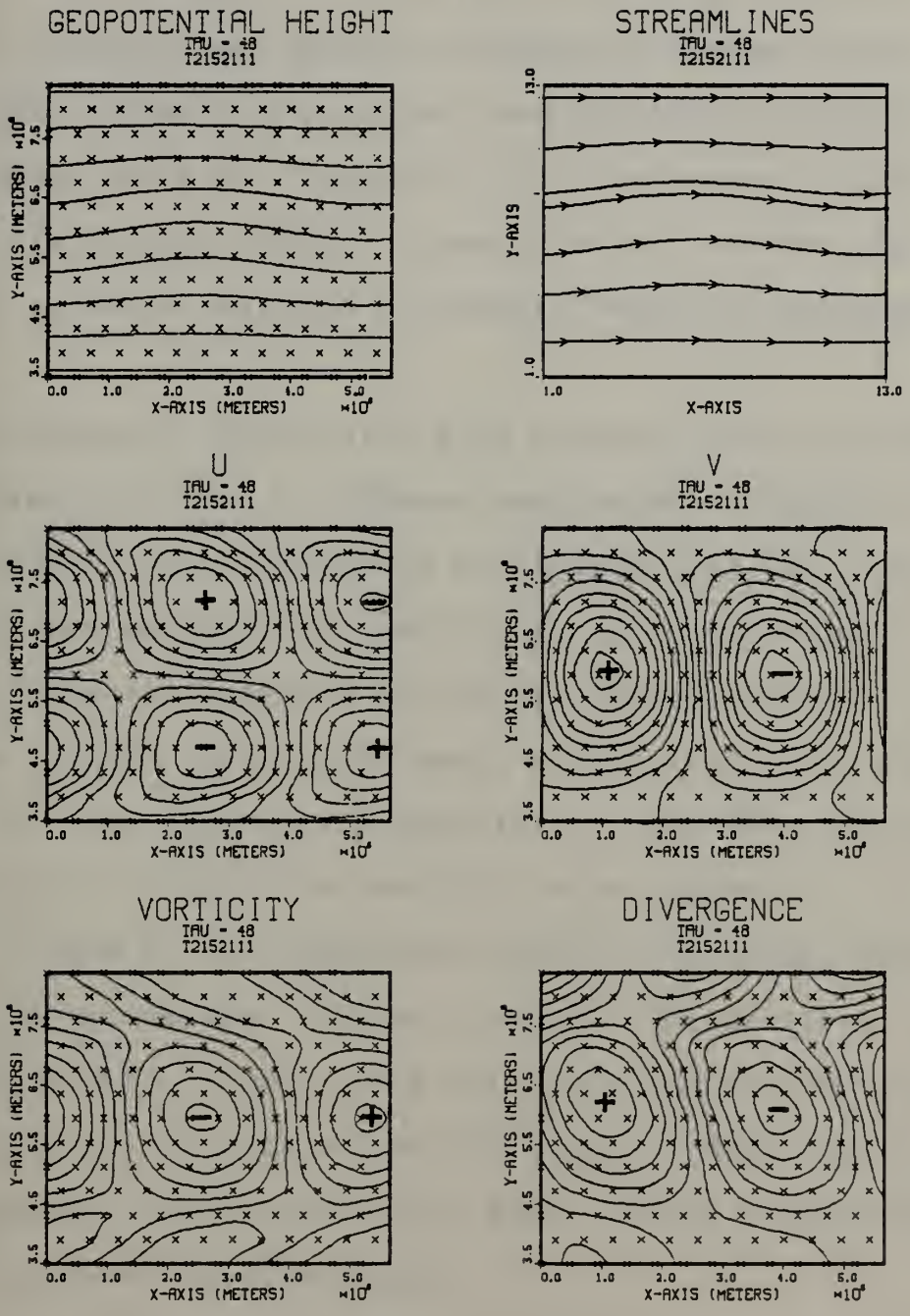


Fig. 6. As in Fig. 5 but a 48-h forecast.

performed. A divergence field which has propagated uniformly with the vorticity field is shown in Figure 6. Harmonic analysis (not shown) indicates divergence amplitudes which initially adjust and then oscillate slightly about a mean value of $.1270 \times 10^{-7}$ $s^{-1}$. The phases of all forecast fields are uniform. Synoptically, the forecast fields $\phi$, u, and v indicate a smoothly resolved atmospheric wave.

A rectangular subdivision 48-h forecast for wave number one is shown in Figure 7. Comparisons between Figures 6 and 7 show little if any difference which indicates that the triangular and rectangular subdivisions give comparable results. Harmonic analysis of the divergence fields indicates a small oscillation about a mean similar to that observed for the triangular subdivision. The 48-h forecast from the finite difference model for wave number one is shown in Figure 8. The equivalent finite difference model also has 12 increments in each direction. Comparisons between Figures 6, 7 and 8 show that the finite difference model vorticity field lags the GFEM models. Additionally, the divergence field has lost its areal extent and developed a strong gradient of divergence.

In each of the wave number one tests there were 12 grid points representing the wave. Good propagation should be expected from all three of the models for a 12-increment

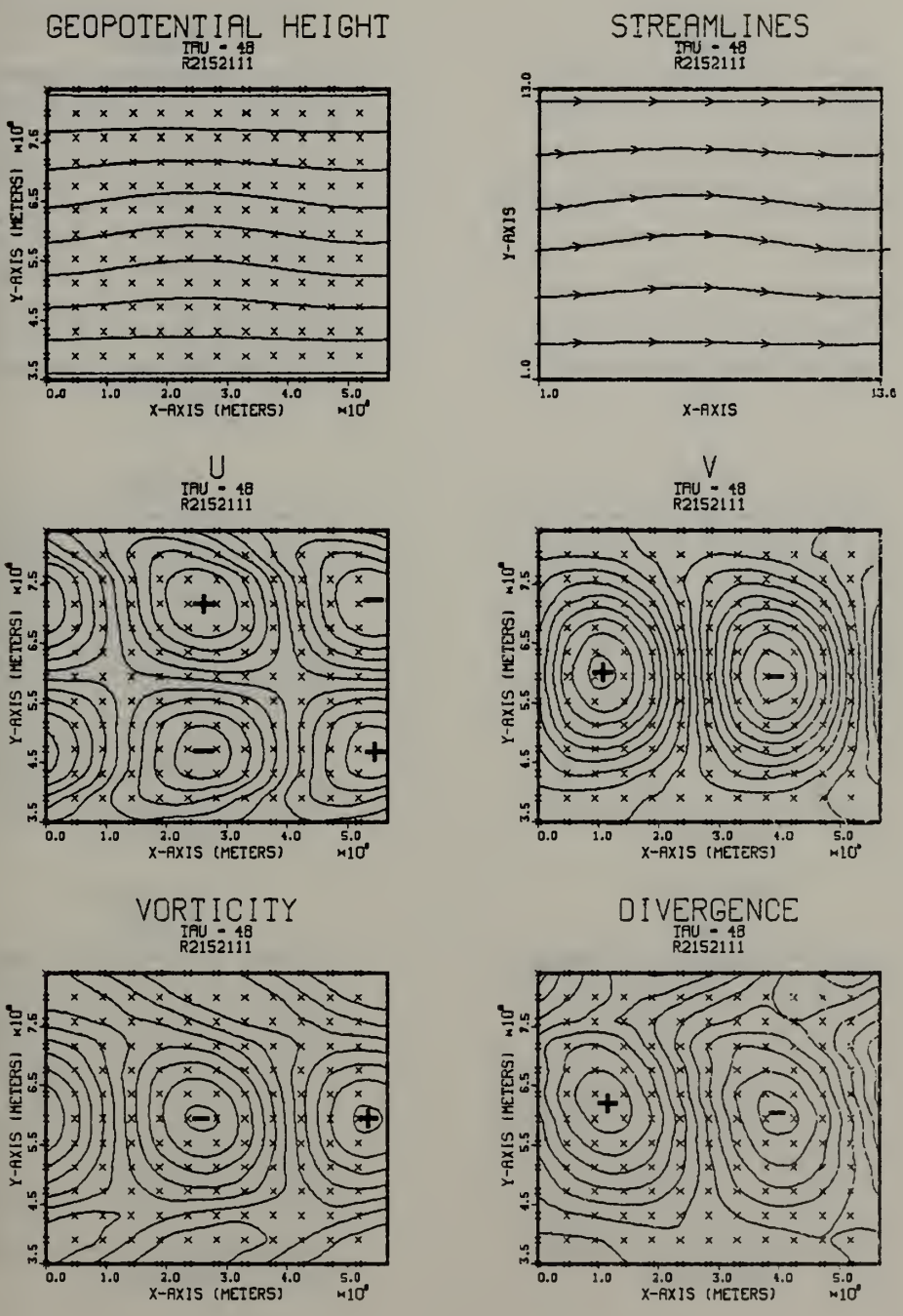


Fig. 7. As in Fig. 6 but a rectangular subdivision.

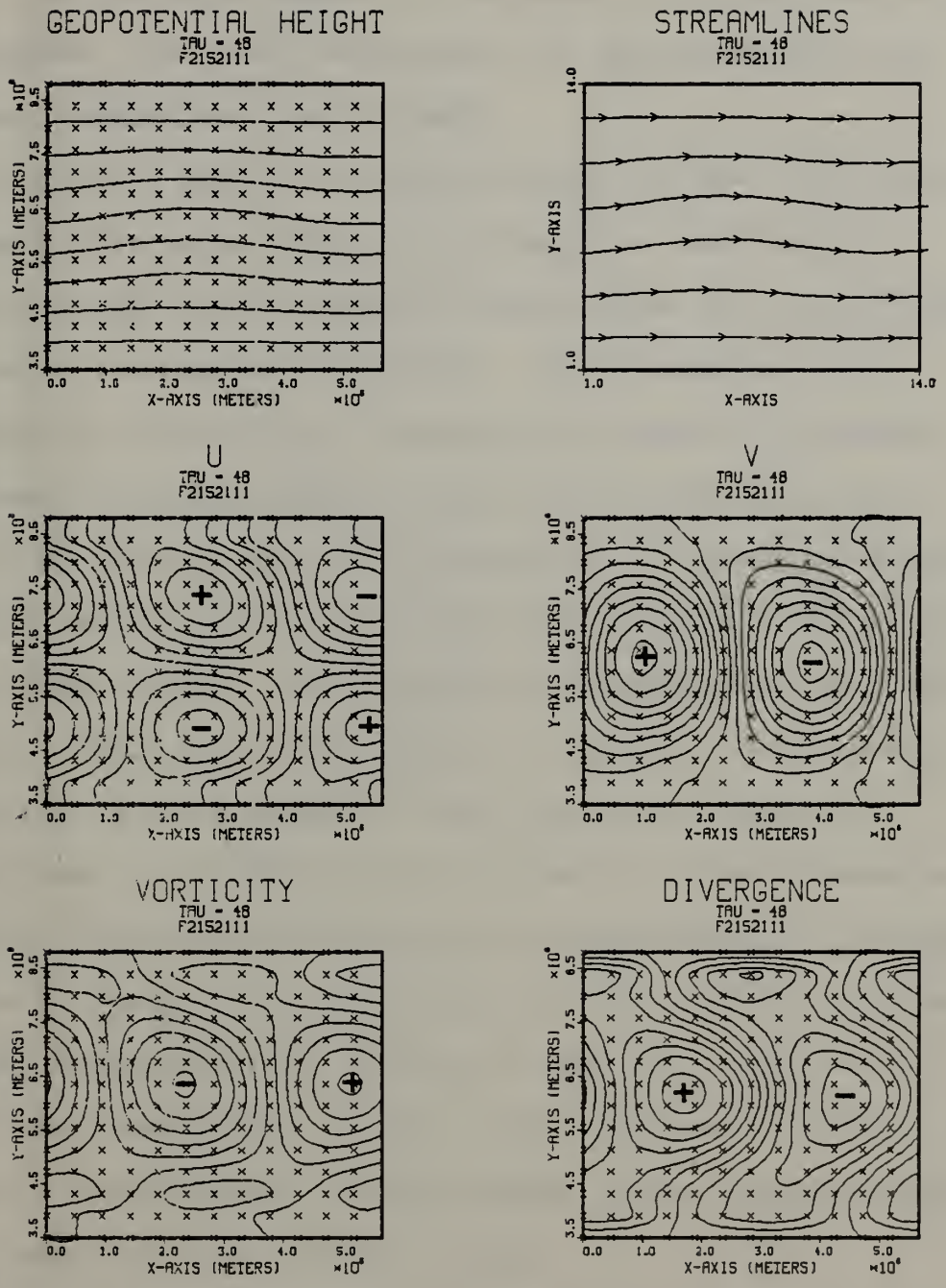


Fig. 8. As in Fig. 6 but a FDM model.

wave. As the wave number is increased with the same degrees of freedom, the wave resolution will be decreased, and clearer comparisons can be made.

Figures 9 and 10 are the initial and 48-h GFEM model forecasts for wave number 2, triangular subdivision. Forecasts for the rectangular subdivision and the FDM model are shown in Figures 11 and 12. The triangular and rectangular subdivision forecasts are similar. However, the FDM model forecast displays additional divergence and vorticity centers near the boundaries. Figures 13 through 16 are a series similar to Figures 9 through 12 except for wave number three. These waves are represented by 4 grid points. There are indications in Figure 14 that energy is appearing in wave numbers other than wave number 3. Comparison of Figures 14 and 15 show that the triangular forecast contains more noise than the rectangular forecast. Figure 16 shows a divergence field from the FDM model which is very different from Figures 14 and 15. There is a north/south asymmetry in the u and divergence fields. The u cells in the northern regions appear to be expanding while the southern cells are decreasing.

Table 1 is a composite of the harmonic analysis for the triangular, rectangular and finite difference wave number 3 case (v component amplitudes). The initial and

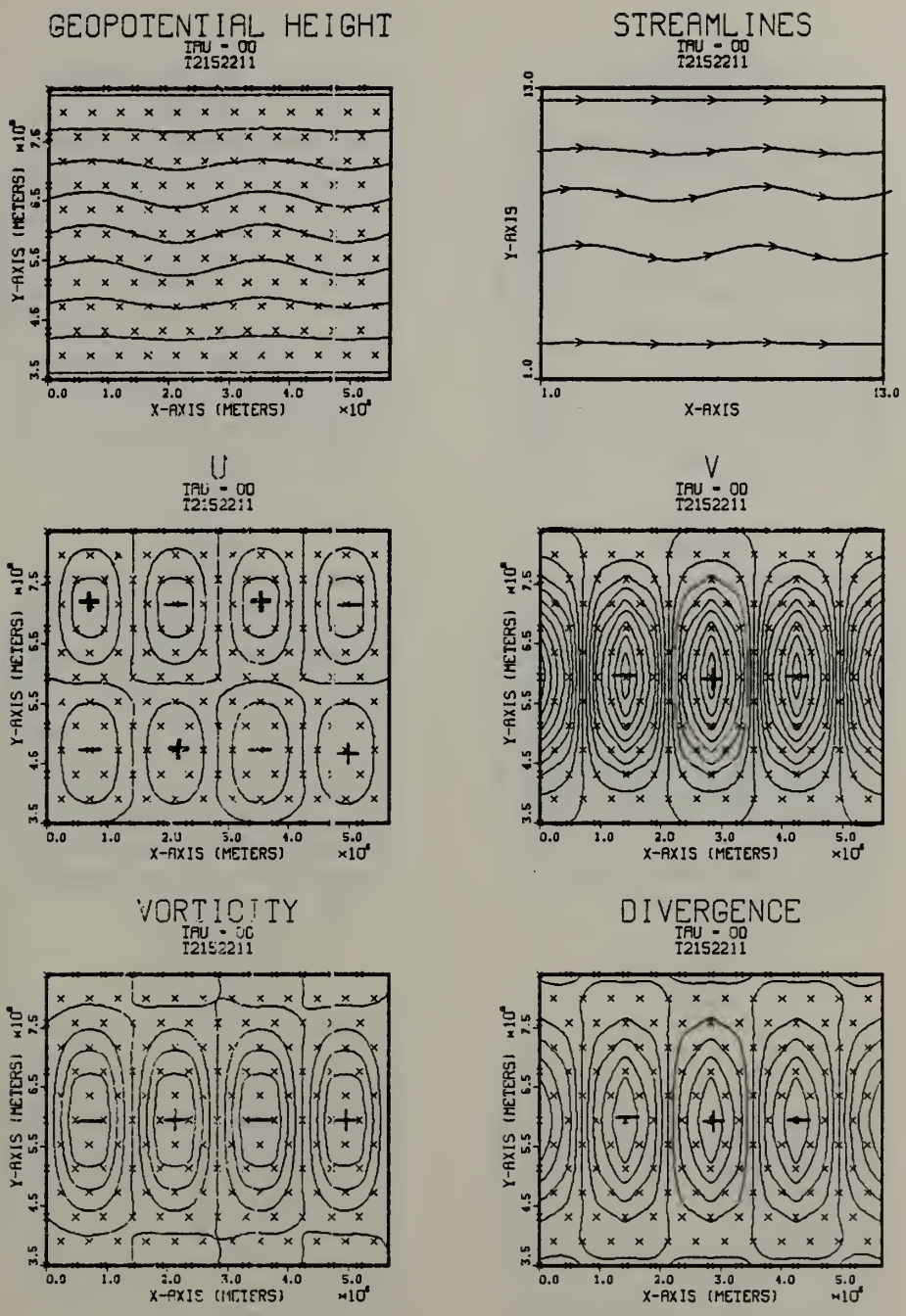


Fig. 9. As in Fig. 5 except for wave number two. Contour intervals are 600 $m^2/s^2$ for geopotential height, .4 m/s for u and v, $.2 \times 10^{-5}$ $s^{-1}$ for vorticity and $.6 \times 10^{-7}$ $s^{-1}$ for divergence.

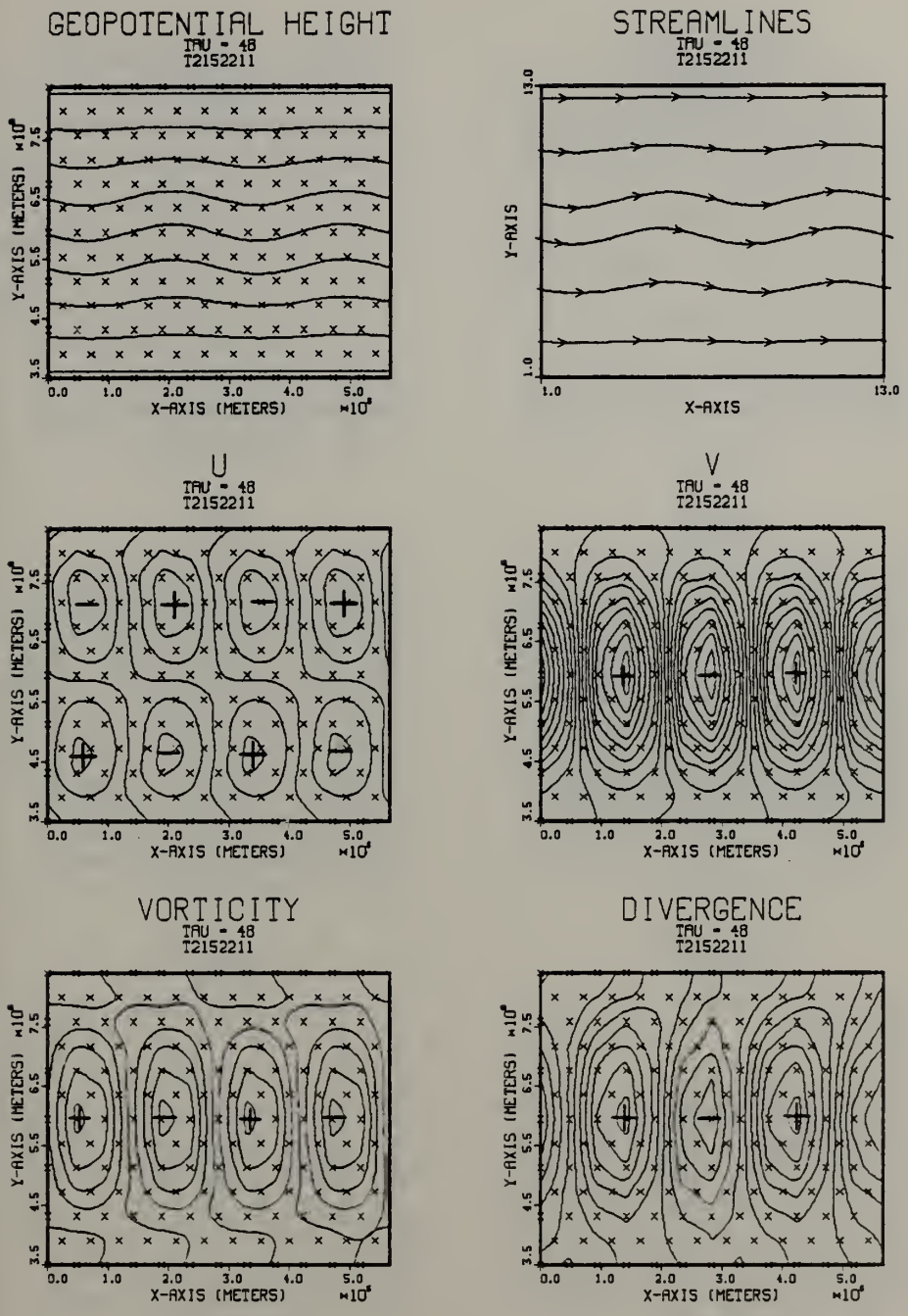


Fig. 10. As in Fig. 9 but a 48-h forecast.

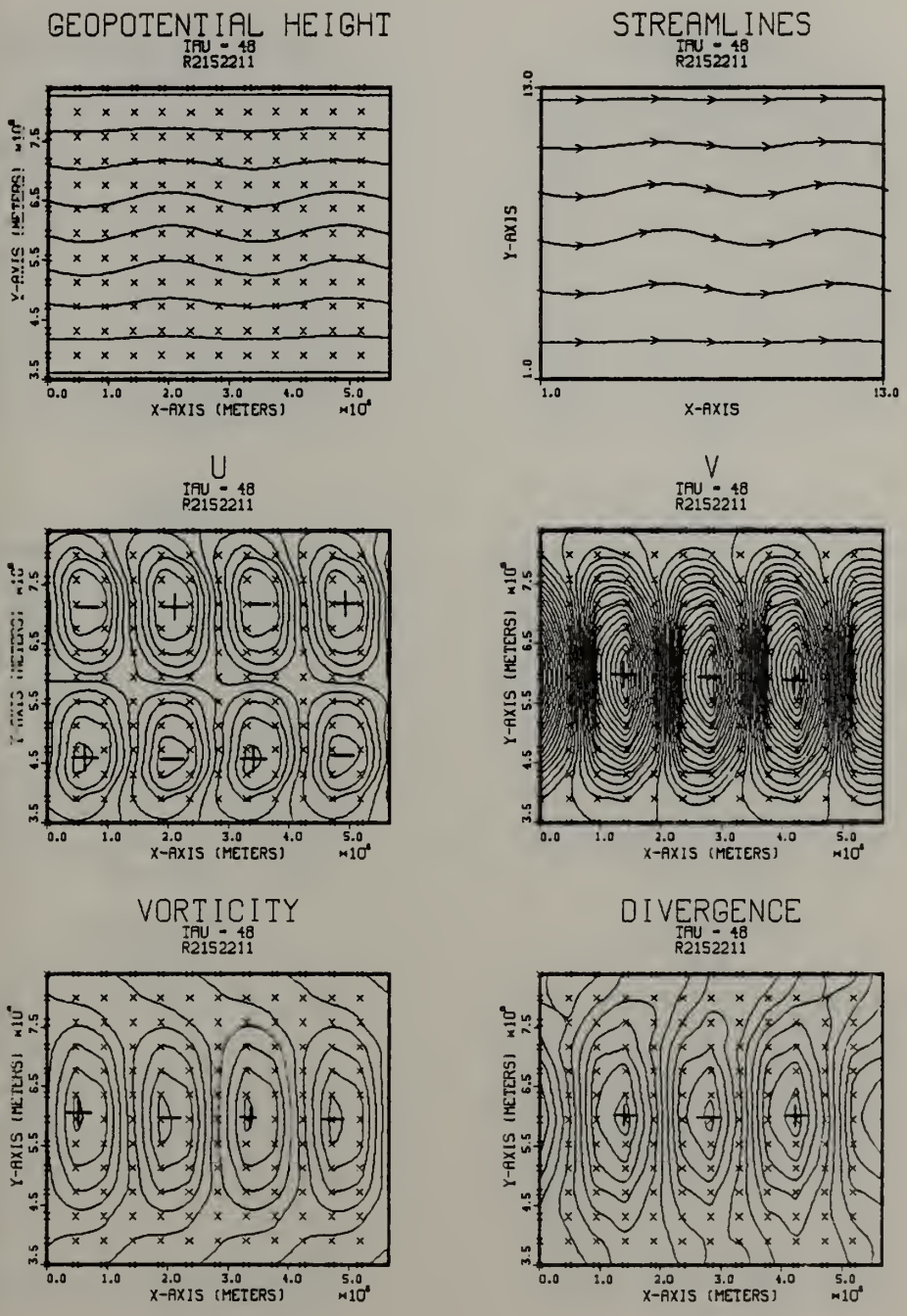


Fig. 11. As in Fig. 10 but a rectangular subdivision.

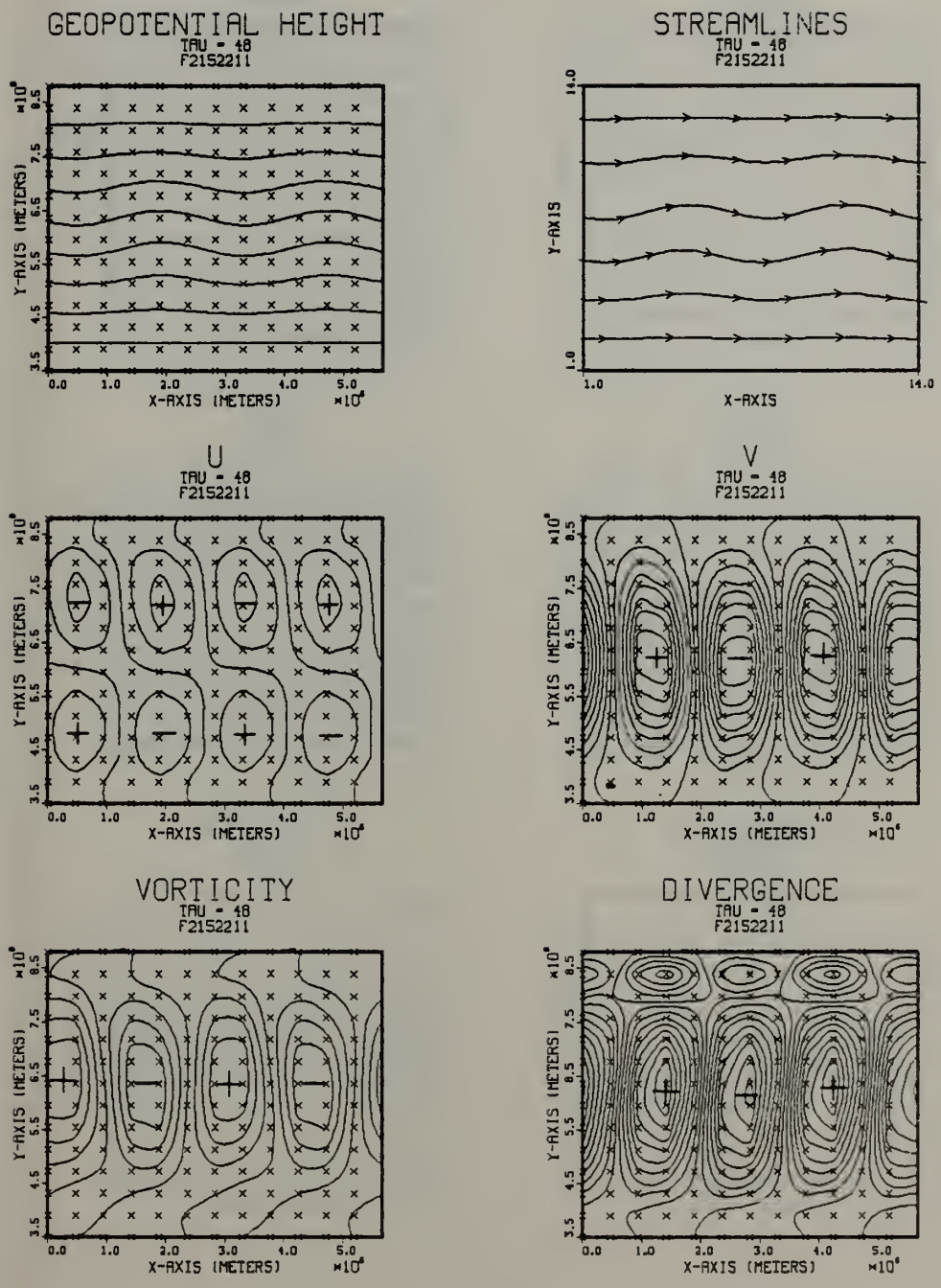


Fig. 12. As in Fig. 10 but a FDM model.

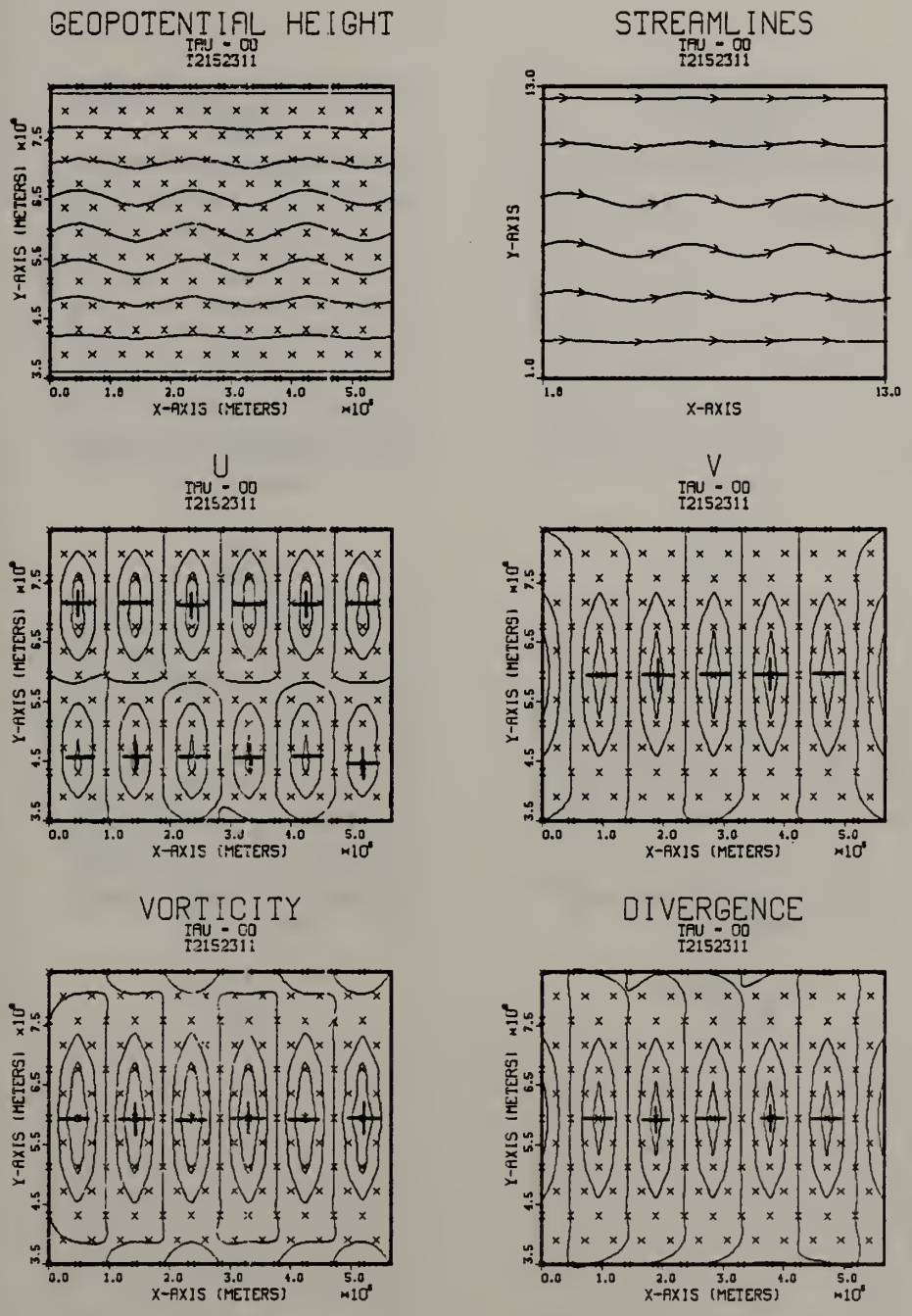


Fig. 13. As in Fig. 5 except for wave number three. Contour intervals are 600 $m^2/s^2$ for geopotential height, .4 m/s for u, 2.0 m/s for v, $.6 \times 10^{-5}$ $s^{-1}$ for vorticity and $.2 \times 10^{-6}$ $s^{-1}$ for divergence.

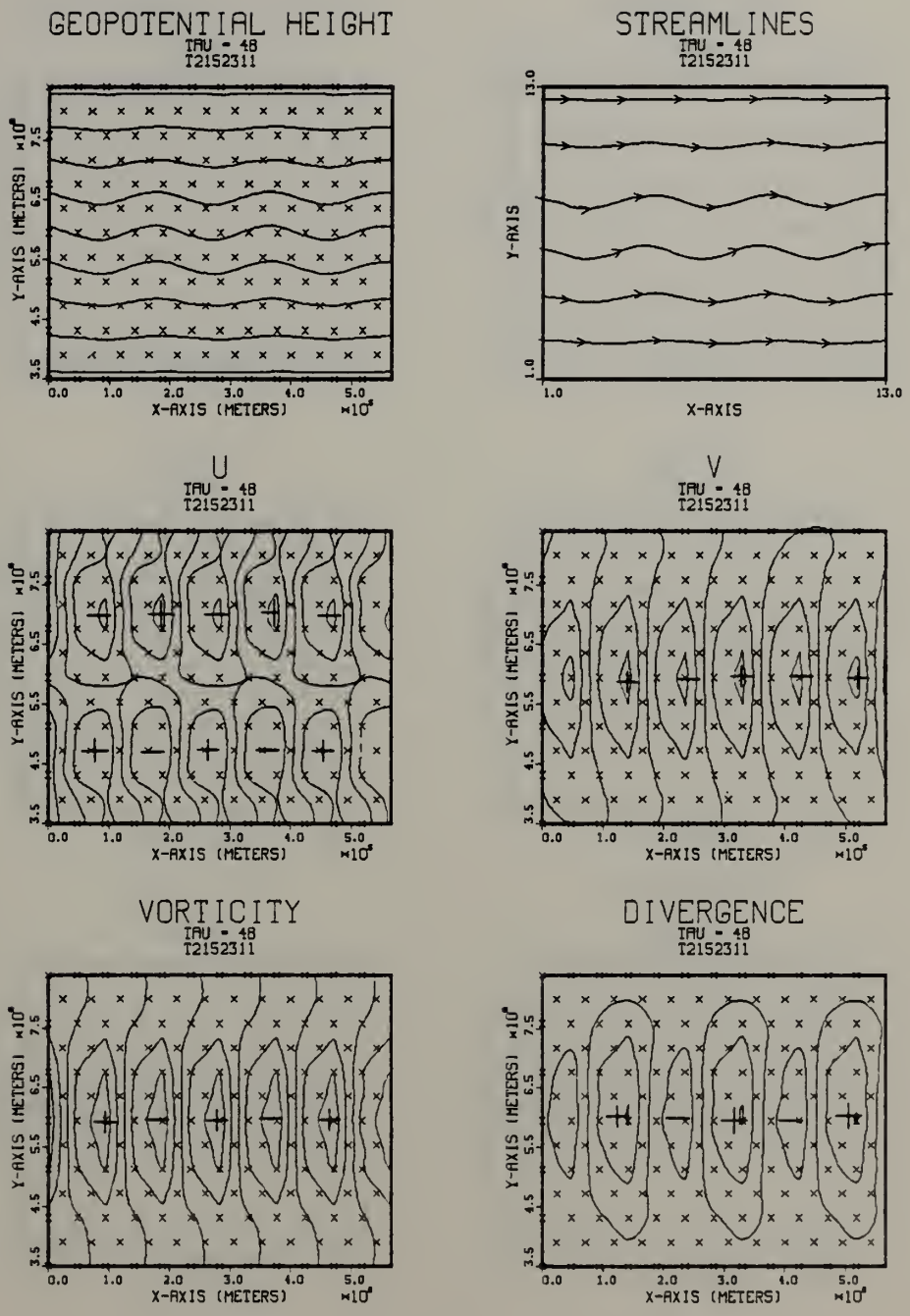


Fig. 14. As in Fig. 13 but a 48-h forecast.

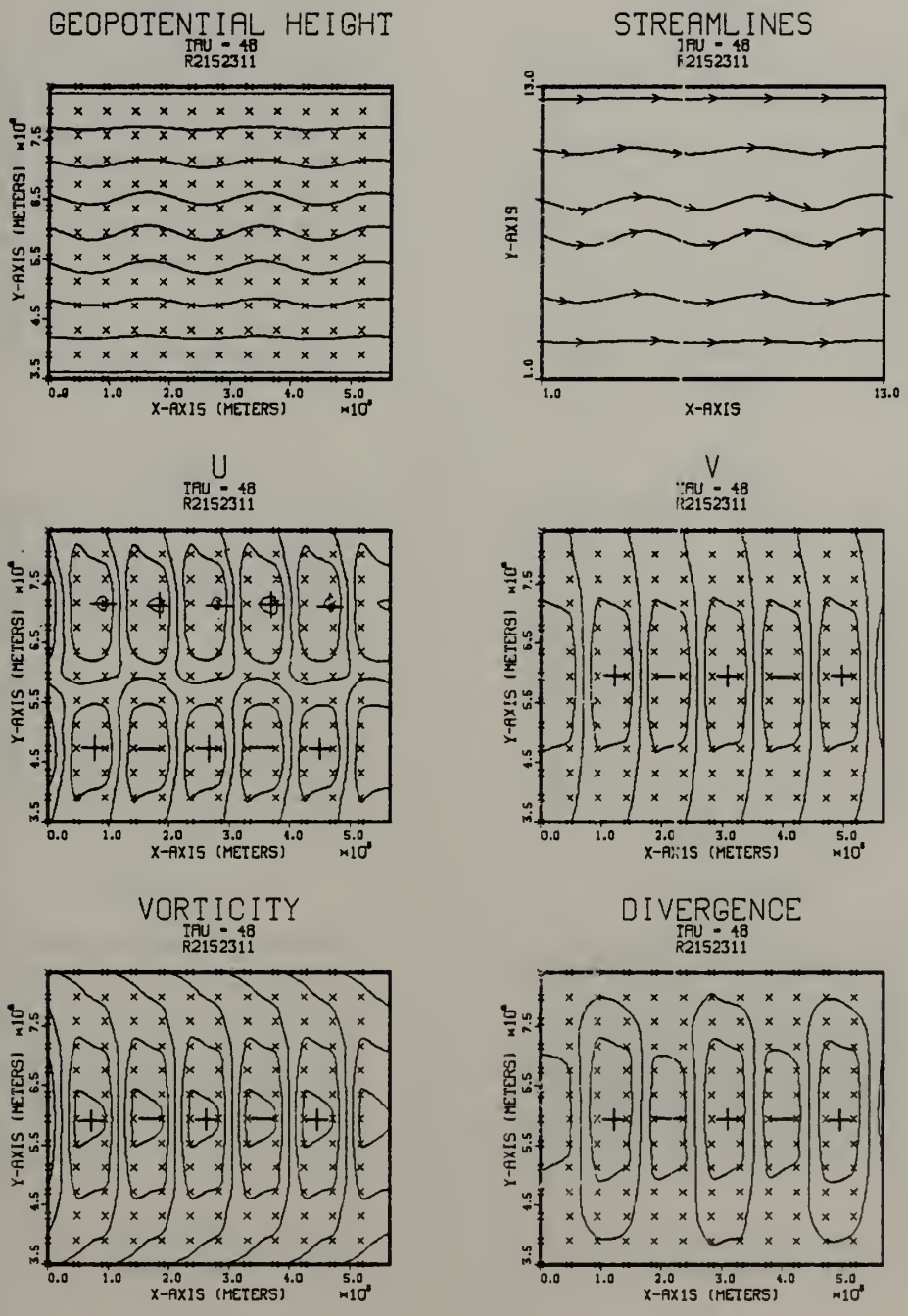


Fig. 15. As in Fig. 14 but a rectangular subdivision.

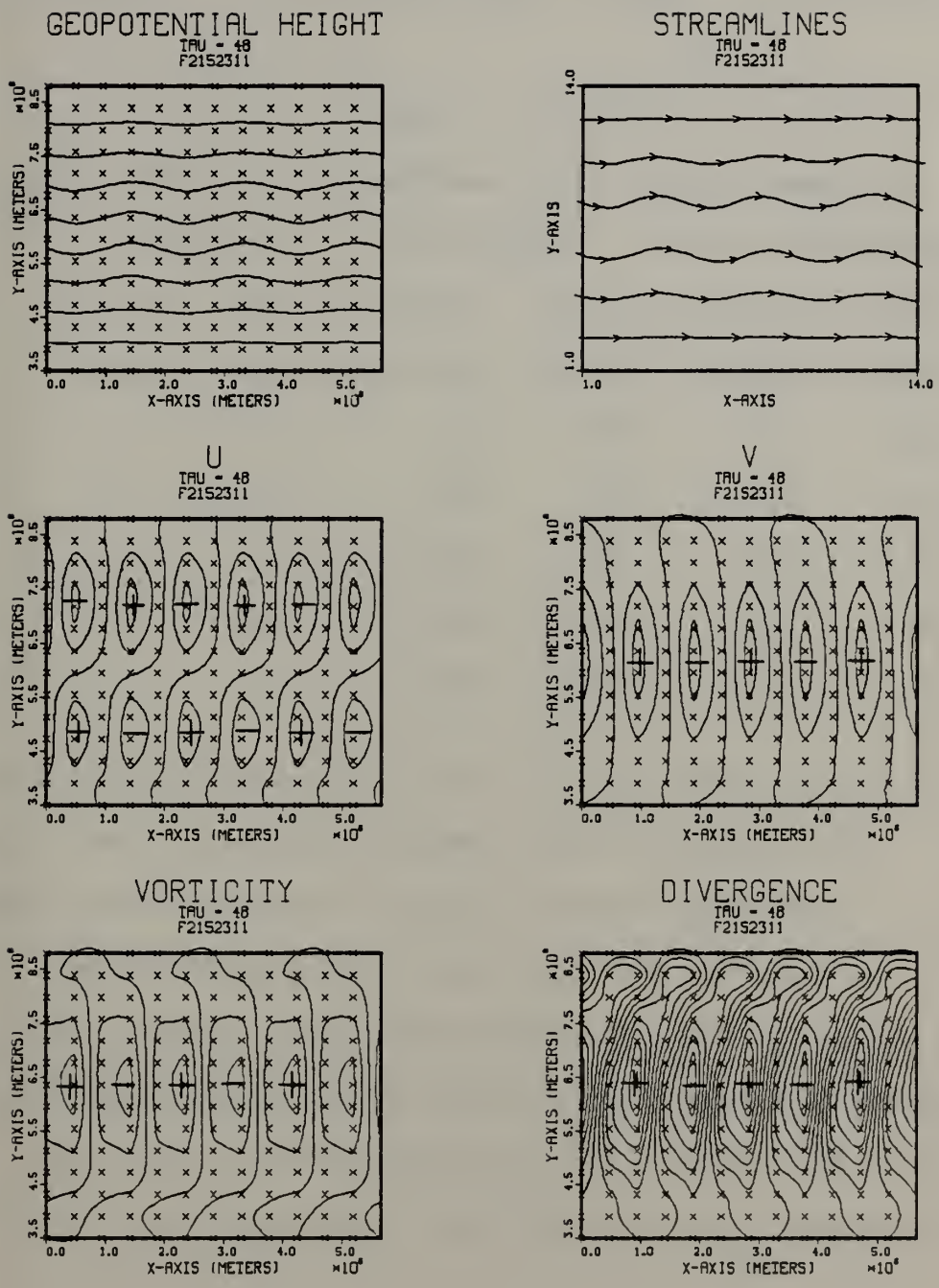


Fig. 16. As in Fig. 14 but a FDM model.

48-h v component amplitudes for wave number 3 in the x direction and the first six possible y modes are tabulated below.

TABLE 1

Harmonic analysis (v component m/s) - wave number 3

| | Triangles | | Rectangles | | Finite Difference | |
|---|---|---|---|---|---|---|
| Wave | Initial | 48-H | Initial | 48-H | Initial | 48-H |
| 1 | 2.12 | 2.14 | 2.20 | 2.22 | 2.20 | 2.20 |
| 2 | .01 | .04 | .01 | .02 | .01 | .09 |
| 3 | .41 | .43 | .44 | .44 | .44 | .42 |
| 4 | .00 | .00 | .00 | .00 | .00 | .00 |
| 5 | .05 | .06 | .06 | .06 | .06 | .05 |
| 6 | .00 | .00 | .00 | .00 | .00 | .00 |

The minor differences in the initial state amplitudes are due to the differences between the triangular and rectangular approximation for the initial conditions. However, the 48-h amplitudes show that the rectangular version has slightly better preserved the initial state amplitudes than either the triangular or finite difference models. The finite difference model has transferred more amplitude to the other modes, especially in the second y mode.

Figures 17 and 18 are the initial and 48-h GFEM model triangular subdivision forecasts for wave number 4. Wave number 4 is a severe test for this model. The energy

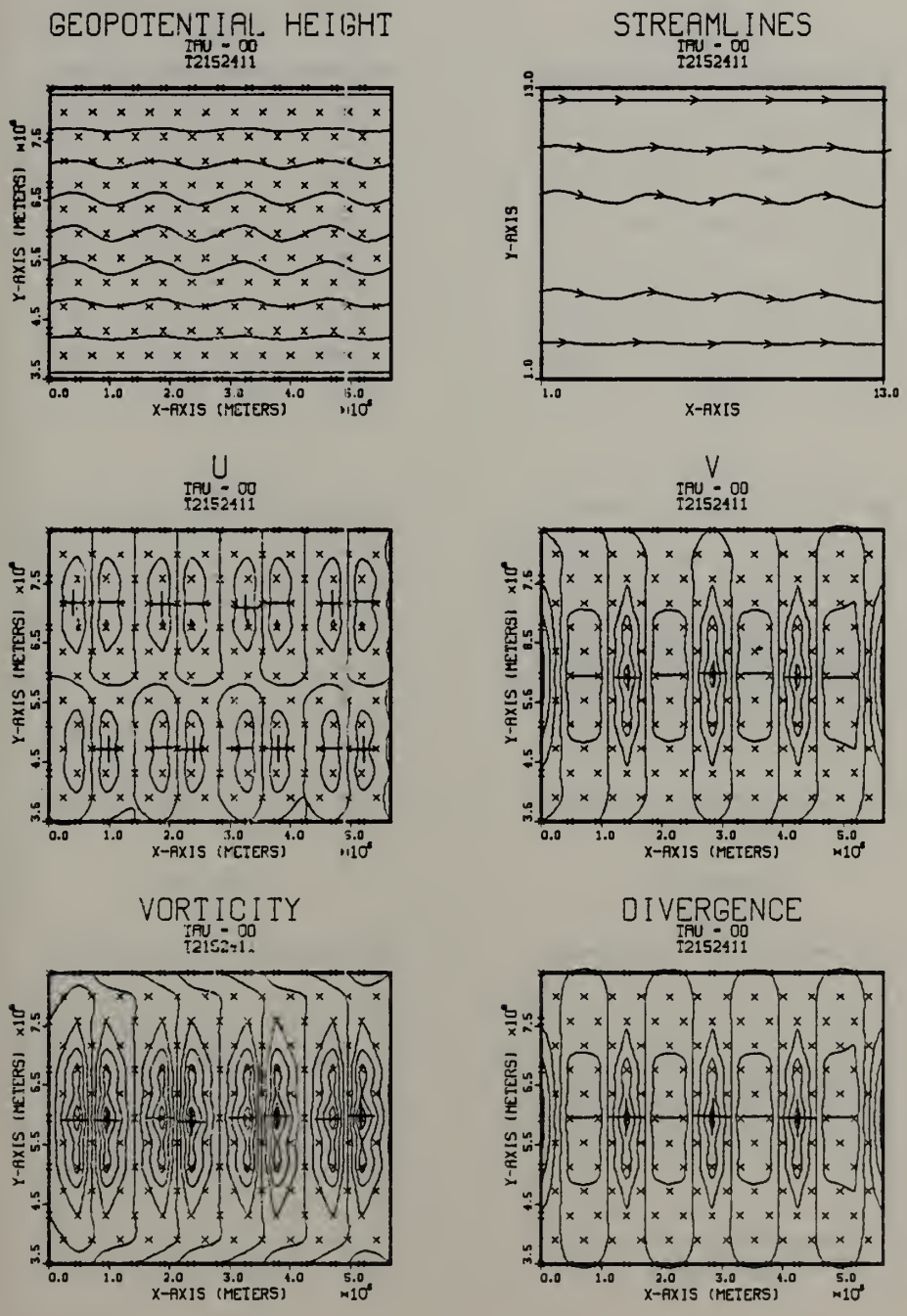


Fig. 17. As in Fig. 13 except for wave number four.

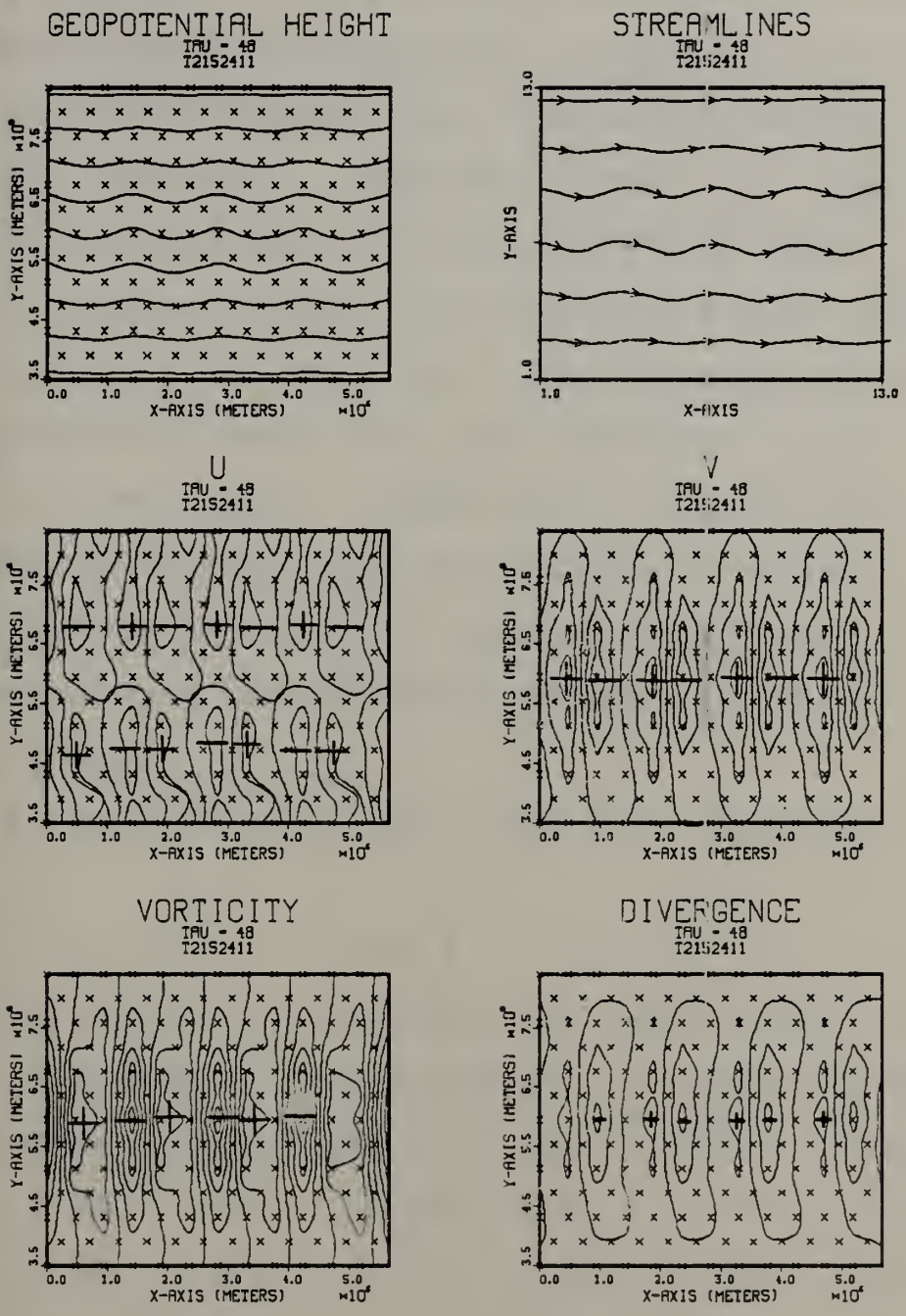


Fig. 18. As in Fig. 17 but a 48-h forecast.

transfer to other modes is readily apparent. Additionally, both the u component of the wind and the divergence show considerable noise at the boundaries. Figure 19 is the 48-h forecast for the rectangular model. No energy transfer nor noise at the boundaries is apparent in Figure 19. Figure 20 is the 48-h forecasts for the finite difference model. The asymmetry in the wave number three finite difference case is magnified for wave number four. The divergence field is heavily asymmetric. The u cells have developed a dipole from each original center. Comparisons of Figures 18, 19 and 20 show the superiority of the rectangular forecast. While the triangular version is noisy, it still has maintained the main features better than the finite difference model.

Table 2 is similar to Table 1 except for the wave number 4 case.

TABLE 2

Harmonic analysis (v component m/s) - wave number 4

| | Triangles | | Rectangles | | Finite Difference | |
|---|---|---|---|---|---|---|
| Wave | Initial | 48-H | Initial | 48-H | Initial | 48-H |
| 1 | 2.68 | 2.60 | 2.94 | 2.96 | 2.94 | 2.96 |
| 2 | .00 | .03 | .01 | .10 | .01 | .05 |
| 3 | .51 | .59 | .58 | .56 | .58 | .60 |
| 4 | .00 | .00 | .00 | .04 | .00 | .05 |
| 5 | .06 | .08 | .08 | .08 | .08 | .08 |
| 6 | .00 | .00 | .00 | .00 | .00 | .01 |

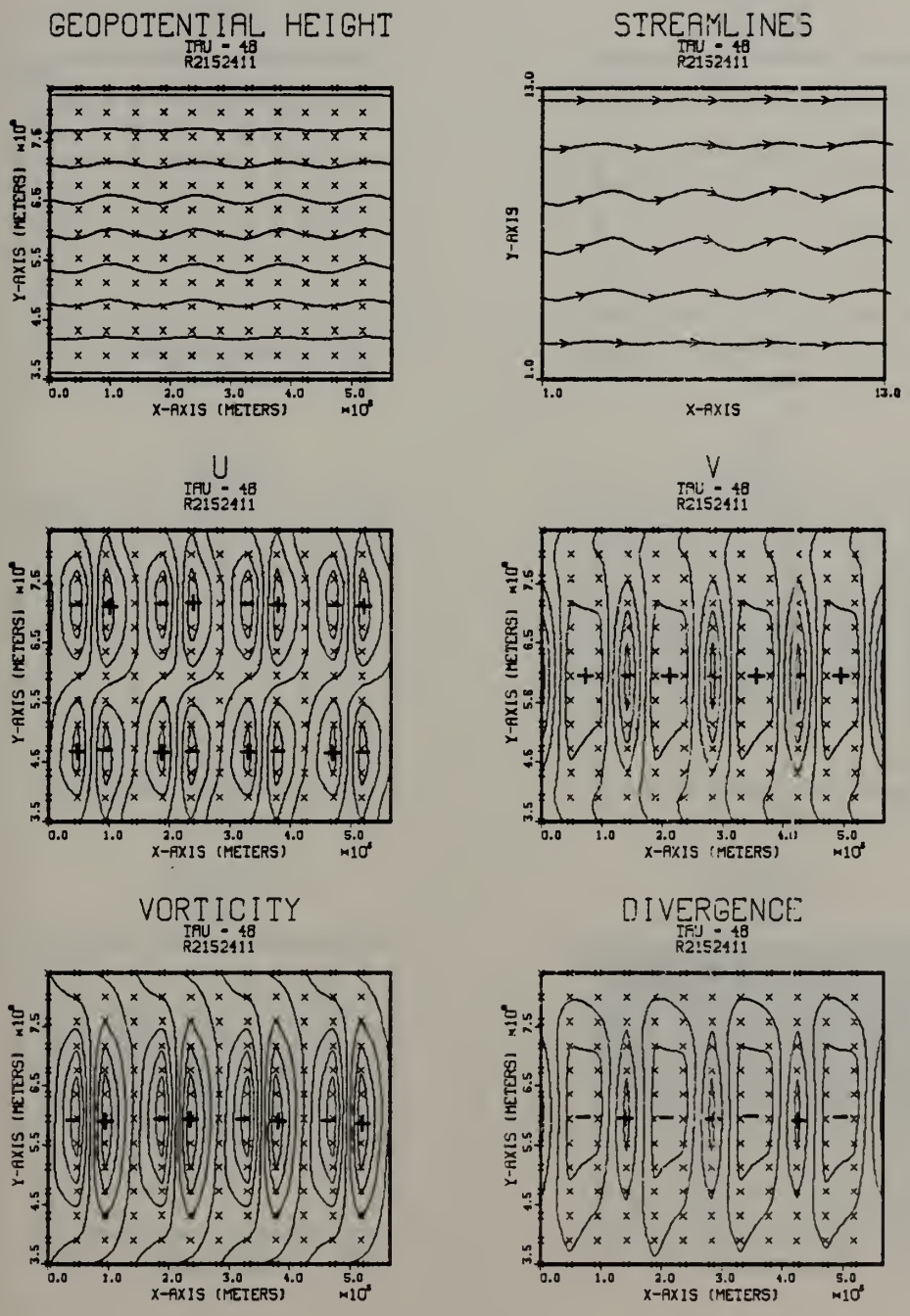


Fig. 19. As in Fig. 18 but a rectangular subdivision.

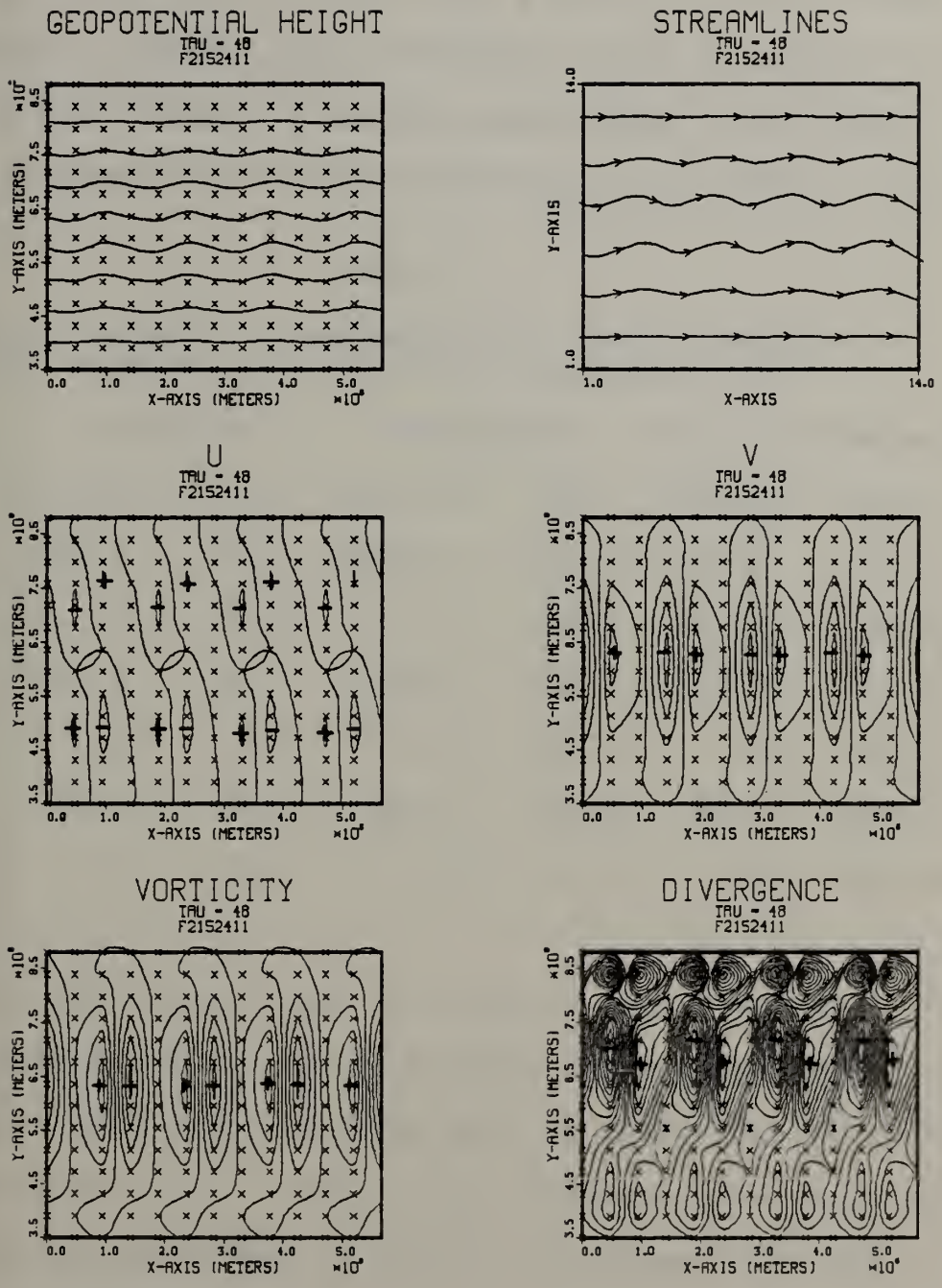


Fig. 20. As in Fig. 18 but a FDM model.

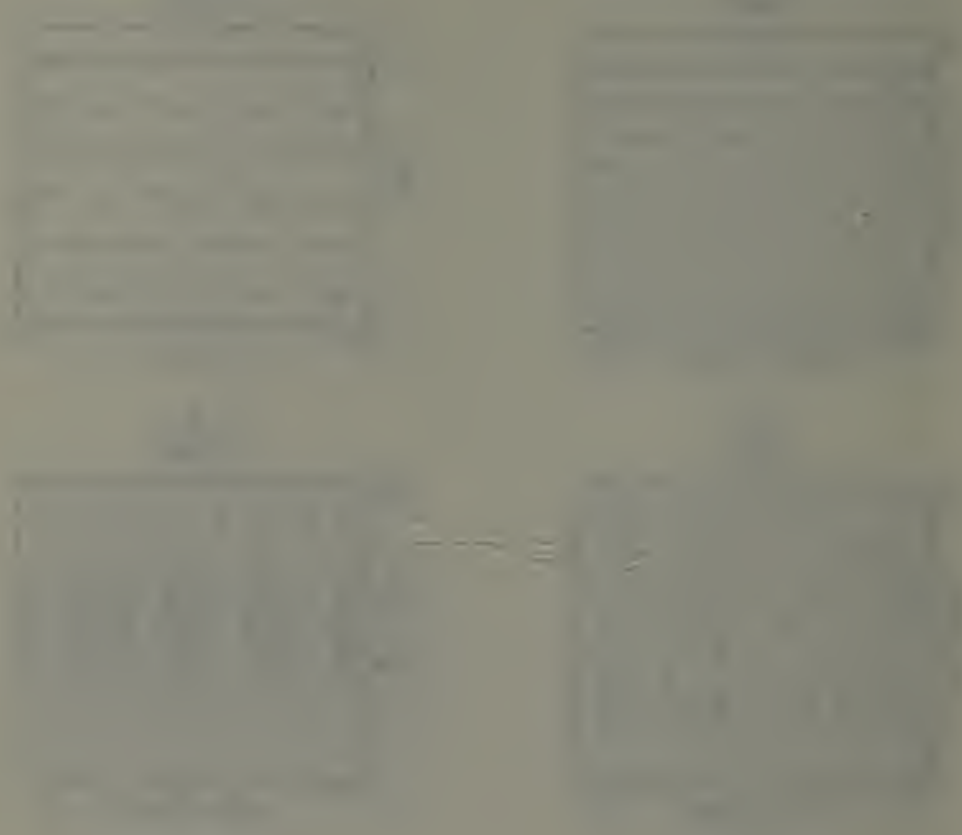

The harmonic analysis shows that the triangular version transfers more energy in the fifth y mode than does either other model. However, the rectangular model transfers more energy in the second y mode than does either other model. Table 3 compares the divergence for the wave number 4 case.

TABLE 3

Harmonic analysis (divergence $s^{-1}$) - wave number 4
(All numbers are scaled 10 to the minus 10.)

| | Triangles | | Rectangles | | Finite Difference | |
|---|---|---|---|---|---|---|
| Wave | Initial | 48-H | Initial | 48-H | Initial | 48-H |
| 1 | 2682.0 | 1741.0 | 2929.0 | 2179.0 | 2801.0 | 4462.0 |
| 2 | .0 | 140.8 | .0 | 207.5 | 447.4 | 5934.0 |
| 3 | 521.3 | 391.1 | 589.8 | 440.7 | 545.5 | 2314.0 |
| 4 | .0 | 20.5 | .0 | 81.2 | .0 | 923.5 |
| 5 | 62.6 | 60.5 | 84.4 | 56.8 | 68.7 | 1382.0 |
| 6 | .0 | 10.5 | .0 | 8.4 | .0 | 882.0 |

The finite difference model has greatly amplified the initial divergence. A choice between the triangular or rectangular grids version based only on these results would be purely subjective. However, the response of both grids at this high wave number in terms of divergence is highly superior to the FDM.

Figure 21 is the phase propagation diagram for the three models obtained from the double harmonic analysis. In all cases, the percentage propagation is for the first y mode and the appropriate x mode. The phase propagation diagram indicates that the triangular and rectangular models are comparable for the low wave numbers and diverge slightly at higher wave numbers. In all cases the GFEM models have better wave propagation than the FDM model.

The analysis performed on the uniform grids has shown that each GFEM model performs in a highly satisfactory fashion. There are minor differences in the phase propagation, while the rectangular version has an advantage in the control of energy transfers which manifest themselves in the divergence. The finite difference model performs as well as the GFEM models for the long waves. However, when forecasting the shorter waves, the finite difference model does not perform as well as either GFEM model.

## C. EXPERIMENT 2

This experiment will investigate two options for a variable grid. Atmospheric wave propagation on variable triangular and rectangular grids will be the test vehicle. Since this FDM model has no capability on a variable grid, it will not be evaluated during this experiment. The comparisons will be between a rectangular and triangular GFEM model.

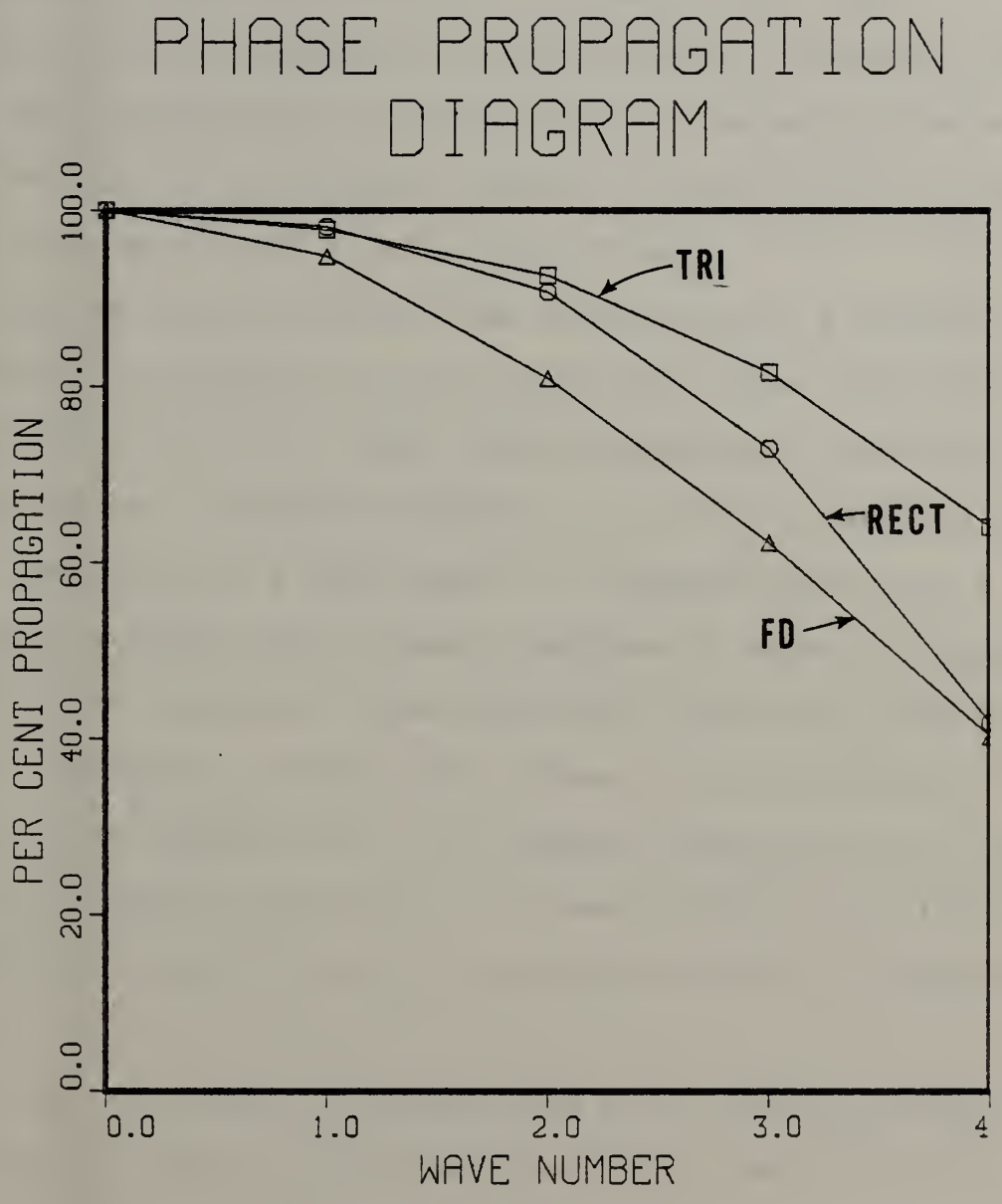


Fig. 21. Phase propagation diagram for the triangular, rectangular and finite difference models from Experiment 1.

There are many criteria for determination of a suitable variable grid. Both rectangles and triangles allow a successful implementation of a variable grid. One criterion is the accuracy of resolving the atmospheric waves that move through the variable grid. A second criterion is the increase in resolution. Another consideration is the ease with which the grid can be refined.

Cullen (1979) stressed the importance of a smooth variation in element size when increasing the resolution from coarse to fine. Older (1981) developed a technique for transforming a uniform triangular grid into a variable grid when working with a GFEM model. He demonstrated that a smoothly varying grid allowed atmospheric waves to propagate through the transition zone with much less noise generation than an abruptly varying grid. Some finite difference models with nested grids, for example Harrison (1973), have abruptly varying resolution. A generalization of Older's techniques allows a similar transformation for a rectangular grid.

The test cases for experiment 2 will be for a simple atmospheric wave. A mean depth of 5 km, a mean flow of 10 m/s, wave number one and a perturbation of 1.0 m/s are employed.

D. RESULTS 2

The ability to refine a grid should be easily achieved. The method of transforming from a uniform grid to smoothly varying should allow one to choose not only what degree of refinement but also where the refinement occurs. Older (1981) developed a transformation method based on

$$X = x + A \cos Kx$$

where

$X$ = the transformed grid

$x$ = the original grid

$A$ = a constant

$k = 2\pi/L$.

Woodward (1981) modified the transformation to include a

$$- \sin^2 \frac{kx}{2}$$

for the longitudinal stretching. A trignometric identity is employed yielding

$$X = x + A(1 - \cos kx)$$

This research added the capability to control the location of the refinement through

$$X = x + A(1 - \cos(kx + \delta))$$

The map factor $\frac{\partial X}{\partial x}$ is defined by

$$\frac{\partial X}{\partial x} = 1 + kA \sin(kx + \delta)$$

The maximum and minimum values are

$$\frac{\partial X}{\partial x}_{max} = 1 + kA, \quad \frac{\partial X}{\partial x}_{min} = 1 - kA$$

The ratio R of maximum map factor to minimum map factor is

$$R = \frac{1+kA}{1-kA}$$

Solving for A yields

$$A = \frac{R-1}{k(R+1)}$$

For purposes of this experiment R was chosen to vary from 1.0 to 4.0. A value of R = 4 implies that the minimum X is one fourth of the maximum X. The Y transformation is performed in a similar fashion except that Y = y + B sin Ly is employed where

Y = the transformed grid,

y = the original grid,

B = a constant, and

L = $2\pi/W$

Placement of the high resolution is accomplished by determining the value of $\delta$ required to place the minimum map factor as desired. For instance, if the refined grid is desired in the middle of the channel (L/2) then $\delta$ would be equal to $\pi/2$.

Figure 22 is the 48-h forecast with the triangular subdivision for a uniform grid. This forecast will act as the control for the triangular cases. Figure 23 is the triangular subdivision, 48-h forecast with R = 2.0. Figure 24 is the triangular subdivision, 48-h forecast with R = 3.0. Figure 25 is the triangular subdivision, 48-h forecast with R = 4.0. All of the 48-h u and v fields appear identical. This indicates that there is no degradation in forecast skill when using the same number of degrees of freedom and locating many of those unknowns into a refined area. There is no noise apparent in the transition regime. However, there are definite differences in the divergence field, although the magnitude of the maximum/ minimum value of divergence is relatively small ($1.0 \times 10^{-8}$ $s^{-1}$).

Table 4 shows the harmonic analysis amplitudes of the geopotential fields for the different triangular cases. The relationship between initial and final amplitudes remains the same regardless of the degree of variability. The phase propagation of the v field in the control case is 97.7%, whereas it is 96.7%, 95.4% and 94.1% for R values of 2, 3 and 4. The variation from the control of the phase propagation with grid refinement is under four percent.

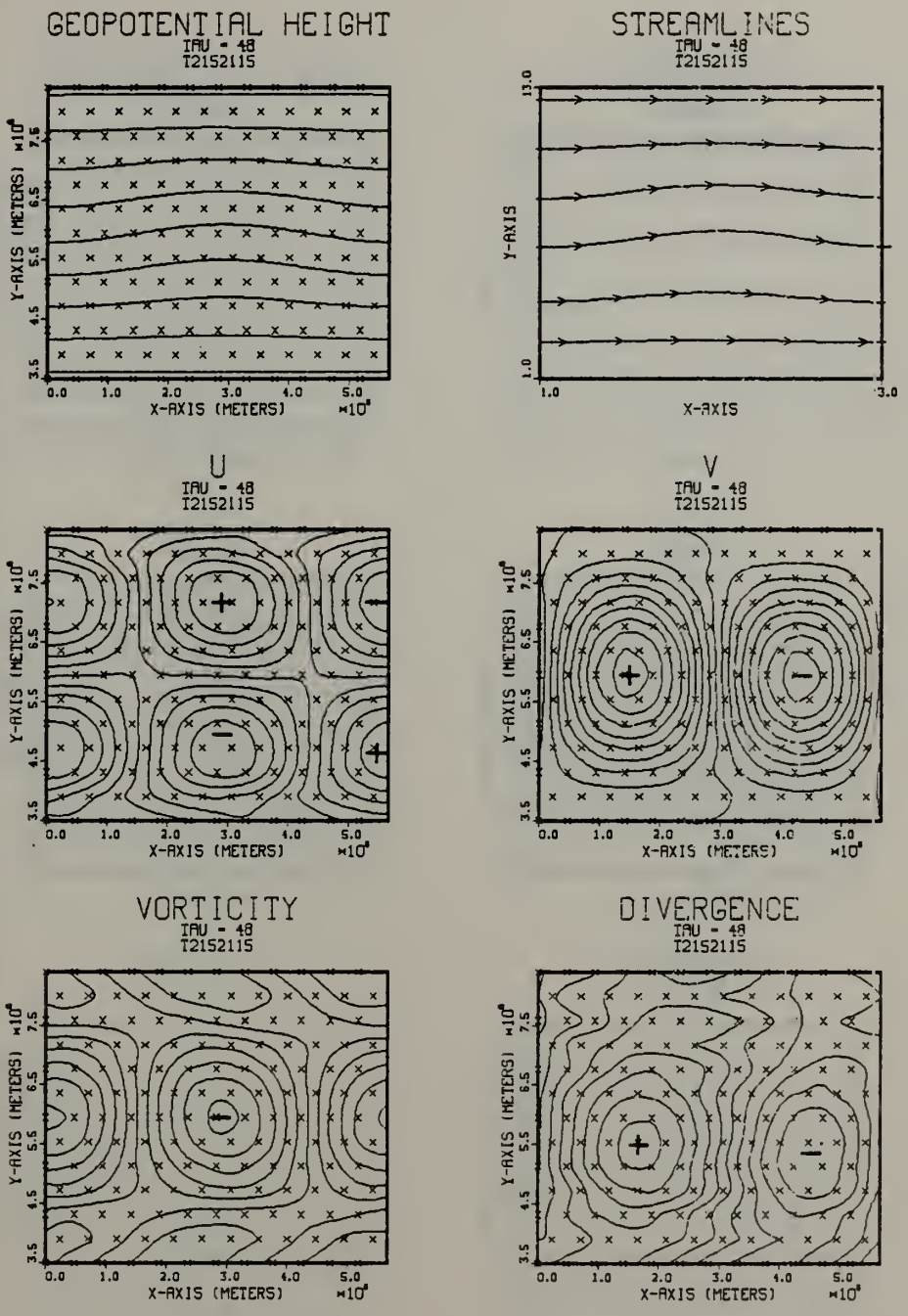


Fig. 22. As in Fig. 6 for R = 1.0. Contour intervals are 600 $m^2/s^2$ for geopotential height, .2 m/s for u and v, $.6 \times 10^{-6}$ $s^{-1}$ for vorticity and $.6 \times 10^{-8}$ $s^{-1}$ for divergence.

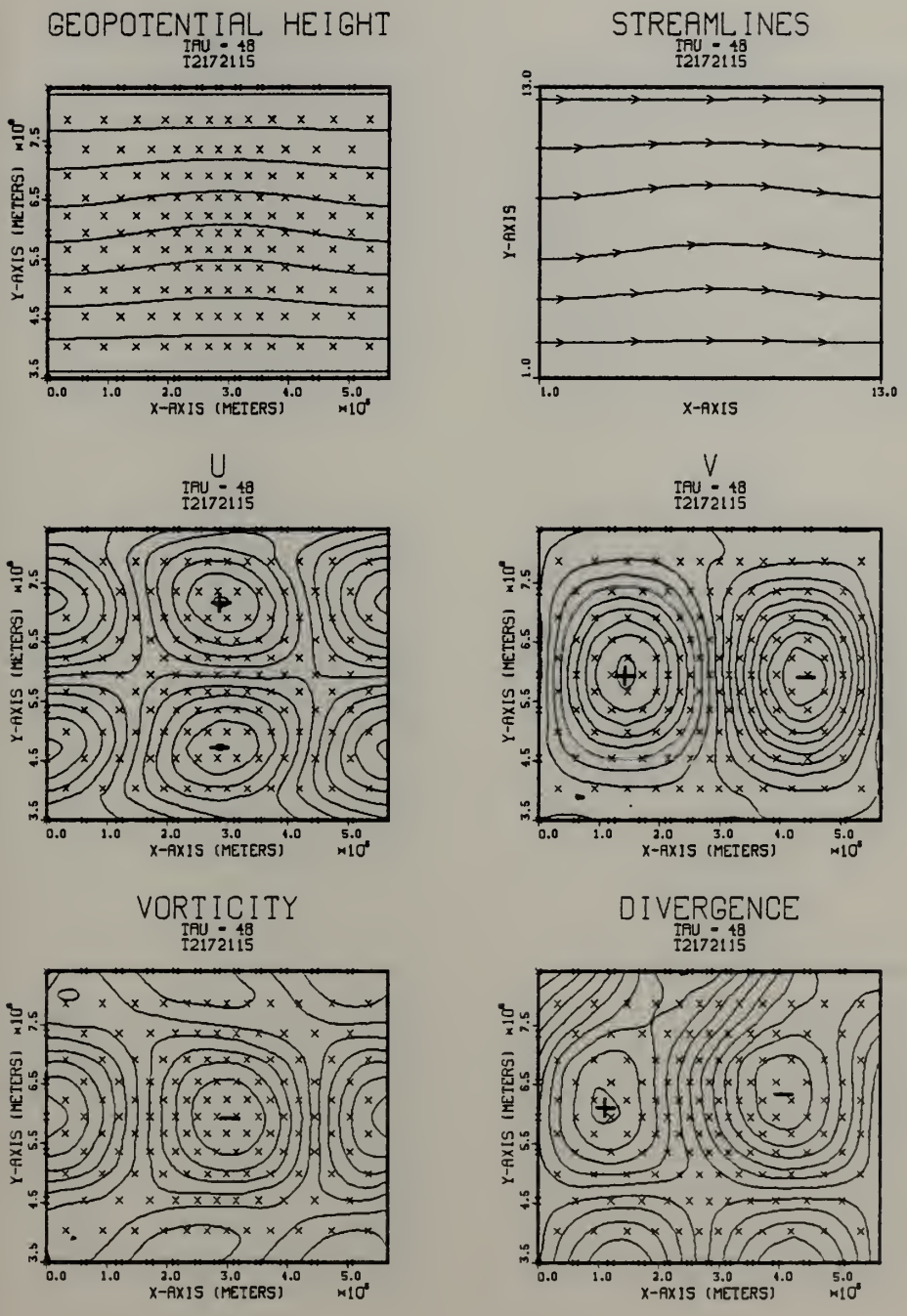


Fig. 23. As in Fig. 22 for R = 2.0.

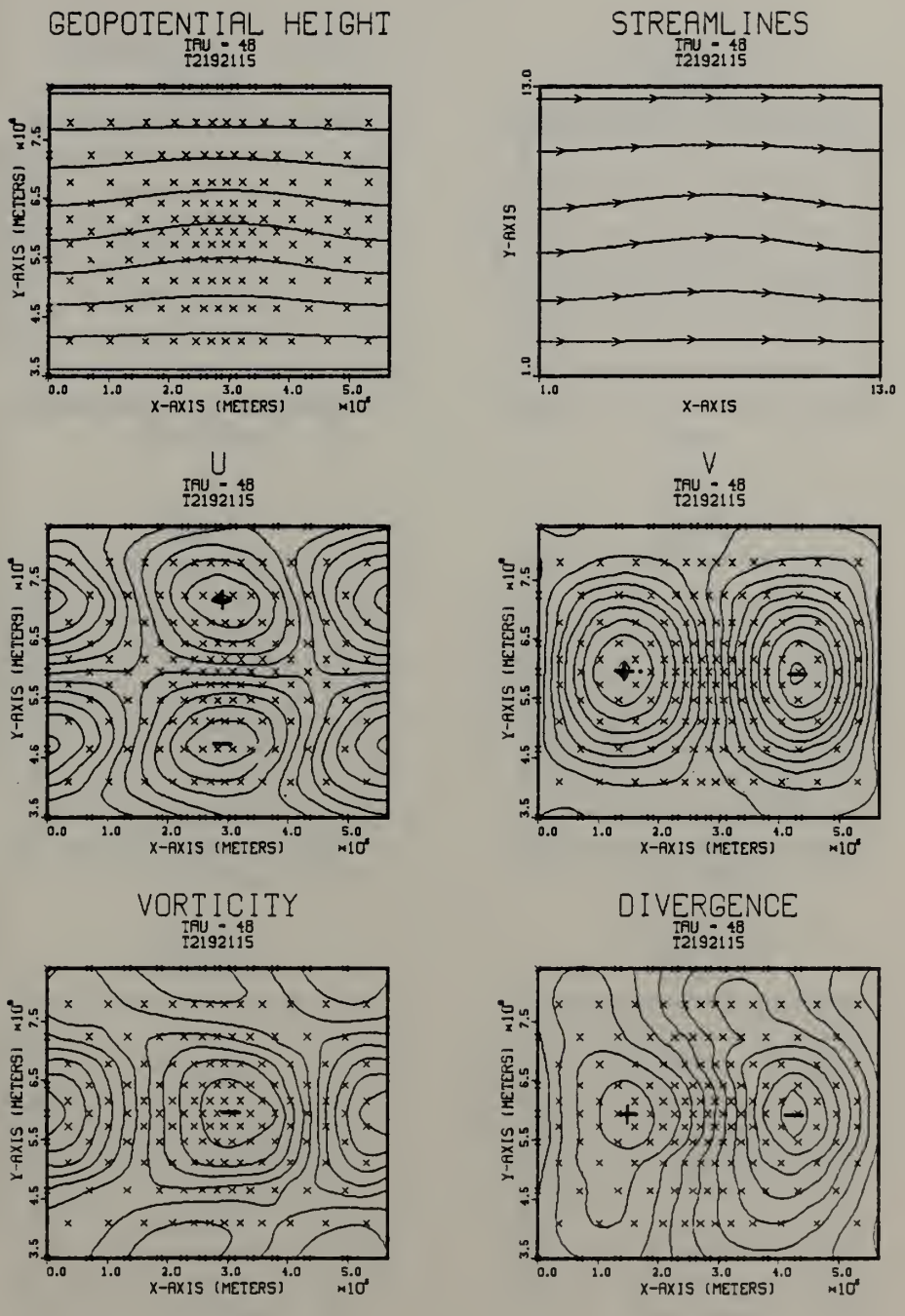


Fig. 24. As in Fig. 22 for R = 3.0.

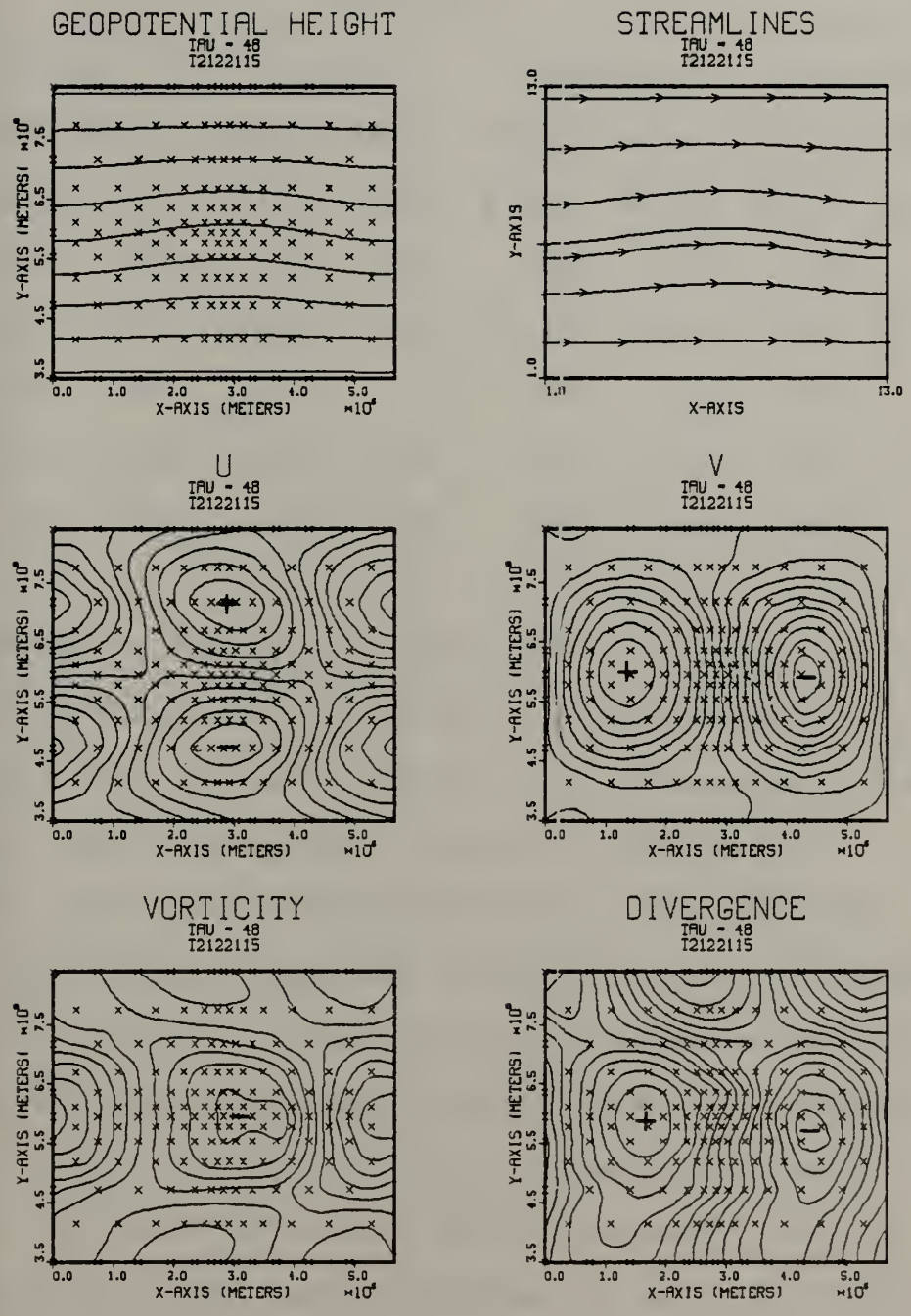


Fig. 25. As in Fig. 22 for R = 4.0.

TABLE 4

Harmonic Analysis (Geopotential $m^2/s^2$)

Triangles

| | R = 1.0 | | R = 2.0 | | R = 3.0 | | R = 4.0 | |
|---|---|---|---|---|---|---|---|---|
| Wave | Initial | 48-H | Initial | 48-H | Initial | 48-H | Initial | 48-H |
| 1 | 67.98 | 67.16 | 67.91 | 64.65 | 67.91 | 64.95 | 67.91 | 63.70 |
| 2 | .00 | .55 | .00 | .69 | .00 | .99 | .00 | .57 |
| 3 | 13.55 | 12.90 | 13.45 | 12.55 | 13.41 | 13.24 | 13.29 | 11.16 |
| 4 | .00 | .21 | .00 | .37 | .00 | .54 | .00 | .28 |
| 5 | 1.90 | 1.70 | 1.67 | 1.30 | 1.33 | 1.62 | 1.32 | 1.38 |
| 6 | .00 | .16 | .00 | .23 | .00 | .36 | .00 | .21 |

Figure 26 is the control case for the rectangular version, 48-h forecast. Figure 27 is the rectangular subdivision, 48-h forecast with R = 2.0. Figure 28 is the rectangular subdivision, 48-h forecast with R = 3.0. Figure 29 is the rectangular subdivision, 48-h forecast with R = 4.0. Close inspection reveals no noise in either the $\phi$, u or v fields. No degradation in forecast skill has been observed due to increased resolution with a rectangular subdivision. All $\phi$, u and v fields are very similar in structure. The main difference in the forecasts lies in the divergence field where the magnitudes are small ( $10^{-8}s^{-1}$) because of the specified mean depth.

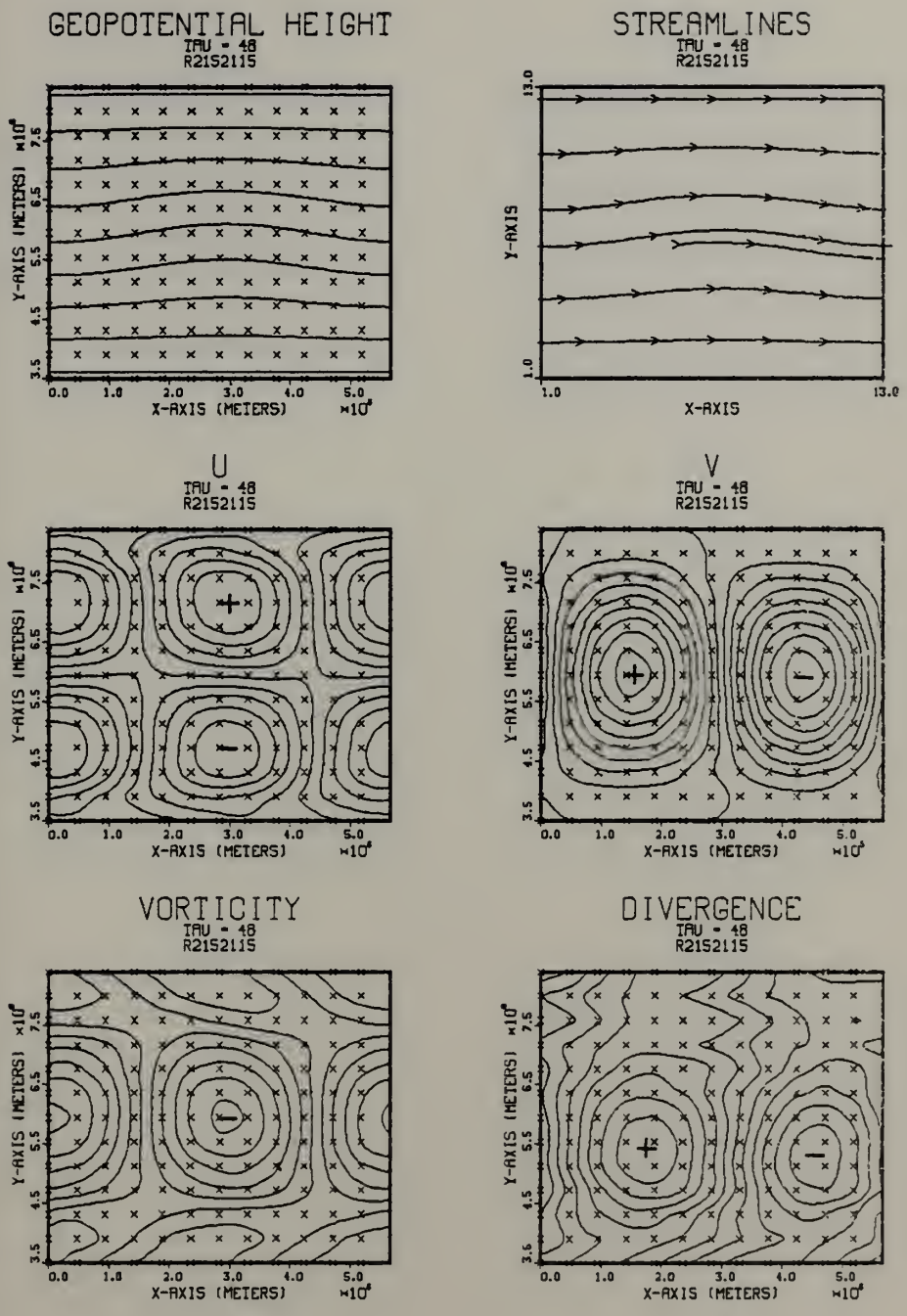


Fig. 26. As in Fig. 7 for R = 1.0. Contour intervals are 600 $m^2/s^2$ for geopotential height, .2 m/s for u and v, $.6 \times 10^{-6}$ $s^{-1}$ for vorticity and $.6 \times 10^{-8}$ $s^{-1}$ for divergence.

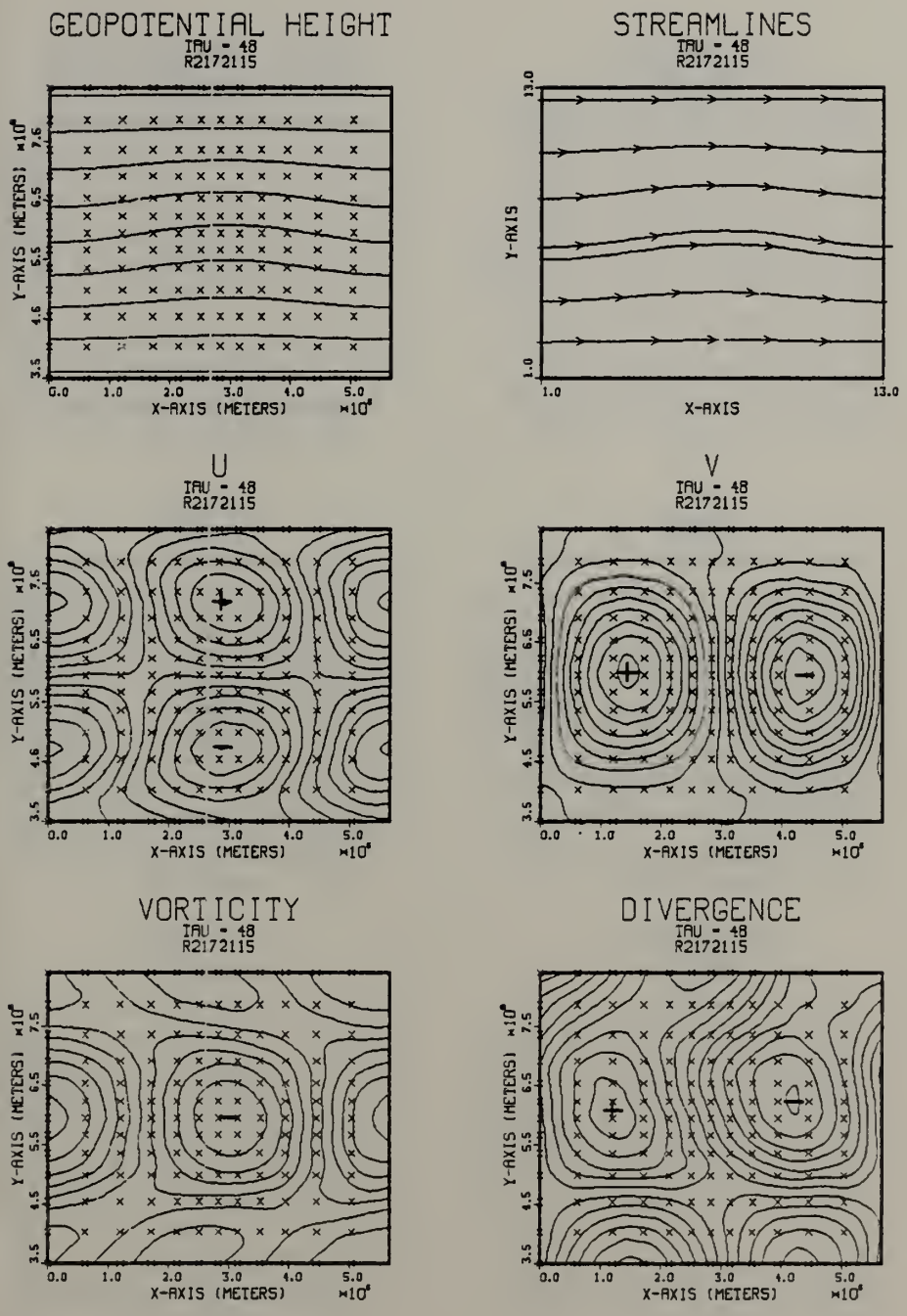


Fig. 27. As in Fig. 26 for R = 2.0.

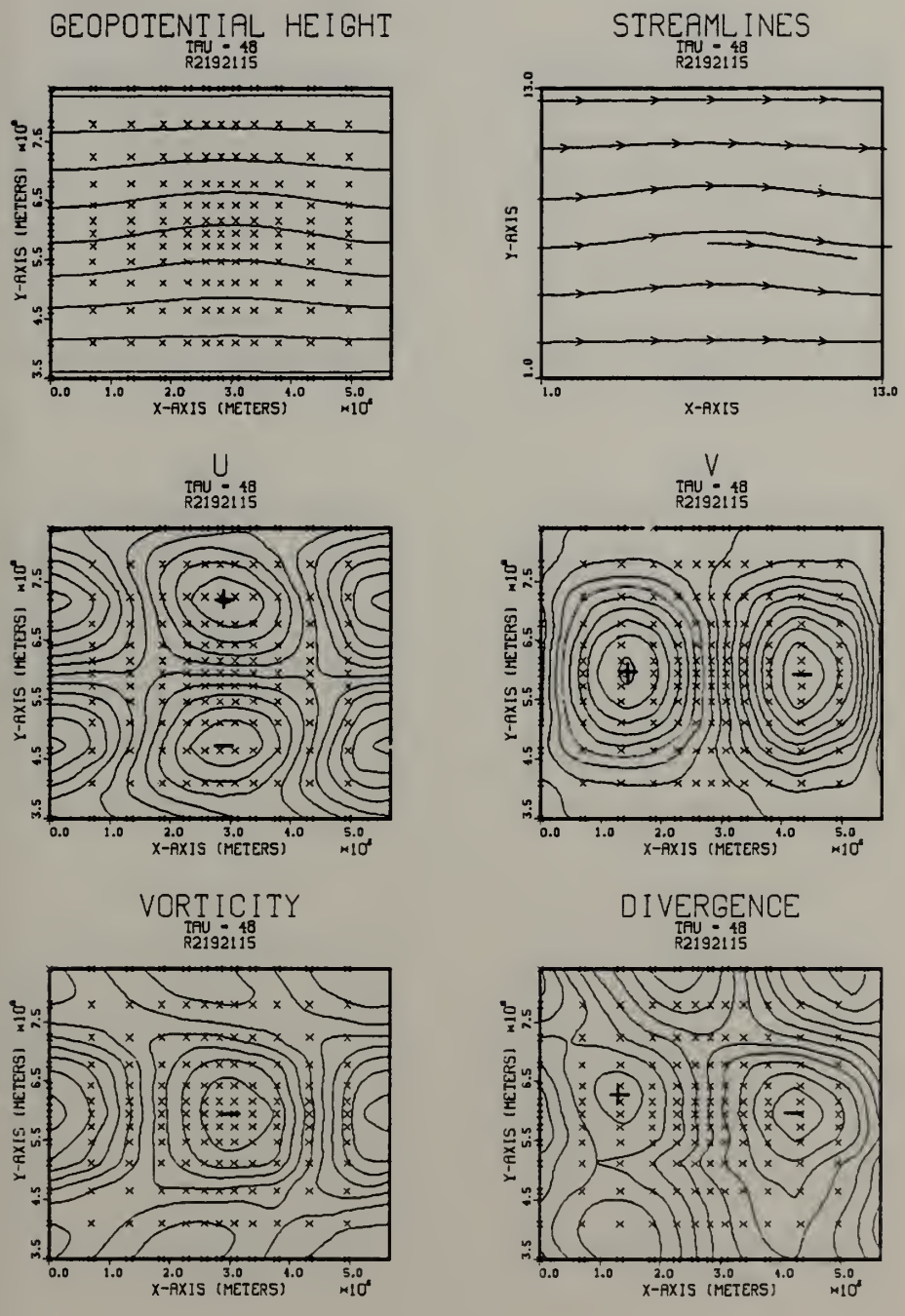


Fig. 28. As in Fig. 26 for R = 3.0.

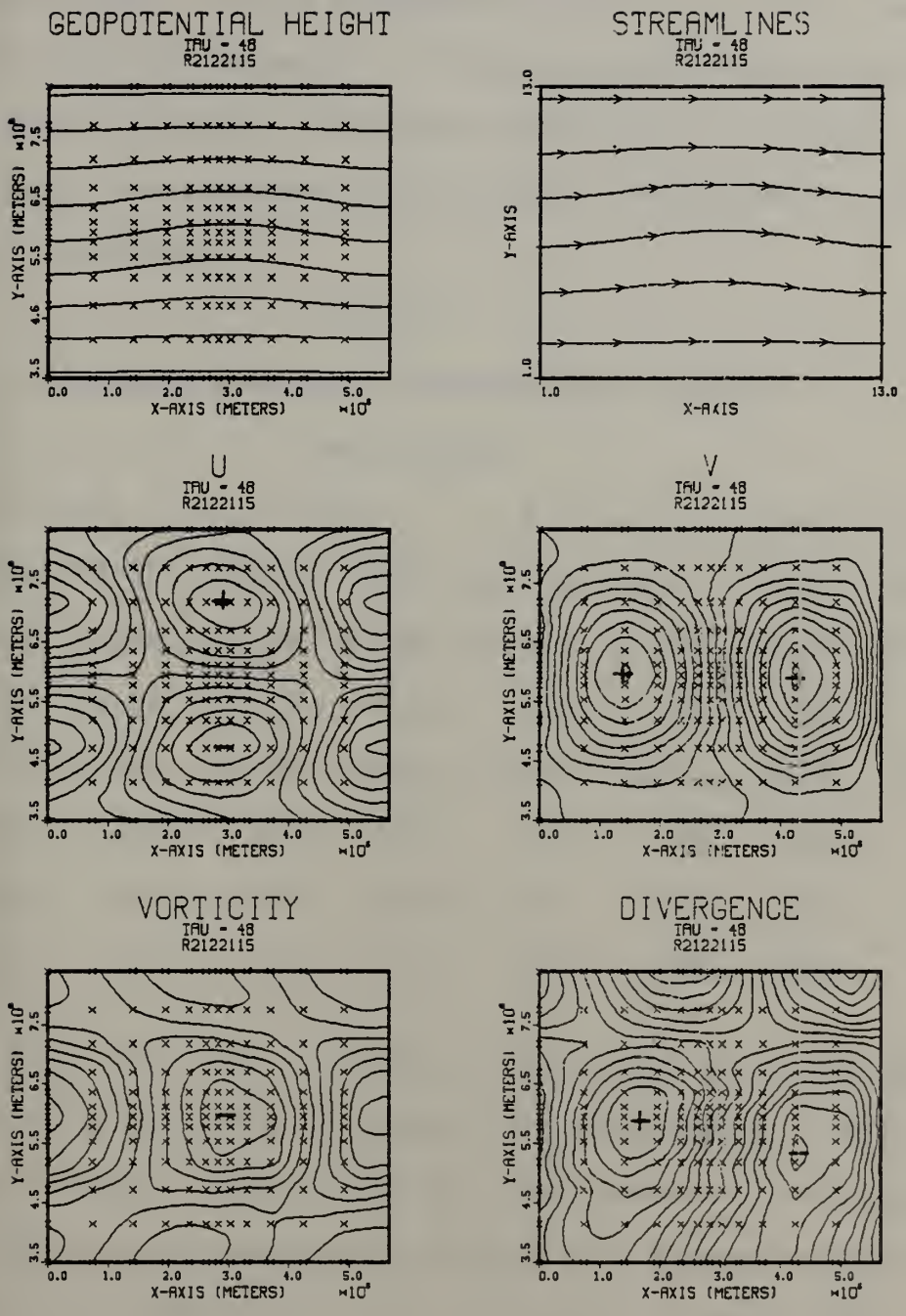


Fig. 29. As in Fig. 26 for R = 4.0.

Table 5 is similar to Table 4 except for the rectangular cases. Phase propagation for the control case v field is 98.0%, whereas it is 98.3%, 98.1%, and 97.9% for R values of 2, 3, and 4. The variation from the control case of the phase propagation with grid refinement is less than half a percent.

TABLE 5

Harmonic Analysis (Geopotential $m^2/s^2$)

Rectangles

| | R = 1.0 | | R = 2.0 | | R = 3.0 | | R = 4.0 | |
|---|---|---|---|---|---|---|---|---|
| Wave | Initial | 48-H | Initial | 48-H | Initial | 48-H | Initial | 48-H |
| 1 | 68.03 | 67.48 | 67.98 | 65.26 | 68.22 | 66.45 | 68.14 | 66.34 |
| 2 | .01 | 1.00 | .03 | .36 | .00 | .85 | .00 | 1.22 |
| 3 | 13.59 | 12.95 | 13.39 | 13.26 | 13.49 | 13.81 | 13.36 | 12.39 |
| 4 | .01 | .46 | .05 | .22 | .01 | .48 | .00 | .43 |
| 5 | 1.92 | 1.81 | 1.57 | 1.64 | 1.54 | 1.59 | 1.46 | 1.19 |
| 6 | .02 | .23 | .07 | .04 | .01 | .30 | .00 | .22 |

The tests thus far indicate a successful grid refinement capability for both triangles and rectangles. There are neither drastic impairments nor improvements in either phase propagation or amplitude changes for either technique. Neither version stands out above the other although the rectangular version has less phase propagation variation and better amplitude conservation. Both versions allow comparable grid refinement through the use of the procedure

previously described. Both allow an easy and straightforward implementation of the procedure.

However, there is a more fundamental difference between the versions. Operators, such as a simple derivative, have weighting coefficients associated with finite element applications as well as with finite difference schemes. For instance, a simple-centered, one-dimensional finite difference derivative has weights of 1/2 and -1/2. The finite element weights are identical to the finite difference weights in this one-dimensional case. The weights can similarly be computed for two-dimensional operators such as a Laplacian. The quadrature formulas used to determine the weights are explained in more depth in Appendix B. The geometry of the triangles affects the weights. For instance, the two-dimensional Laplacian applied to a finite element application on an equilateral triangular subdivision gives weights of 1/6 to all surrounding points, and -1 to the center point, as indicated in Figure 30. However, the weights change if a triangle with a height equal to one half the base is employed as shown in Figure 31. The fact that some weights are zero is a strong cause for alarm. If the triangles are flattened further, the farthest end point weights become negative. This is strictly a function of the geometry of the triangle and is a clear sign that use of the triangles warrants extreme caution. In fact, Williams

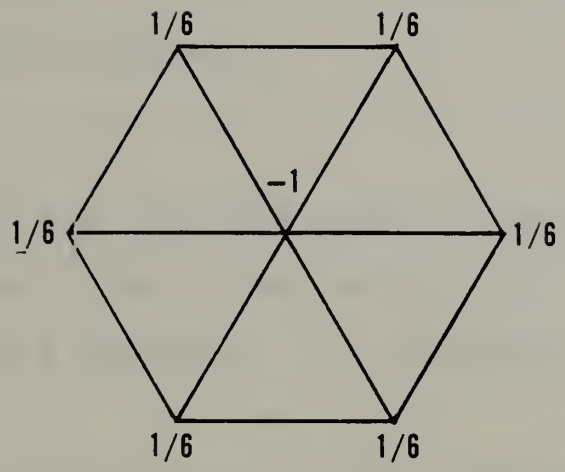


Fig. 30. Weights associated with a Laplacian operator for a triangular subdivision using equilateral triangles.

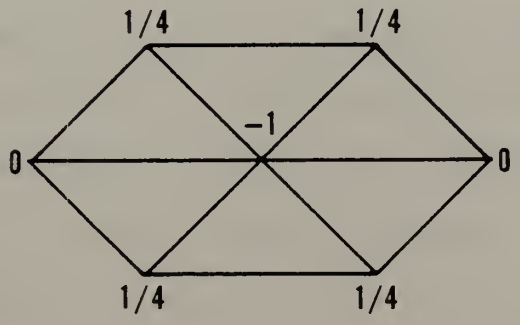


Fig. 31. Weights associated with a Laplacian operator for a triangular subdivision using triangles with a base equal to twice the height.

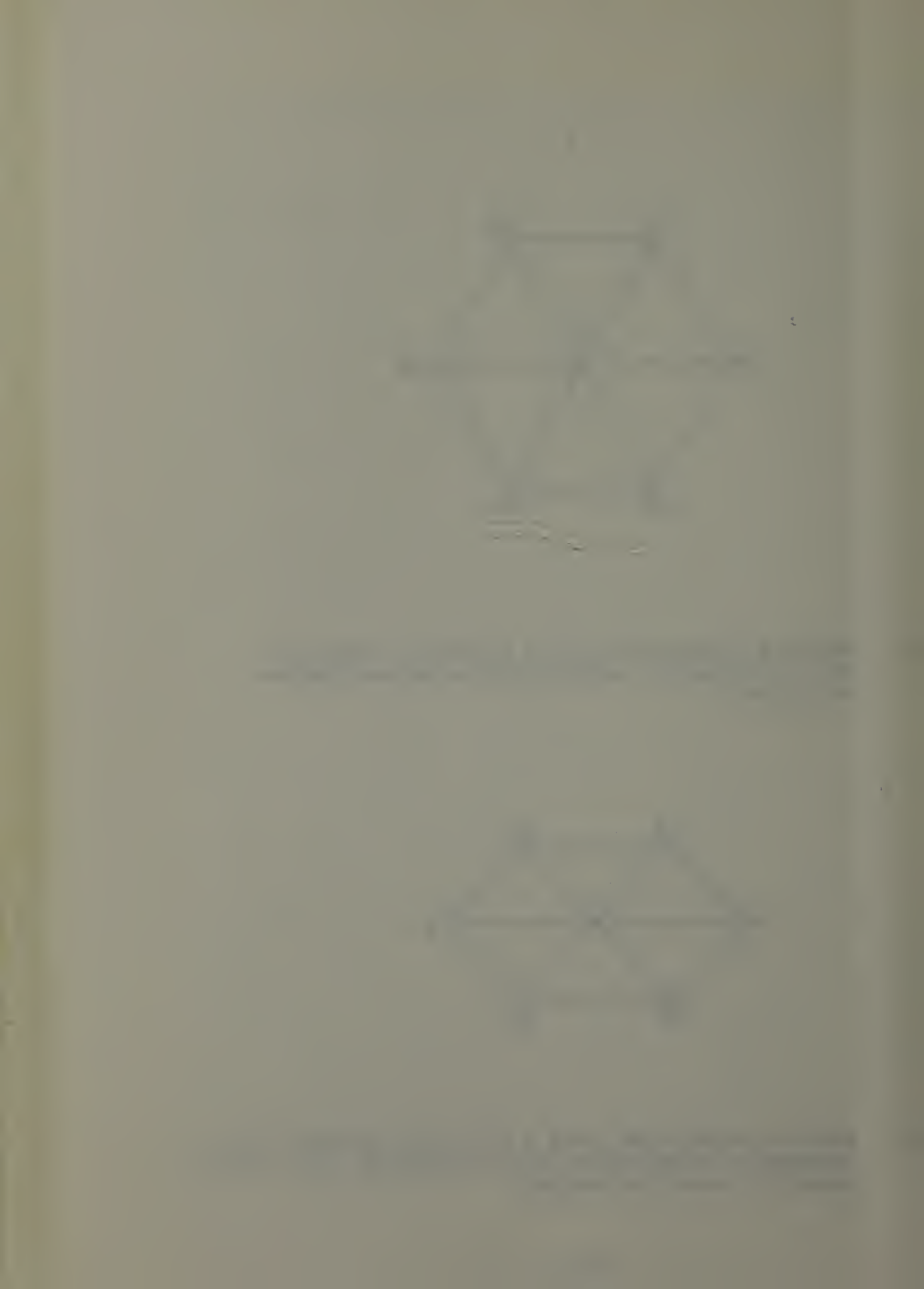

(unpublished notes) has determined that the geometry of the triangles dictates that unless a triangle with at least two equal sides (isosceles) is employed the boundary conditions will not be exactly satisfied.

## E. EXPERIMENT 3

The capability of the GFEM model to resolve atmospheric phenomena near the scale of the smallest grid length will be demonstrated. This experiment is in response to Task II of the hypothesis.

The ultimate motivation for any "improvement" in a model is a better forecast. During the past decade, improvements have come, to a certain degree, by increased resolution. While it is intuitively obvious that increased resolution will improve a forecast, demonstrations have not been made to show how the model resolves features near the smallest grid length. Staniforth and Mitchell (1978) increased the resolution with a variable grid but resolved a synoptic scale feature in a 37x37 uniform fine mesh area.

In this experiment, a source term simulating a mass source is added to the continuity equation. An expression for the source term in terms of a wave form is derived by theoretical means. The wave form allows a very small scale feature to be simulated. A detailed description of this procedure can be found in Chapter IV-D-2. By assuming the

wave is in equilibrium and steady state, the solution and source are known for all time when the Rossby number is small.

The development of the source term expression followed traditional quasi-geostrophic theory. One requirement for quasi-geostrophic theory is that the Rossby number be small. In the linear case, the Rossby number will be approximately 0.1. However, in the nonlinear case the Rossby number is approximately 0.4 and the quasi-geostrophic theory assumption is violated.

The first test will be on a uniform grid for the rectangular GFEM and finite difference models and the second test will be on a variable rectangular grid GFEM model. High resolution versions of the uniform test will be run and act as the control. A mean depth of 5 km was selected. Perturbations of 2.5 m/s and 25 m/s upon a mean flow of 10 m/s will be evaluated for the uniform grid. This will allow both the linear and nonlinear aspects of the different models to be observed. Here linearity is implied by the smallness of the perturbation amplitude. The source term solution is nonlinear and nonlinear interactions do occur when the amplitude is small. Each test will be integrated for 96 h of forecast time. A perturbation of 25 m/s upon a mean flow of 10 m/s will also be evaluated for the variable grid.

The main thrust of this experiment is to determine the grid-scale sensitivity for the GFEM model and the equivalent finite difference model. Sensitivity will be measured by insertion of a source term into the continuity equation. However, the theoretical development presented in Chapter IV-D-2 is for the rotational component of the wind. Because the initial conditions for u and v are non-divergent, the divergence in the model must increase from a zero initial state. This increase will require an adjustment process. This serendipity effect will be exploited during the comparisons.

The linear cases examined represent a small-scale short wave embedded in a long wave pattern. Using a small perturbation for the first tests will establish a level of confidence that each model responds to the source term creditably. The nonlinear cases represent an active vortex in a mean flow. The maximum u component is 35 m/s which is hurricane/typhoon strength. Physically, the source term in the divergence field opposes the advection of the vorticity field, and "anchors" the steady-state vorticity solution.

In either the linear or nonlinear tests, the source term is nonlinear. By constraining the perturbation to be small, the source term plays a linear role. However, when the perturbation is large, the source term allows full nonlinear interactions.

F. RESULTS 3

1. Linear Case - Uniform Grids

Figures 32 and 33 are the initial and 96-h forecasts for the rectangular GFEM model. There are 156 degrees of freedom in these forecasts. The initial v field has a maximum value of $\pm$2.27 m/s across a separation of 4 increments. The initial u field maximum and minimum are 12.5 m/s and 7.5 m/s. The source term is shown in the initial fields and remains constant throughout the integration. The divergence value increased to a steady state solution during the first 12 hours with an oscillation that died out after hour 24. Figure 34 is the equivalent finite difference 96-h forecast. Figure 34 demonstrates that the finite difference model performs well for these initial conditions. Figure 35 is the high-resolution 96-h forecast for the rectangular GFEM model. Close inspection of Figures 33 and 35 shows little difference. The low resolution forecast with 156 degrees of freedom has converged to the high resolution forecast with 600 degrees of freedom. Figure 36 is a graph of v component amplitudes at hour 96 as a function of x and y wave numbers for the low and high resolution and finite difference models. The high resolution (S253115) and low resolution (S153115) forecasts are in excellent agreement. However, the FDM (F153115) forecast departs from the control

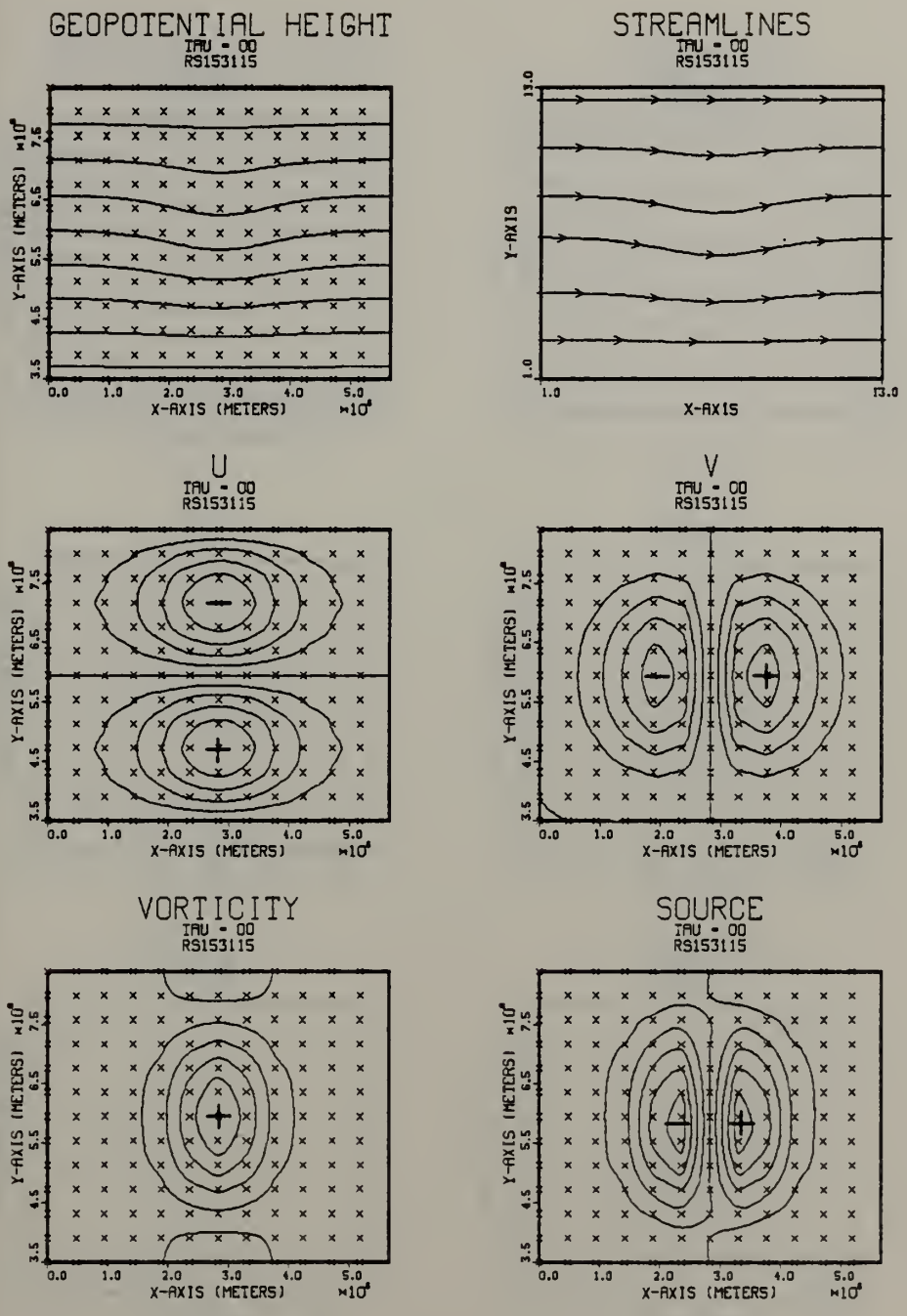


Fig. 32. Initial conditions for the GFEM model with a rectangular subdivision and source term added to the continuity equation. Resolution is low and uniform for a 2.5 m/s perturbation. Contour intervals are 600 $m^2/s^2$ for geopotential height, .5 m/s for u and v, $.2 \times 10^{-5}$ $s^{-1}$ for vorticity and $.2 \times 10^{-6}$ $s^{-1}$ for source.

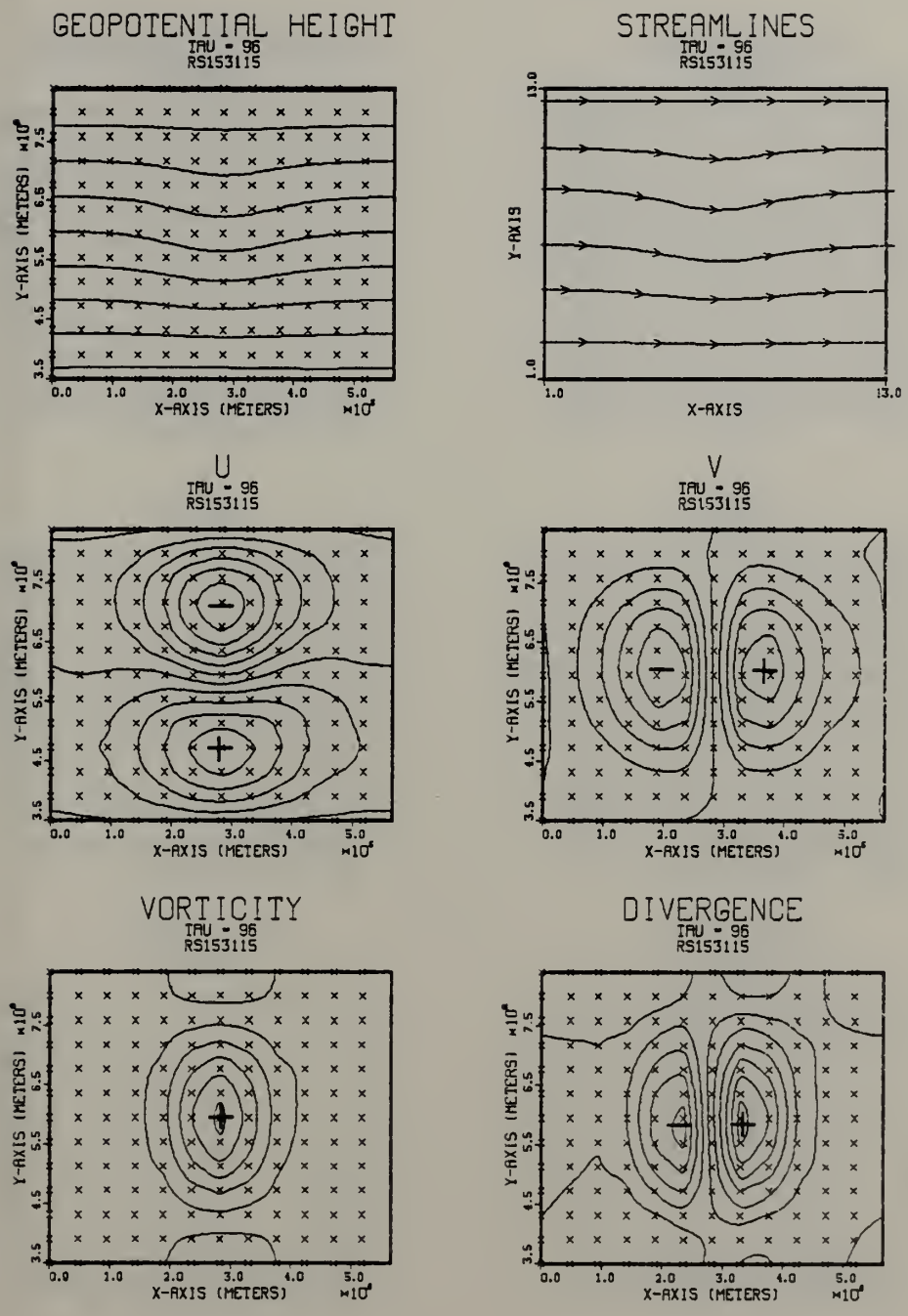


Fig. 33. As in Fig. 32 for a 96-h forecast.

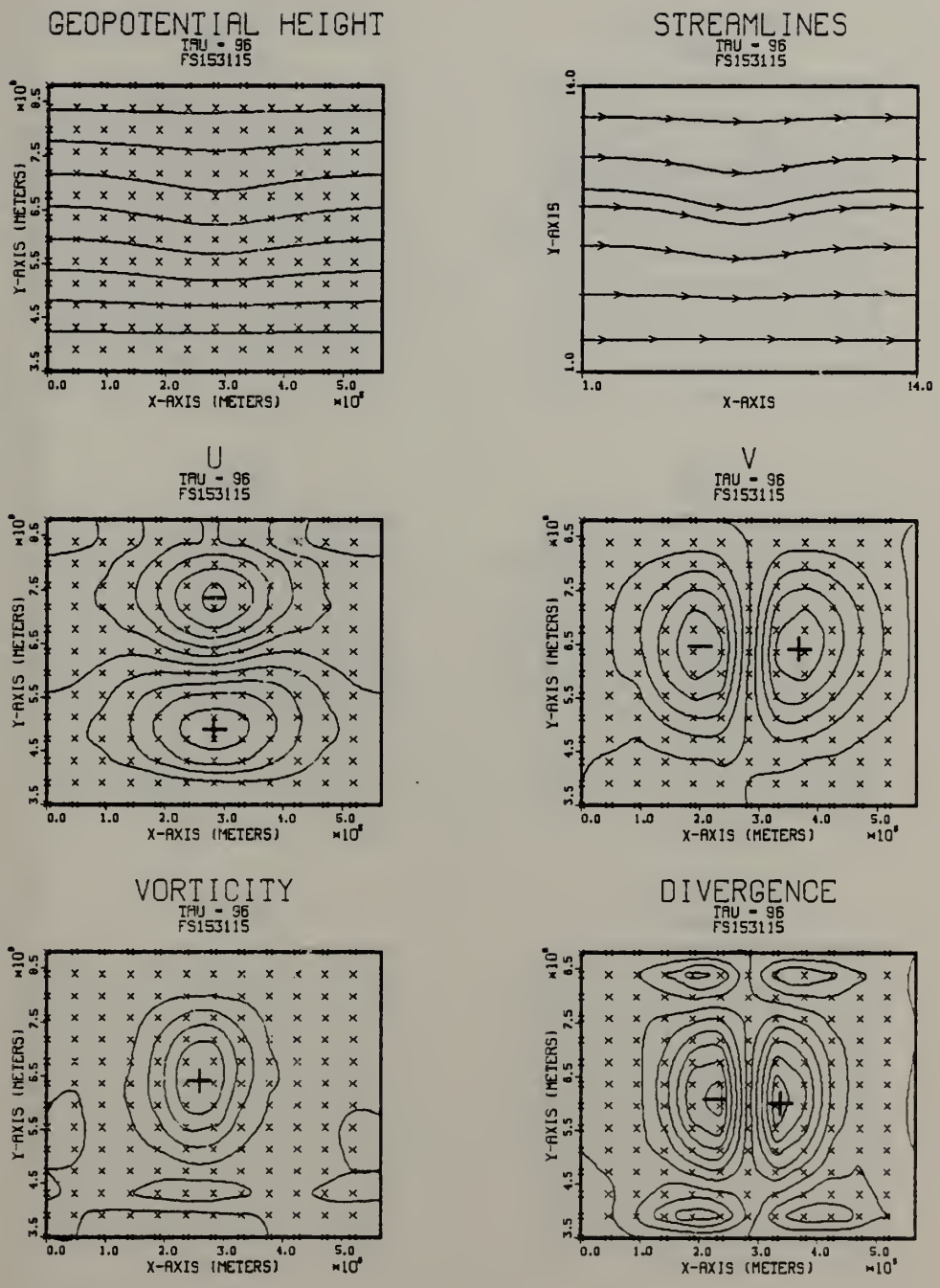


Fig. 34. As in Fig. 33 for a FDM model.

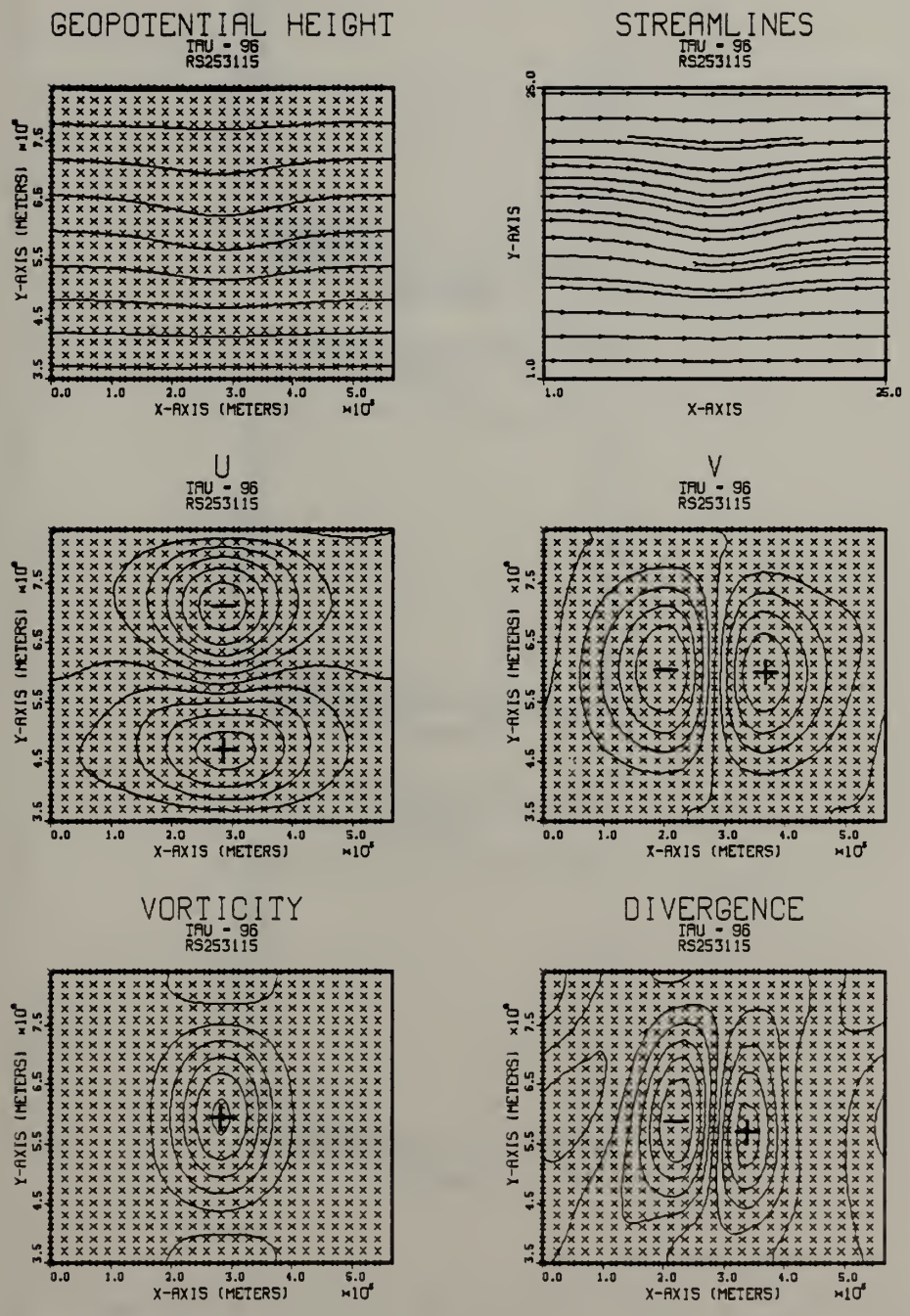


Fig. 35. As in Fig. 33 for a high resolution GFEM model.

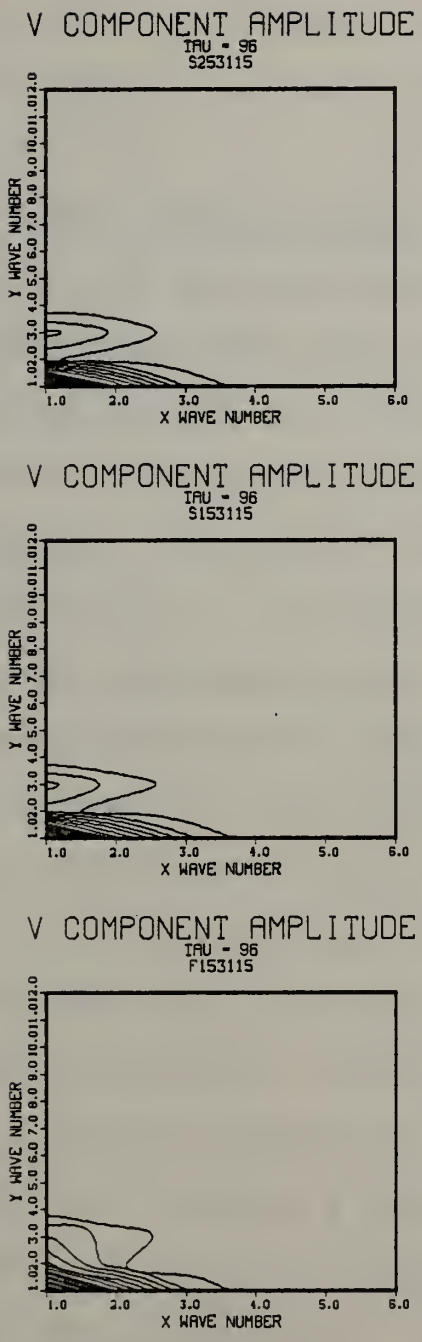


Fig. 36. V component amplitude as a function of x and y wave number at hour 96 for the high (S253115) and low (S153115) resolution GFEM models and the finite difference (F153115) model and perturbation = 2.5 m/s. Contour interval is .05 m/s.

even with this relatively linear case. For uniformity of comparison, similar ranges of x, y wave numbers will be shown in Figures 36 and 41.

2. Nonlinear Case - Variable Grids

Figures 37 and 38 are the initial and 96-h forecasts for the rectangular GFEM model with low resolution. The initial v field has a maximum of ±22.7 m/s across a separation of 4 increments, but most of the change occurs over 2 increments. The initial u field maximum/minimum is 35 m/s and -15 m/s. The source term as shown remains constant during the integrations. The adjustment process is evident when viewirg 96-h forecasts. The final v field has a maximum of 44.3 m/s, and a minimum of -38.0 m/s. The final u field has a maximum of 40.2 m/s and a minimum of -29.8 m/s. Figure 39 is the equivalent finite difference model forecast of Figure 38 and the marked differences in the forecast are readily apparent. The maximum final v component is 41.2 m/s and the minimum is -47.3 m/s. The maximum final u component is 50.6 m/s and the minimum value is -38.6 m/s. Figure 40 is the 96-h forecast for the rectangular high-resolution GFEM model. Comparisons of Figures 38, 39 and 40 show a convergence of the low-resolution GFEM version towards the high-resolution solution with a much poorer showing for the finite difference model. Figure 41 is a graph of v component amplitudes at hour 96 as a function of x and y wave numbers for the low and high

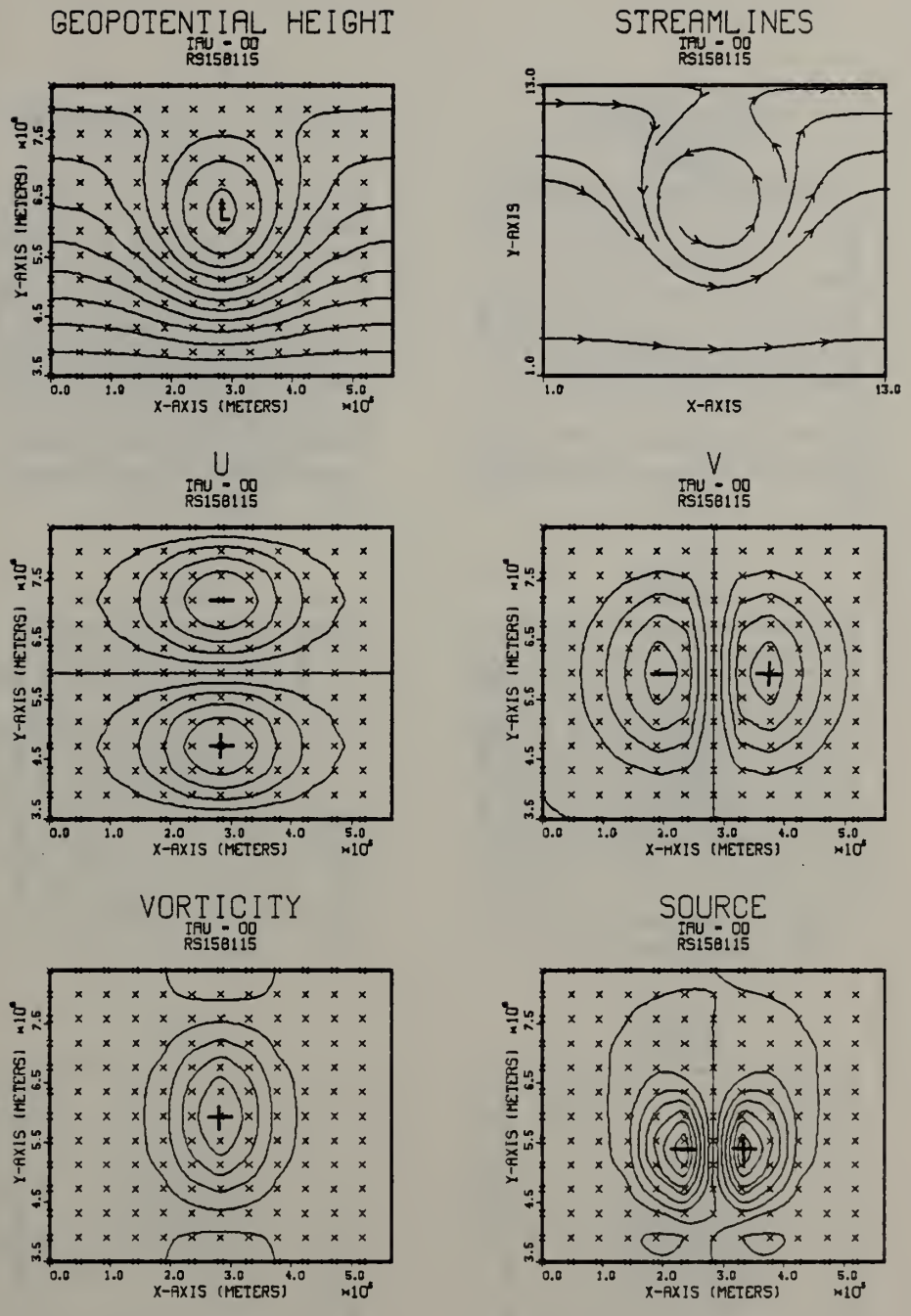


Fig. 37. As in Fig. 32 for a 25 m/s perturbation. Contour intervals are 600 $m^2/s^2$ for geopotential height, 5 m/s for u and v, $.2 \times 10^{-4}$ $s^{-1}$ for vorticity and $.2 \times 10^{-5}$ $s^{-1}$ for the source.

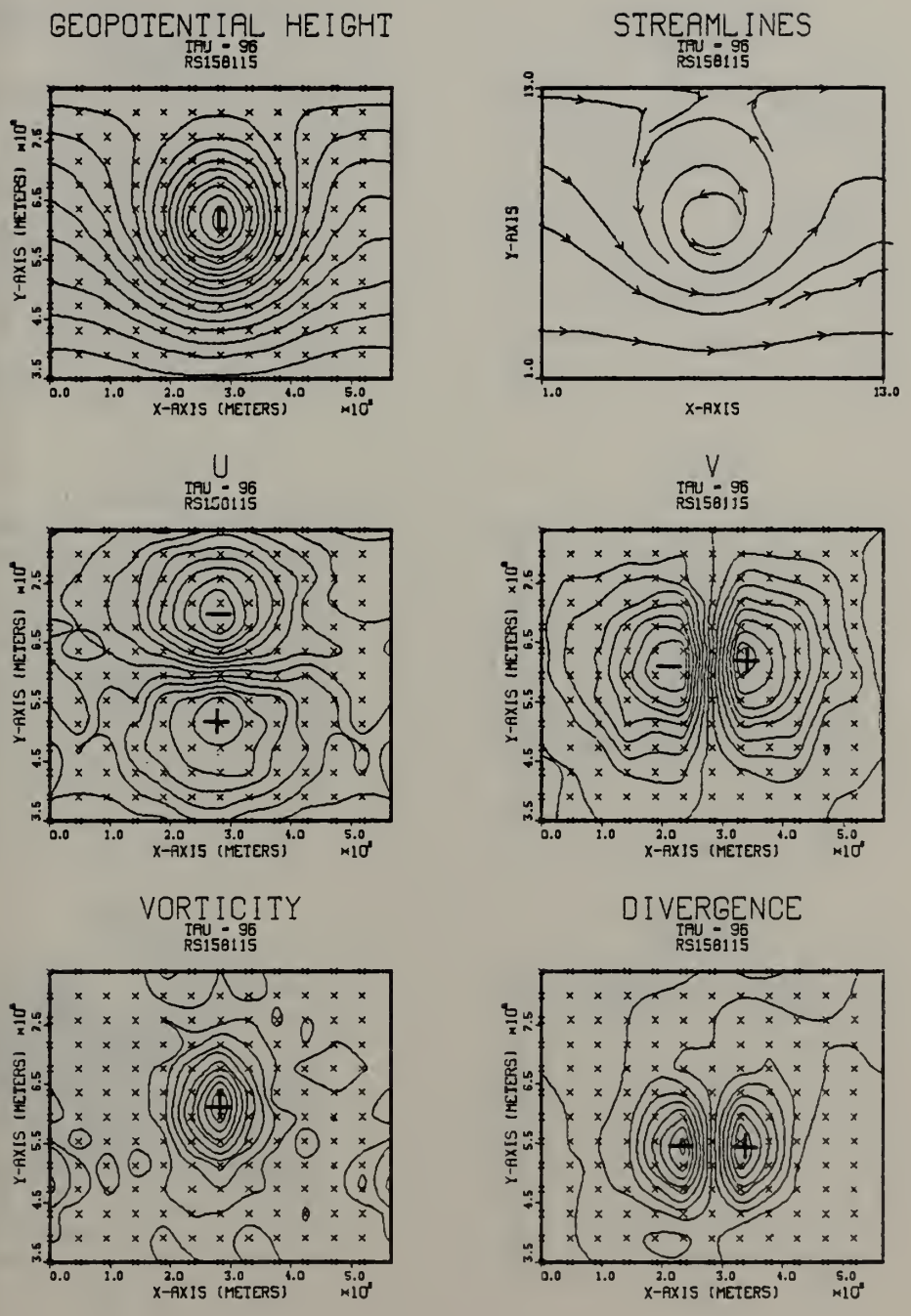


Fig. 38. As in Fig. 37 for a 96-h forecast.

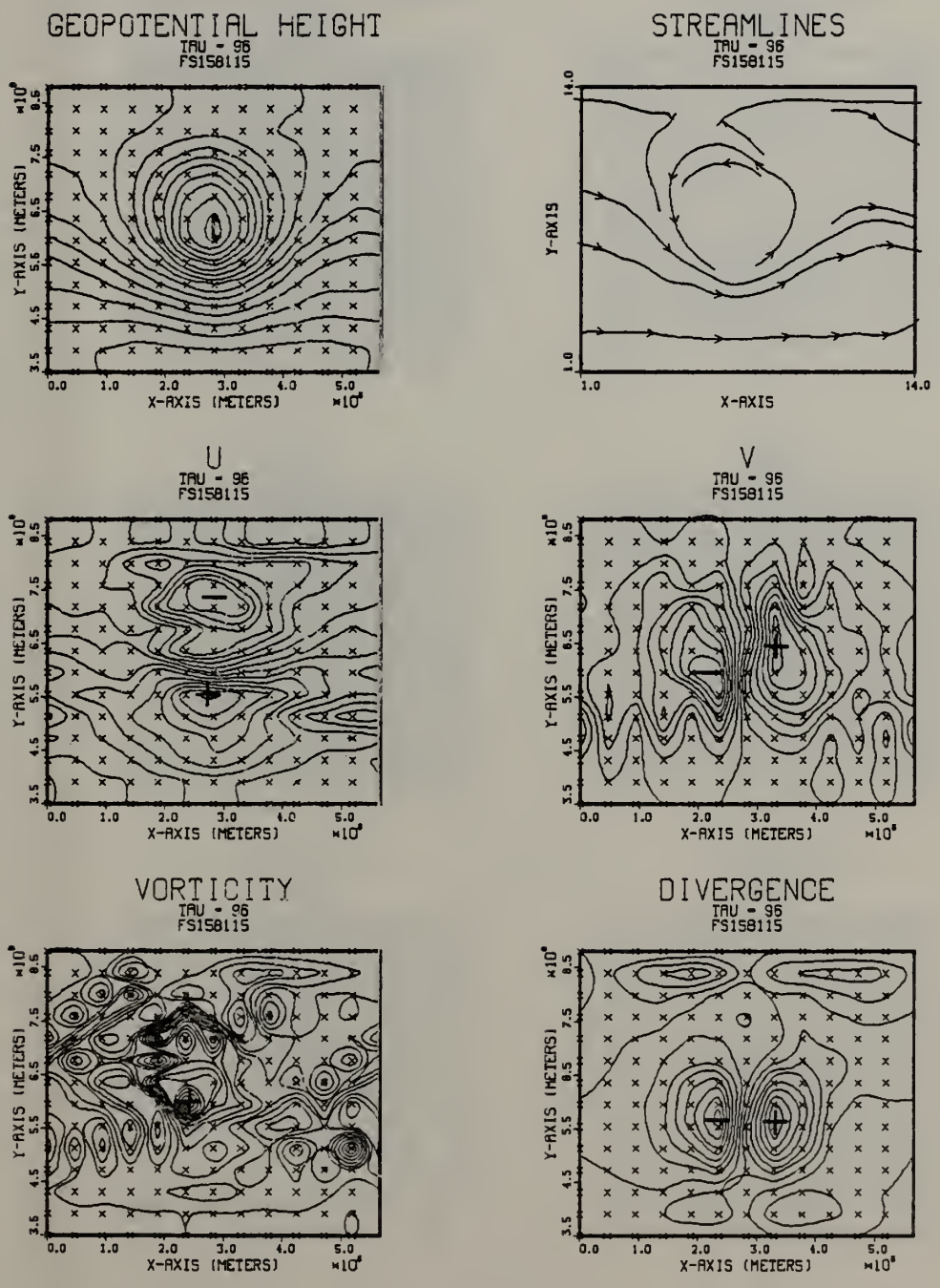


Fig. 39. As in Fig. 38 for a FDM model.

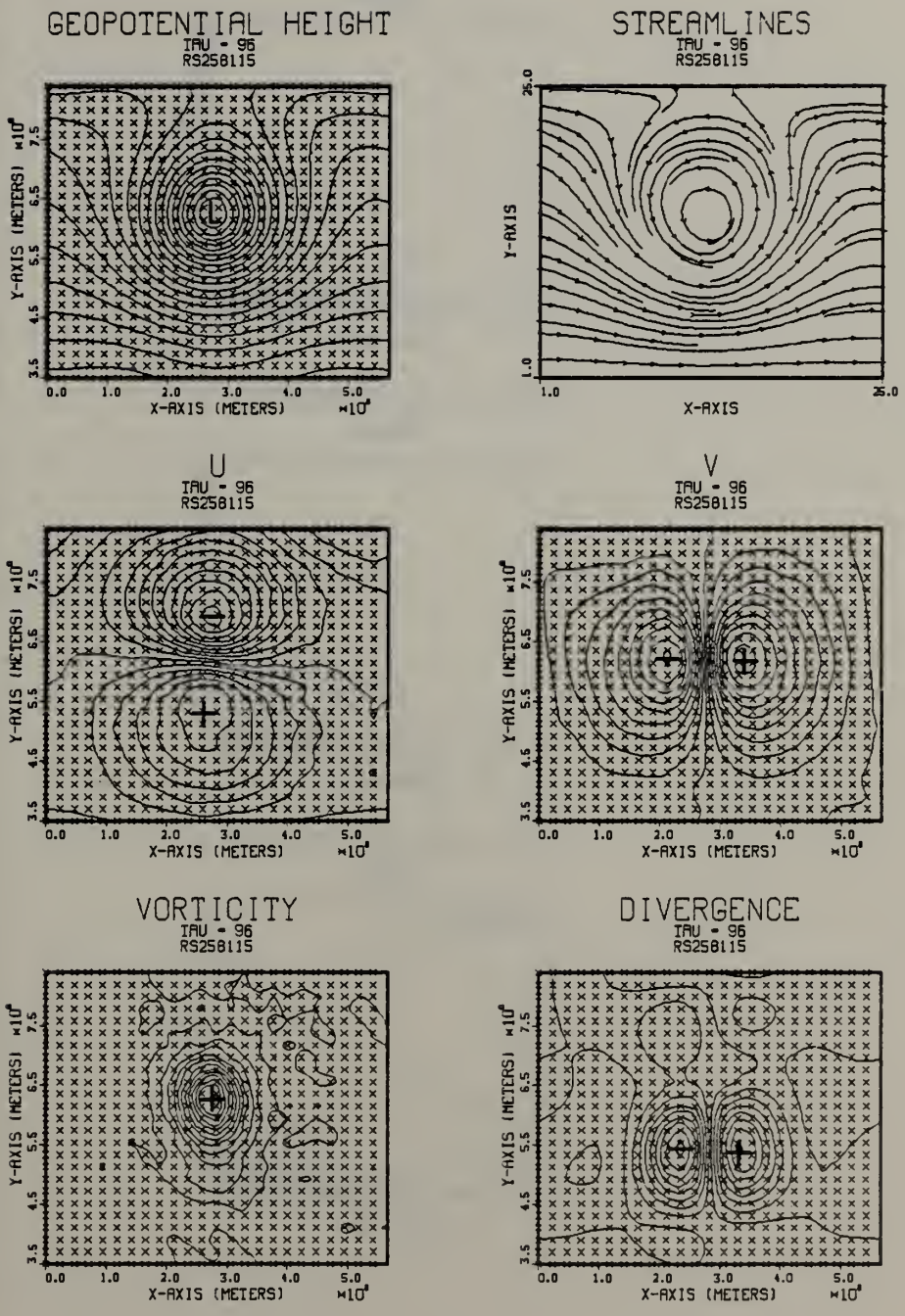


Fig. 40. As in Fig. 38 for a high resolution GFEM model.

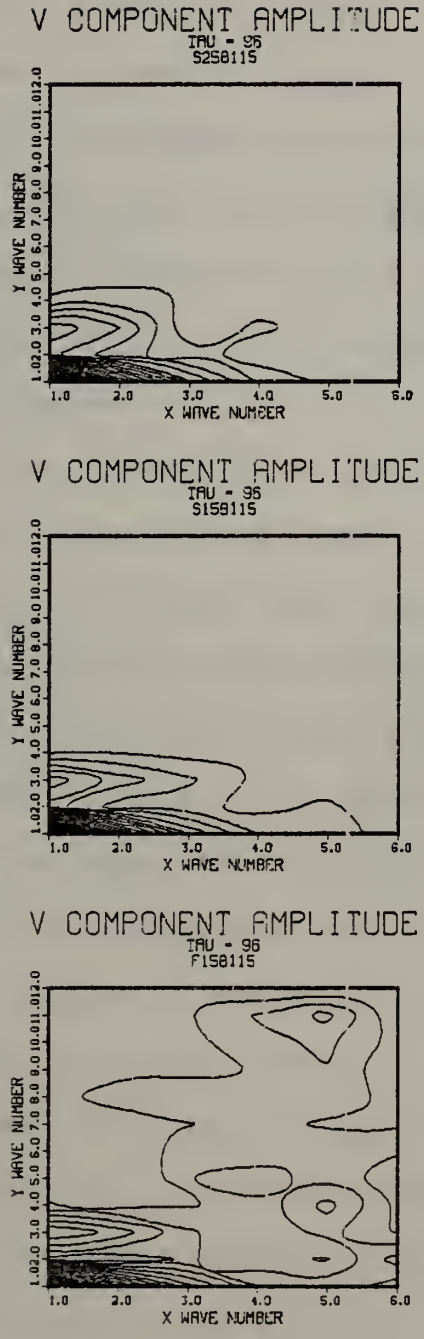


Fig. 41. V component amplitude as a function of x and y wave number at hour 96 for the high (S258115) and low (R158115) resolution GFEM models and the finite difference (F158115) model. Perturbation = 25.0 m/s. Contour interval is 0.5 m/s.

resolution and finite difference model. As in the linear case, there is strong agreement between the low and high resolution forecasts. The departure of the FDM from the control is readily apparent in this highly active case. The inability of the FDM to properly handle the nonlinear interactions manifest itself as large spurious amplitudes at high x and y wave numbers.

The relatively poor showing of the finite difference model for the forced cases shown so far can be improved, to a certain degree, by increasing the resolution. However, increased resolution requires more computational effort. Figure 42 is the 96-h forecast with a perturbation of 25.0 m/s for the FDM model. The initial conditions are identical to the nonlinear cases shown in Figure 37. The difference in the forecasts is the resolution where there are now 576 degrees of freedom (24X24). The 96-h forecast is certainly better than the 12X12 forecast. However, there is some high frequency noise in the forecast. Figure 43 is identical to Figure 42 except that there are 1296 degrees of freedom (36X36). The high frequency noise is readily apparent and is a manifestation of nonlinear aliasing. For this forced case the finite difference model is unable to achieve the same forecast as the low resolution GFEM model. This result will be amplified when a model with the same number of degrees of freedom as the low resolution model is employed but with a variable grid.

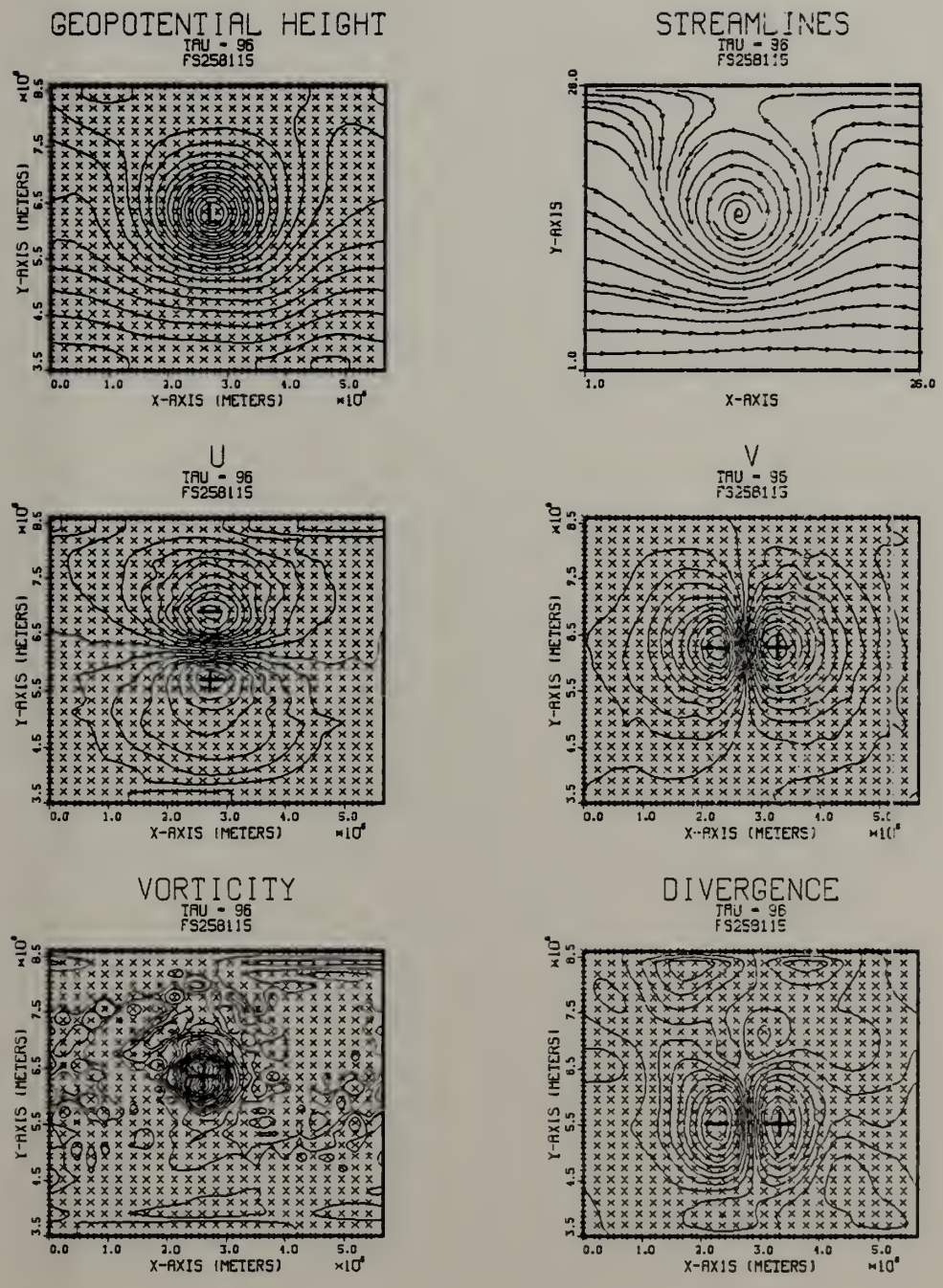


Fig. 42. As in Fig. 39 with 576 degrees of freedom.

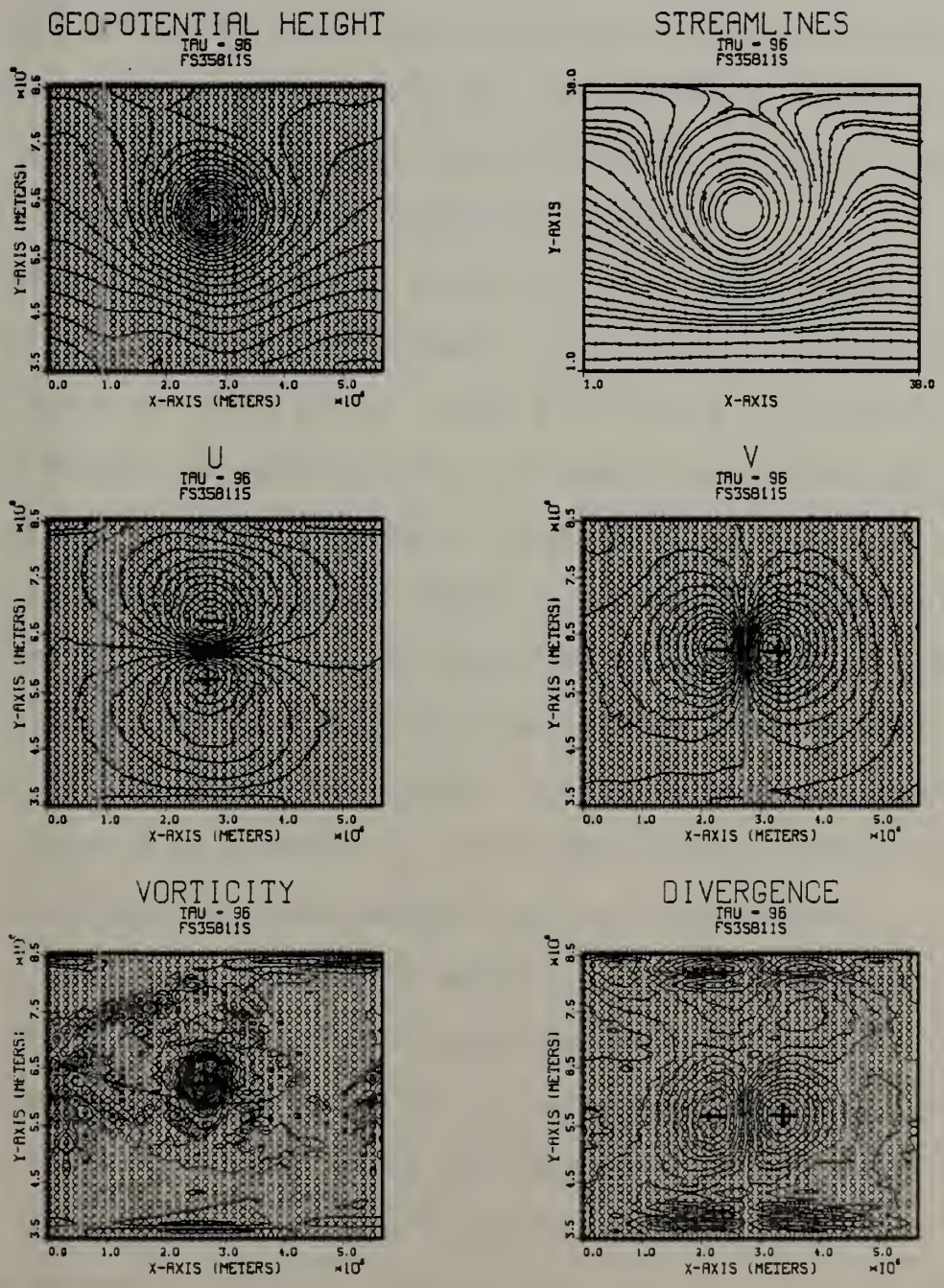


Fig. 43. As in Fig. 39 with 1296 degrees of freedom.

This comparison of the finite element and finite difference methods for the source term dramatically highlights the potential improvement when utilizing a Galerkin approach. Both graphical displays and harmonic analysis leave little doubt as to the superiority of the GFEM model over the equivalent finite difference model.

Adding an extra margin to the already established superiority can be accomplished by using the low-resolution model with a variable grid. Figure 44 is similar to the tests in Figure 38 except that a variable resolution grid (R = 2.0) was utilized. A 96-h forecast for a variable resolution grid (R = 3.0) is shown in Figure 45. Comparison of Figures 38, 40, 44, and 45 show the convergence of the low-resolution uniform solution towards the high resolution solution as the degree of variability is increased. Figure 46 is a graph of geopotential amplitudes at hour 96 versus y mode wave number (x wave number one) for the uniform, variable, and high resolution models. The R = 2.0 case better represents the control than the uniform low resolution forecast especially at low wave numbers. However, at wave number three and above all models have similar differences from the control.

The harmonic analysis demonstrates an improvement with increasing variability but is not conclusive. Another method to evaluate the improvement with increased variability is to look at the difference charts between the

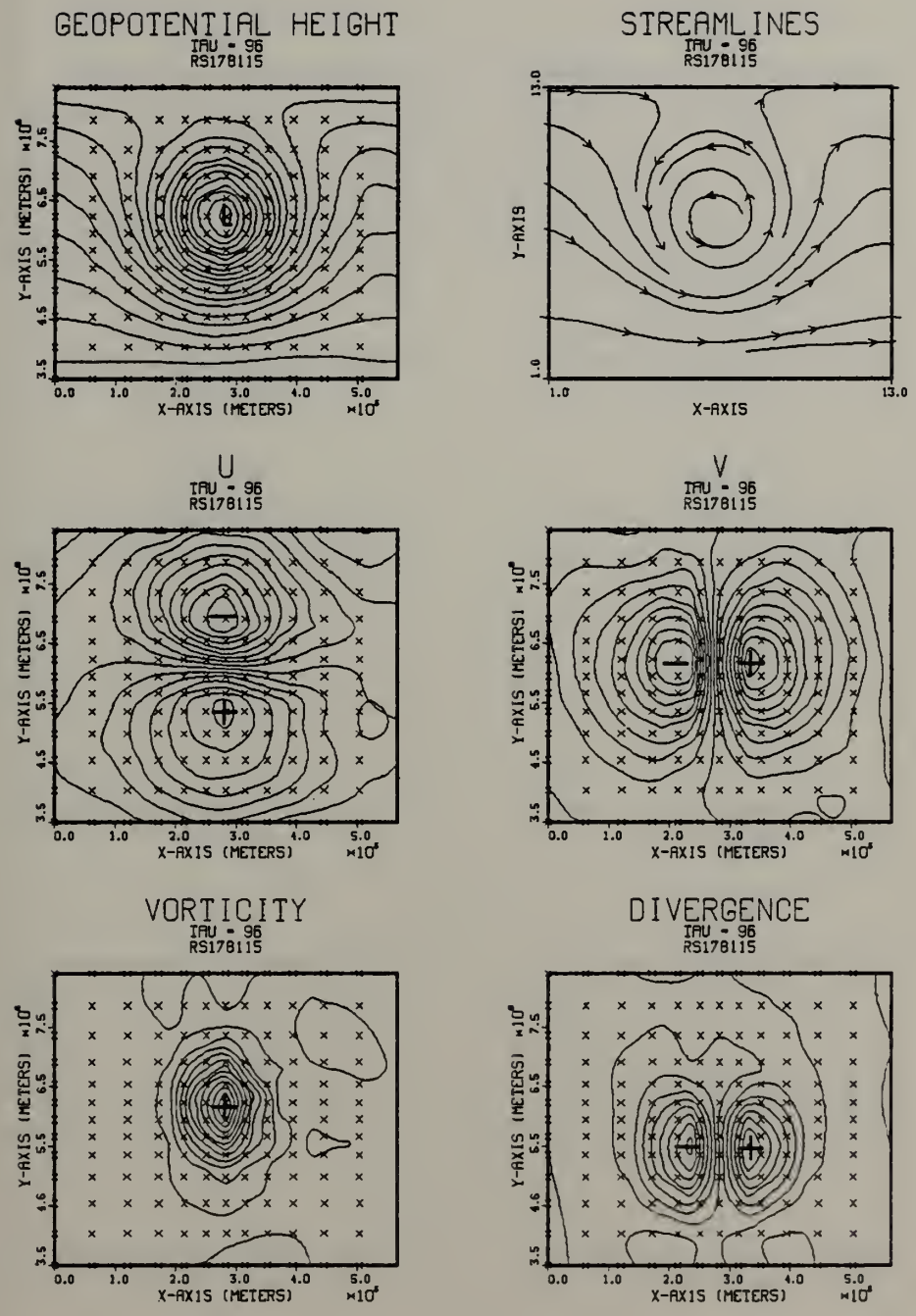


Fig. 44. As in Fig. 38 for R = 2.0.

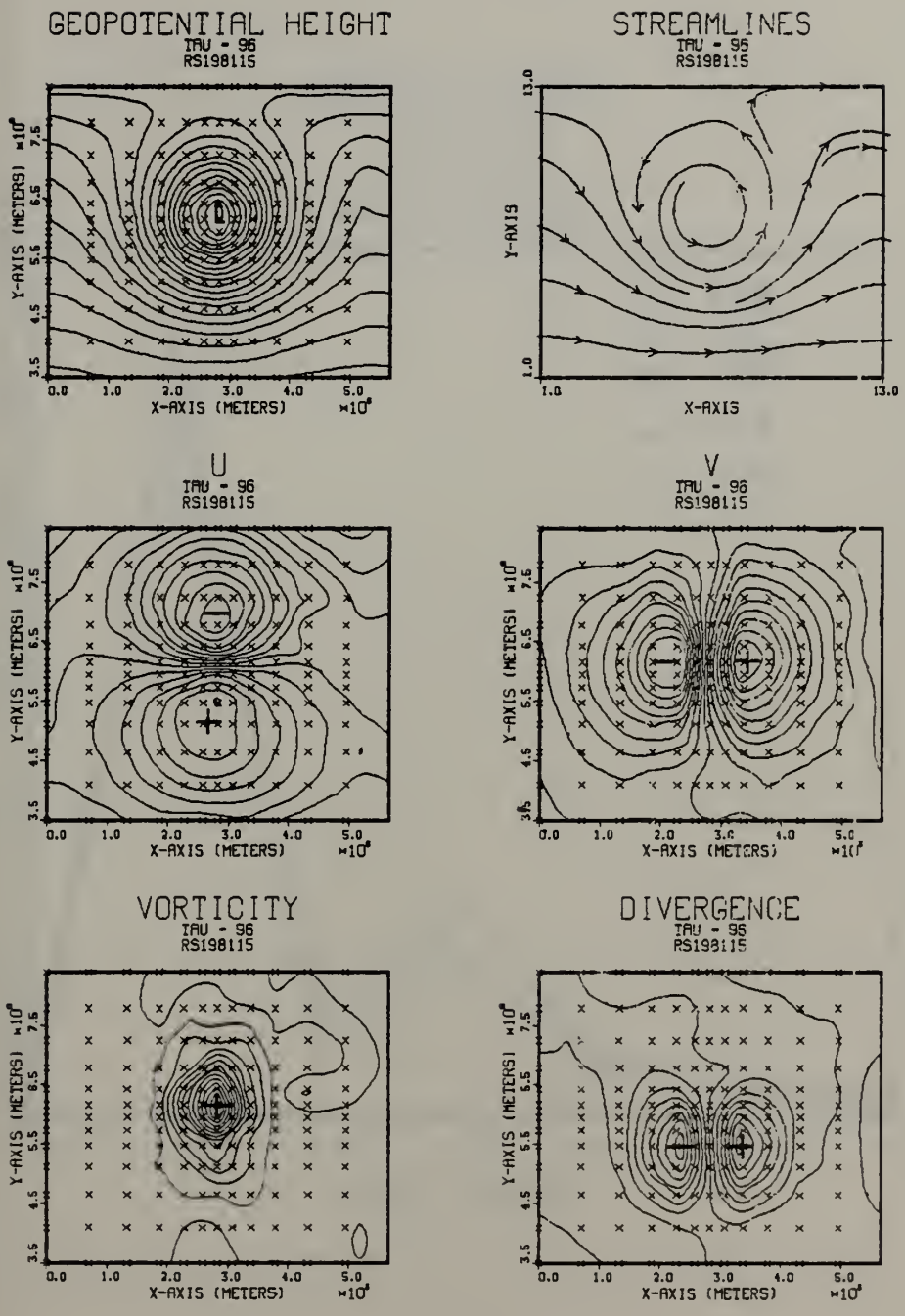


Fig. 45. As in Fig. 44 for R = 3.0.

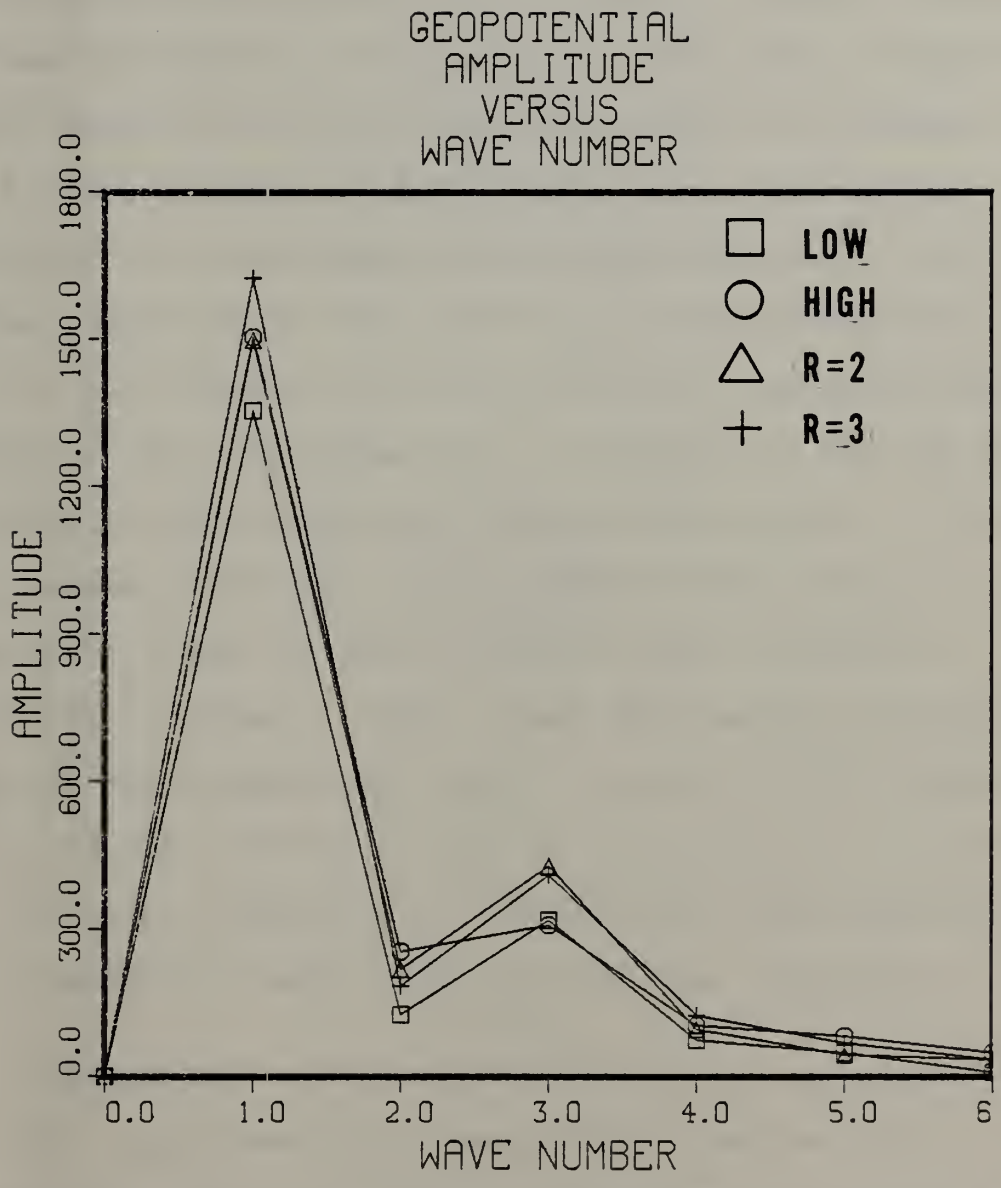


Fig. 46. Geopotential amplitude versus x wave number 1 and y waves 1-6 at hour 96 for the uniform, variable and high resolution GFEM models. Perturbation = 25.0 m/s.

control and each level of variability. The difference chart in Figure 47 is the control 96-h forecast (high resolution) minus the low-resolution 96-h forecast. Figure 47 shows a maximum difference in the center of the vortex. Figure 48 is the comparison of the high resolution 96-h forecast and the R = 2.0 variable grid 96-h forecast. The maximum difference has decreased from the uniform case. Figure 49 is the comparison of the high resolution 96-h forecast and the R = 3.0 variable grid 96-h forecast. The difference centers at the right-hand edge in Figures 47, 48 and 49 are a result of post processing interpolation errors. Although the maximum difference in the center of the vortex is greater in Figure 49 than Figure 48, the latitudinal difference gradient is less. Root mean square differences from the high resolution control are 652.2 $m^2/s^2$, 608.8 $m^2/s^2$ and 469.7 $m^2/s^2$ for the low resolution, R = 2.0 and R = 3.0 tests respectively. The forecasts have definitely been improved at each level of increased resolution.

## G. EXPERIMENT 4

This experiment will demonstrate a moving grid capability. Harrison (1973) demonstrated the use of a moving grid in his finite difference model. The inherent problems with moving finite difference models are abrupt changes in resolution causing spurious noise. The noise, unless damped, is magnified if left unattended every time a

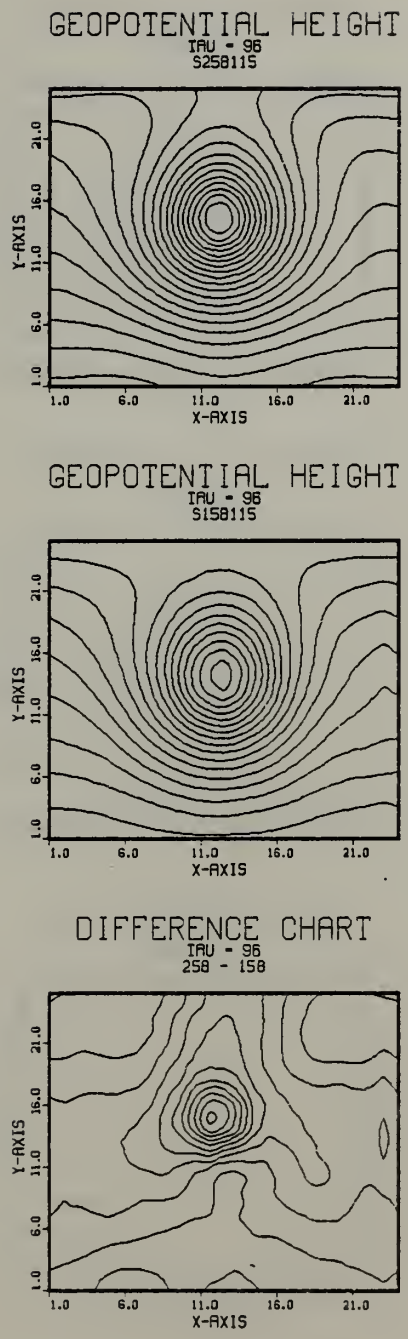


Fig. 47. Forecasts and difference charts at hour 96 for the uniform high (S258115) and low (S158115) resolution GFEM models. Perturbation = 25.0 m/s. Contour interval is 600 $m^2/s^2$ for the geopotential fields and 200 $m^2/s^2$ for the difference field.

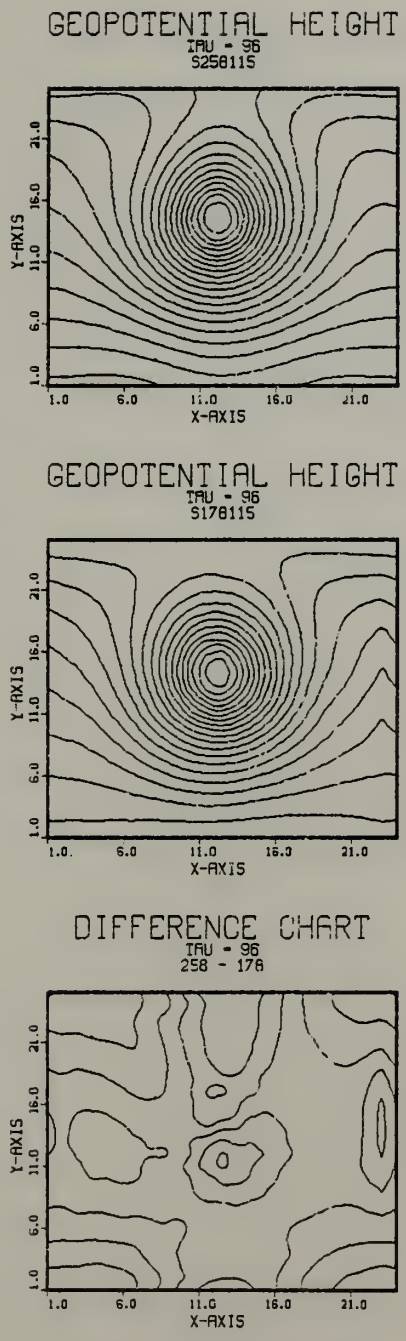


Fig. 48. As in Fig. 47 for the high resolution (S258115) and the variable (S178115) (R = 2.0) GFEM models.

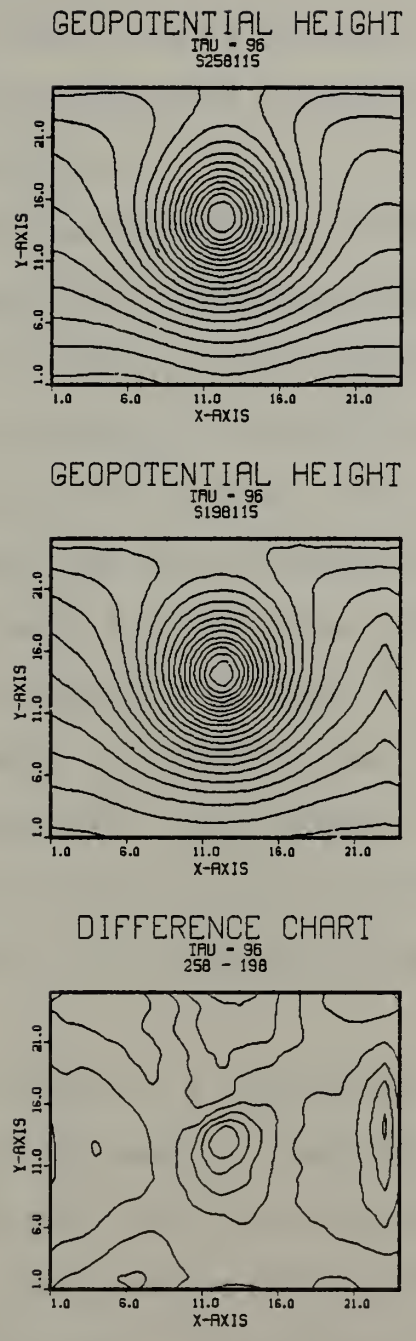


Fig. 49. As in Fig. 47 for the high resolution (S258115) and the variable (S198115) (R = 3.0) GFEM models.

grid moves. In a GFEM model there is a smooth transition into the fine grid area with no attendant noise. Therefore, moving the entire grid with the fine grid is simply a matter of accurate interpolation.

Three tests will be performed. First, uniform low and high resolution models will be integrated. These models will not use a moving grid. Then a model with the same degrees of freedom as the low-resolution model, but employing a moving, variable grid, will be run. The high-resolution model will act as the control. Identical initial conditions will be used for all three tests. These conditions are similar to those developed for experiment 3, except that the source term will be zero throughout the course of the integration. The initial conditions include a sharp trough with a relative vorticity maximum which is advected by the mean flow in the absence of any forcing (the source).

Of particular concern is the generation of noise incurred during grid movement. Therefore, a forecast of 96-h is made during which this grid moved eleven times. As previously stated, the model utilizes absolutely no diffusion, filters or friction. If spurious modes are excited during the movement of the grid, they will appear in the harmonic analysis.

The procedure of moving the finite element grid is achieved by displacing all the nodes one unit distance in the direction desired. This retains the relative distribution of the nodes and merely moves the entire grid as an entity. Ramifications of this approach are:

1. The areas of each element remain the same and the numerical quadrature coefficients for all the associated integrals do not have to be recomputed.

2. The unit distance moves should be the smallest grid increment; and

3. Direct solvers that utilize a preprocessing procedure based on the grid distribution will not require the preprocessing to be recomputed after each move.

The most important aspect of moving the grid is to accurately interpolate the new field values for the new grid point position. In this dissertation a standard International Mathematics and Statistical Library's (IMSL) bi-cubic spline interpolating routine was employed. The movement will occur only in the x direction and, therefore, a one-dimensional interpolator suffices. The interpolator accommodates the periodic boundary condition. However, interpolators for non-periodic boundary conditions are available. The accuracy of the interpolator is exact at grid points for a uniform distribution. Initial experimentation verified that a field could be moved with no loss in accuracy for a uniform grid. Experiment 4 will test its capability to move a variable grid with R = 2.0.

## H. RESULTS 4

Figures 50 and 51 are the initial and 96-h forecasts for the uniform low-resolution model. The perturbation is 25.0 m/s, mean flow 10 m/s and mean depth 5 km. The initial divergence is a zero field but spins up through geostrophic adjustment. The northeast/southwest trough orientation is a manifestation of the nonlinear interactions occurring for this highly active perturbation. Figure 52 is the 96-h forecast for the uniform high-resolution model. The northeast/southwest trough orientation is evident in this forecast as well. Figure 53 is the 96-h forecast for the low-resolution, moving variable grid (R = 2.0) model.

Time steps were 4320s, 3085.7s and 3600s for the low, high and variable models, respectively. The variable model took 95 full time steps and two half steps during the 96-h forecast. The half steps are required only to start the model to obtain the N and N+1 time levels in the leapfrog time stepping. The grid moved 11 times during the forecast at time steps 8, 16, 24, 32, 40, 48, 56, 64, 72, 80 and 88.

The x axis origin in Figure 53 is 3530 km indicating eastward grid movement. The vortex is still in the fine mesh area. Additionally, there is no noise in the forecast fields. To reiterate a previous statement, there are no filters, diffusion or friction terms employed during this integration. Comparisons among Figures 51, 52 and 53 show

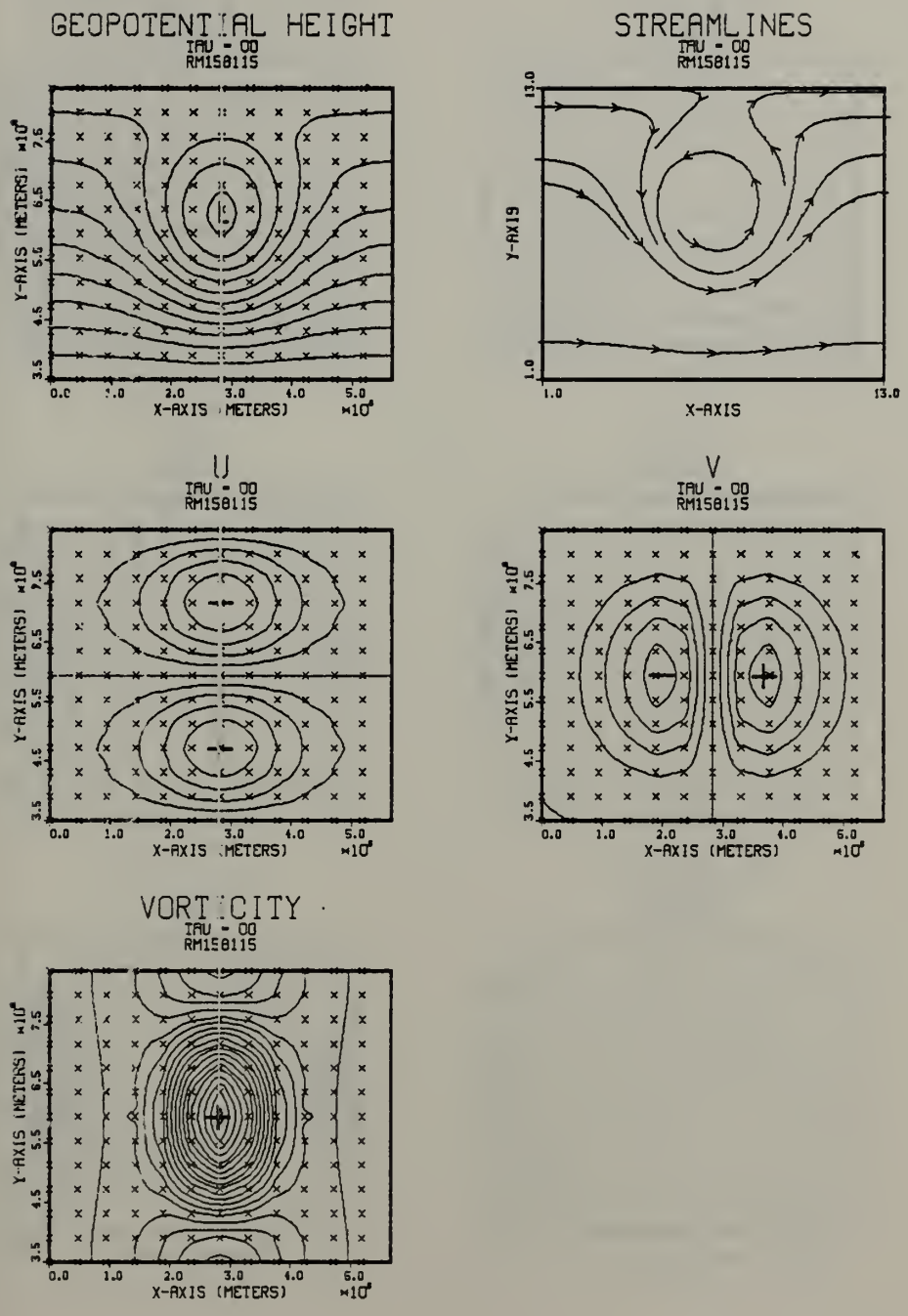


Fig. 50. As in Fig. 37 for a zero source term. Contour intervals are 600 $m^2/s^2$ for geopotential height, 5 m/s for u and v, $.6 \times 10^{-5} s^{-1}$ for vorticity and $.2 \times 10^{-5} s^{-1}$ for divergence.

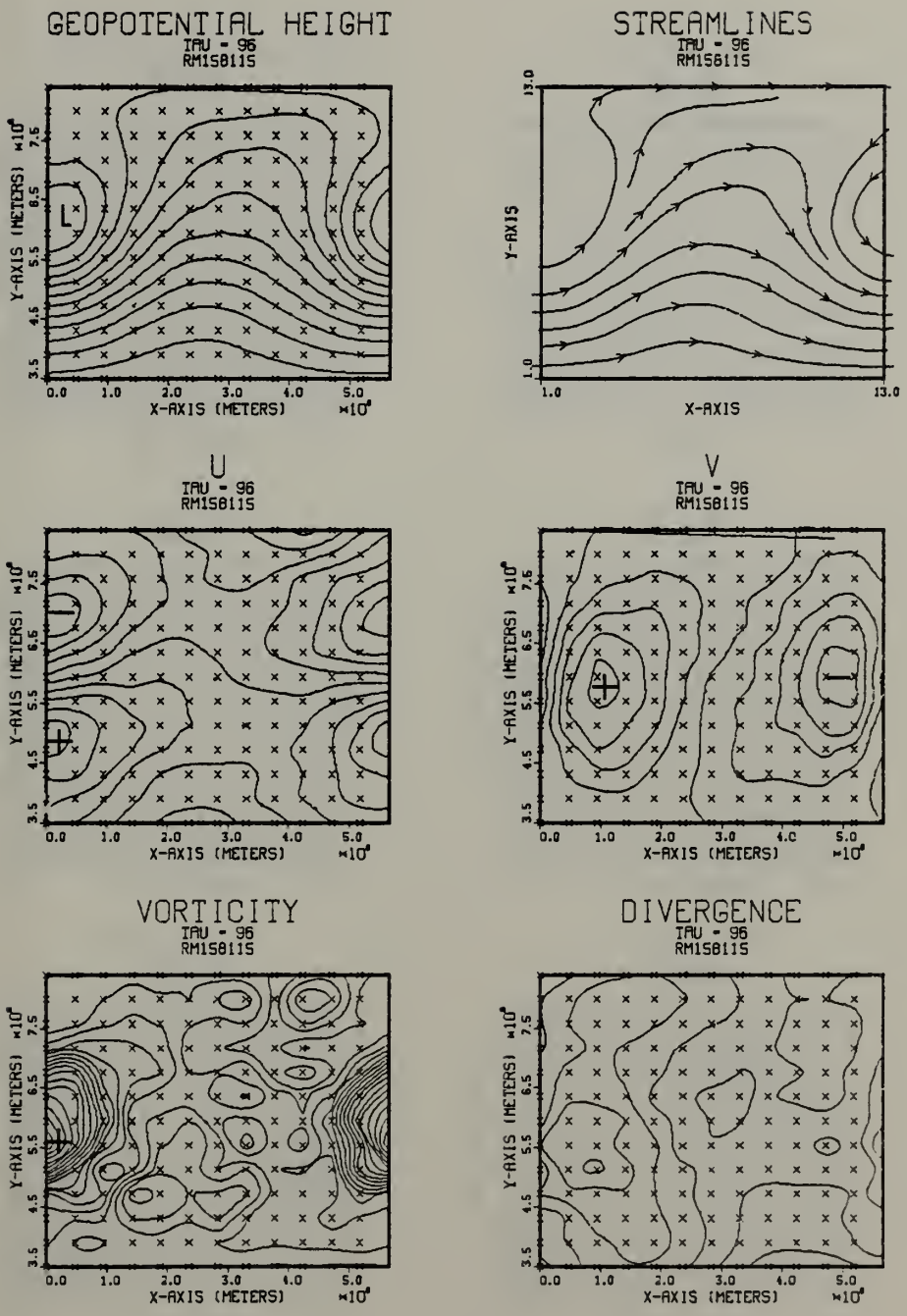


Fig. 51. As in Fig. 50 for a 96-h forecast.

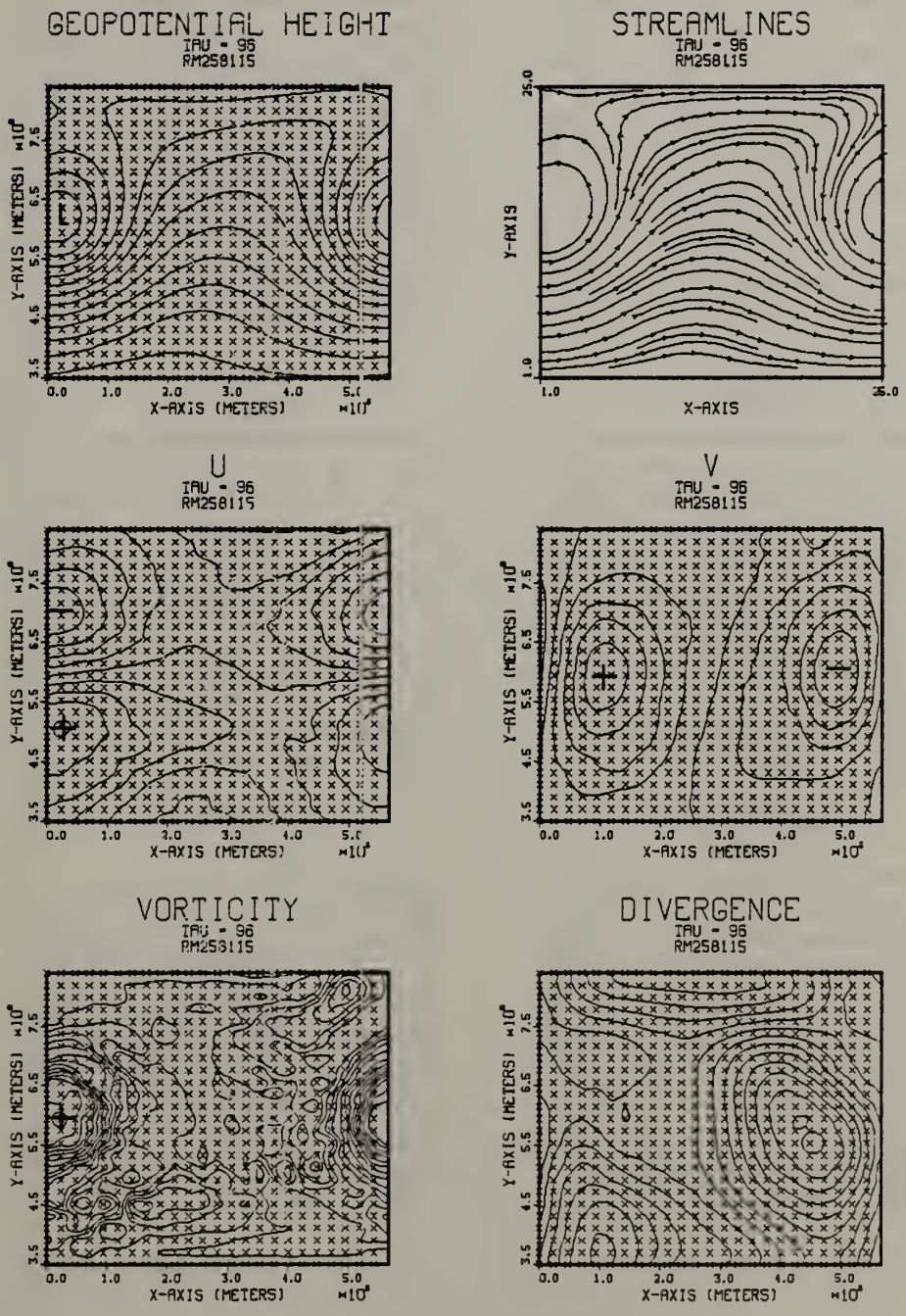


Fig. 52. As in Fig. 51 for a high resolution GFEM model.

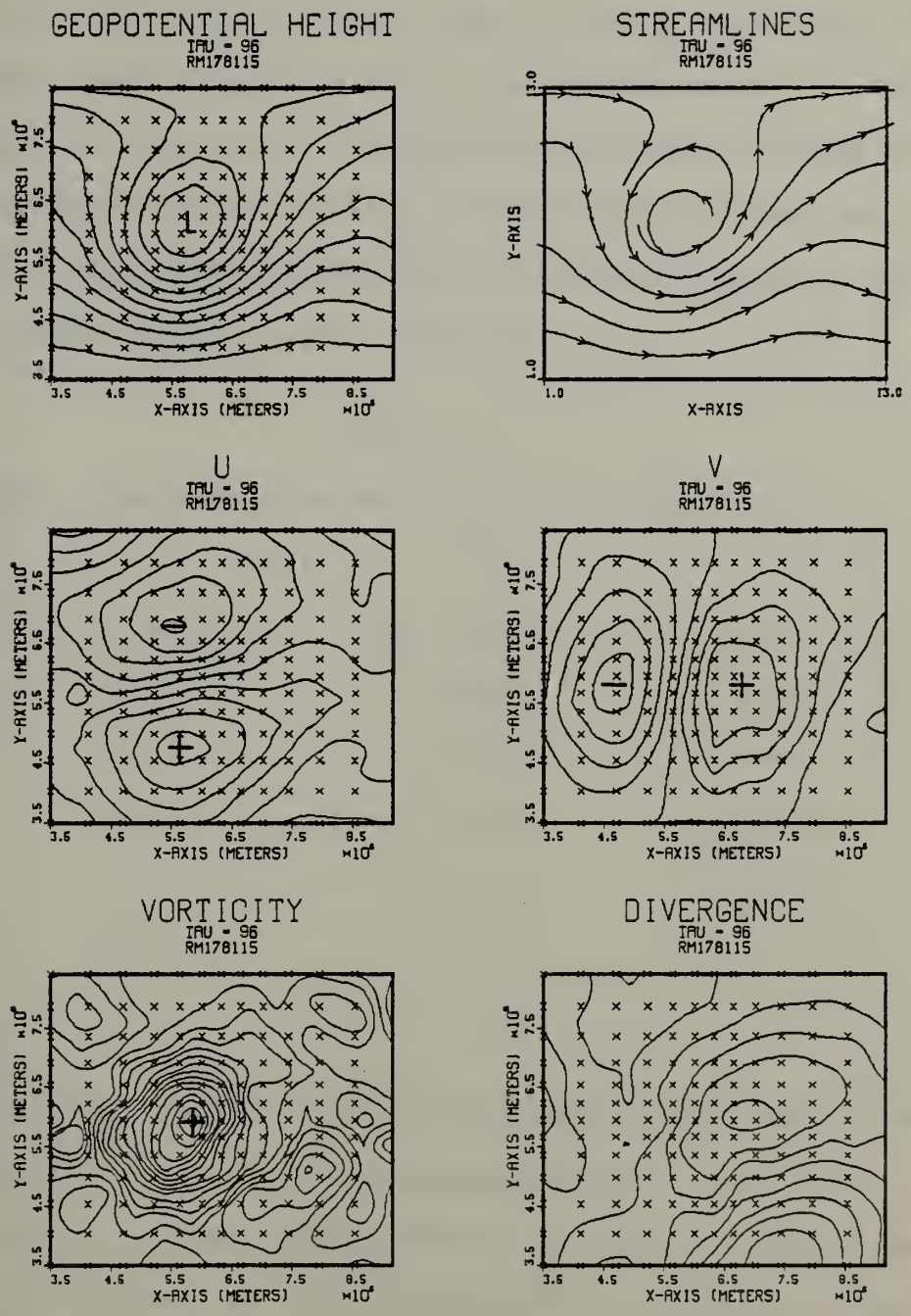


Fig. 53. As in Fig. 51 for a moving variable (R = 2.0), GFEM model. The x origin is different from Fig. 51 due to the movement of the grid during the forecast.

that the variable grid forecast more closely approaches the control than does the uniform low-resolution model. This is to be expected since the fine mesh area has been moved to coincide with the active region of the forecast domain.

Table 6 shows the geopotential harmonic analysis for the three models after a 96-h forecast.

TABLE 6

Harmonic Analysis (Geopotential) for Experiment 4

Units are $m^2/s^2$

| Wave | Low Resolution | High Resolution | Moving Grid |
|---|---|---|---|
| 1 | 876.1 | 904.7 | 850.0 |
| 2 | 167.4 | 152.9 | 146.6 |
| 3 | 122.5 | 176.9 | 159.6 |
| 4 | 54.7 | 39.0 | 39.0 |
| 5 | 20.3 | 10.2 | 9.6 |
| 6 | 5.1 | 7.6 | 7.3 |

Comparisons of the higher wave number amplitudes show almost identical amplitudes in y modes four, five and six for the moving case and high-resolution uniform case. The amplitude in y mode six indicates that the movement of the grid has not generated unwanted noise. The overall improvement for the moving case is a result of the finer grid's ability to better resolve the small-scale interactions occurring.

# VI. SUMMARY AND RECOMMENDATIONS

Numerical weather prediction requires that the equations governing atmospheric flow be solved numerically. These flows cover a large range of scales. Classical modeling schemes have successfully forecast the longer scales and improvements are being sought for the smaller scales.

In this dissertation, the GFEM has been employed for the shallow-water equations in a channel domain. The differentiated form of the equations on an unstaggered finite element grid with a semi-implicit time scheme has been utilized. An equivalent finite difference model representing the conventional approach has also been utilized. Analytic initial conditions representing simple atmospheric waves and a more complex source term have been used to test the different models.

The hypothesis of this dissertation is that the GFEM is a viable option for numerical weather prediction. The theoretical foundation of the GFEM leads to a minimization of the error between the actual equations and their approximation. This minimization implies a basis for expected improvement in forecast capabilities. Three features were addressed to support that hypothesis. First, alternatives for variable grids were investigated. Second, forcing near

the smallest grid scale determined if the GFEM model resolved the smaller scales better than a finite difference counterpart. Finally, a proof of concept for the ability to move the grid was demonstrated. Each task adds to the usability of the GFEM and illuminates the well-rounded potential that it contains.

First, the ease with which the method allows variable grids was demonstrated. In all cases, no numerical techniques were employed to damp or filter any field. The grid refinement obtained when using a rectangular subdivision was more attractive than with a triangular subdivision. It allowed refinement to be easily obtained with increased accuracy from the higher order polynomial and decreased computational effort due to reduced operation counts. Additionally, it was shown that the geometry of the triangular elements greatly influences the problem. Furthermore unless specific constraints are enforced, the boundary conditions would not be satisfied.

Second, the ability of the GFEM to resolve atmospheric phenomena occurring near the scale of the smallest grid-length was shown. A small-scale steady state solution was cast into a source required for that solution. Integrations showed that the GFEM model resolved the small-scale forcing admirably and far exceeded the performance of an equivalent finite difference model. Even when the resolution of the

finite difference model was doubled and tripled, it could not match the performance of the low-resolution variable grid GFEM model. The responsiveness of the GFEM model near the smallest resolvable grid length clearly demonstrates that the variable grid concept is worth the computational effort.

Finally, the concept of moving the variable grid was demonstrated. The ability to resolve a small-scale phenomenon is a tremendous asset to the GFEM. The ability to move the grid with the atmospheric phenomena further enhances its usefulness.

Throughout this dissertation the GFEM model has demonstrated desirable characteristics. It has conservative properties. It propagates atmospheric waves better than an equivalent finite difference model. It allows variable-resolution grids and responds better than an equivalent finite difference model near the smallest gridlength. Moving grids can be achieved with no apparent noise generation. It can utilize direct solvers and is a natural choice for vectorization on large computers. It truly is a viable option for simulation of atmospheric flows.

The success of this dissertation mandates further research. The next logical step would be a baroclinic model. Completion of a baroclinic model should allow its application as a regional model. Additionally, different

basis functions could be employed for the vertical discretization, such as solutions to the vertical structure equation. For the moving variable-resolution grid, further research into two-dimensional movement is required. The proof of concept in this dissertation of one-dimensional movement can logically be extended to two dimensions. Upon completion of two-dimensional movement, an operational forecast capability for tropical cyclones should be investigated. The superior small-scale response of the GFEM indicates potential increase in skill for both regional and tropical cyclone/hurricane prediction.

# APPENDIX A

## STABILITY ANALYSIS

A one-dimensional linear analysis of the forecast equations will be presented. The analysis was obtained through personal communication with Dr. Andrew Staniforth (Recherche en Prevision Numerique). The primitive form of the forecast equations and a semi-implicit time scheme will be analyzed, because the results are identical for the vorticity/divergence form. The one-dimensional equations with a mean flow $\bar{U}$ are

$$\frac{\partial u}{\partial t} + \frac{\partial \phi}{\partial x} = - \bar{U} \frac{\partial u}{\partial x} + fv \qquad (A\text{-}1)$$

$$\frac{\partial v}{\partial t} = - \bar{U} \frac{\partial v}{\partial x} - fu \qquad (A\text{-}2)$$

$$\frac{\partial \phi}{\partial t} + \Phi \frac{\partial u}{\partial x} = - \bar{U} \frac{\partial \phi}{\partial x} \qquad (A\text{-}3)$$

Time derivatives are evaluated with a centered time differencing and the other terms on the left-hand side are averaged between time levels $(t + \Delta t)$ and $(t - \Delta t)$. Equations (A-1), (A-2) and (A-3) become

$$\frac{u(x,t+\Delta t) - u(x,t-\Delta t)}{2\Delta t} + \frac{1}{2}\left[\frac{(\phi(x+\Delta x,t+\Delta t) - \phi(x-\Delta x,t+\Delta t)}{2\Delta x}\right.$$

$$\left. + \frac{(\phi(x+\Delta x,t-\Delta t) - \phi(x-\Delta x,t-\Delta t)}{2\Delta x}\right] = - \bar{U}\left[\frac{u(x+\Delta x,t) - u(x-\Delta x,t)}{2\Delta x}\right]$$

$$+ f\, v(x,t) \qquad (A\text{-}4)$$

$$\frac{v(x,t+\Delta t) - v(x,t-\Delta t)}{2\Delta t} = -\bar{U}\left[\frac{v(x+\Delta x,t) - v(x-\Delta x,t)}{2\Delta x}\right]$$

$$- f\,u(x,t) \qquad \text{(A-5)}$$

$$\frac{\phi(x,t+\Delta t) - \phi(x,t-\Delta t)}{2\Delta t} + \frac{\Phi}{2}\left[\frac{(u(x+\Delta x,t+\Delta t) - u(x-\Delta x,t+\Delta t)}{2\Delta x}\right.$$

$$\left. + \frac{(u(x+\Delta x,t-\Delta t) - u(x-\Delta x,t-\Delta t))}{2\Delta x}\right] = -\bar{U}\left(\frac{\phi(x+\Delta x,t) - \phi(x-\Delta x,t)}{2\Delta x}\right) \qquad \text{(A-6)}$$

Assuming that a function, F, can be expressed as

$$F(x,t) = F' e^{i(kx + wt)} \qquad \text{(A-7)}$$

then

$$\frac{F(x,t+\Delta t) - F(x,t-\Delta t)}{2\Delta t} = \frac{iF'}{\Delta t}\sin(w\Delta t)e^{i(kx + wt)} \qquad \text{(A-8)}$$

$$\frac{F(x,t+\Delta t) + F(x,t-\Delta t)}{2} = F' \cos(w\Delta t)e^{i(kx + wt)} \qquad \text{(A-9)}$$

Equations (A-4), (A-5), and (A-6) become, after substitution,

$$\frac{isu'}{\Delta t} - fv' + ik'c\phi' = 0 \qquad \text{(A-10)}$$

$$fu' + \frac{isv'}{\Delta t} = 0 \qquad \text{(A-11)}$$

$$ik'c\Phi u' + \frac{is\phi'}{\Delta t} = 0 \qquad \text{(A-12)}$$

where $s = \sin w\Delta t + k'u\Delta t$, $c = \cos w\Delta t$ and $k' = \sin \frac{k\Delta x}{\Delta x}$. The determinant of the system of equations (A-10), (A-11) and (A-12) when set equal to zero yields

$$\frac{s}{\Delta t}\left[\frac{s^2}{\Delta t^2} - (f^2 + k'^2 c^2 \Phi)\right] = 0 \qquad \text{(A-13)}$$

The roots are s=0 and

$$s^2 = (f\Delta t)^2 + c^2(k\Delta t)^2 \, \Phi \qquad \text{(A-14)}$$

The roots of this second order equation when requiring w to be real yield the stability criterion

$$\Delta t \leq \frac{1}{\left|\frac{\bar{U}}{\Delta x}\right| + f} \qquad \text{(A-15)}$$

# APPENDIX B

## NUMERICAL QUADRATURE

Evaluation of the Galerkin integrals requires a fast, efficient method . Two different elements, triangles and rectangles, have been employed and the quadrature schemes for evaluation are presented here. In the first case, triangles, area coordinates are used. For the rectangles, integration formulas are based on an orthogonal axis transformation. In both cases, the integrals to be evaluated contain either products of basis functions, products of derivatives of basis functions, or a mixture of both.

Zienkiewicz (1971) developed the relationship between the Cartesian coordinates of a triangle and the area coordinates as

$$X = L_1X_1 + L_2X_2 + L_3X_3 \tag{B-1}$$

$$Y = L_1Y_1 + L_2Y_2 + L_3Y_3 \tag{B-2}$$

$$\underline{1} = L_1 + L_2 + L_3 \tag{B-3}$$

where $(x_1,y_1)$, $(x_2,y_2)$ and $(x_3,y_3)$ are the Cartesian coordinates of the triangle's vertices and $L_1$, $L_2$ and $L_3$ are the area coordinates. Here

$$L_1 = A_1/A \qquad L_2 = A_2/A \qquad L_3 = A_3/A$$

where $A_1$, $A_2$ and $A_3$ are shown in Figure 54 and A is the area of the entire triangle. He further shows that

$$\iint L_1^{\,a} L_2^{\,b} L_3^{\,c}\, dxdy = \frac{a!b!c!}{(a+b+c+2)!}\, 2A$$

The L's are the basis and test functions used during the approximating process. Figure 55 defines some necessary parameters for evaluation of the derivatives.

Equations B-1, B-2 and B-3 can be written in matrix form as

$$\begin{bmatrix} L_1 \\ L_2 \\ L_3 \end{bmatrix} = \frac{1}{2A} \begin{bmatrix} 2A & b_1 & a_1 \\ 2A & b_2 & a_2 \\ 2A & b_3 & a_3 \end{bmatrix} \begin{bmatrix} 1 \\ X \\ Y \end{bmatrix} \qquad \text{(B-5)}$$

Differentiation of Eq. (B-5) shows that

$$\frac{\partial}{\partial x} = \sum_{i=1}^{3} \frac{b_i}{2A} \frac{\partial}{\partial L_i} \qquad \text{(B-6)}$$

$$\frac{\partial}{\partial y} = \sum_{i=1}^{3} \frac{a_i}{2A} \frac{\partial}{\partial L_i} \qquad \text{(B-7)}$$

However, the derivative of the basis function with respect to the area coordinate is non-zero only where the basis function and area coordinate coincide. In fact, the non-zero value is one. Therefore, using $V_1$ as a basis function

$$\frac{\partial V_1}{\partial x} = \frac{b_1}{2A} \qquad \text{(B-8)}$$

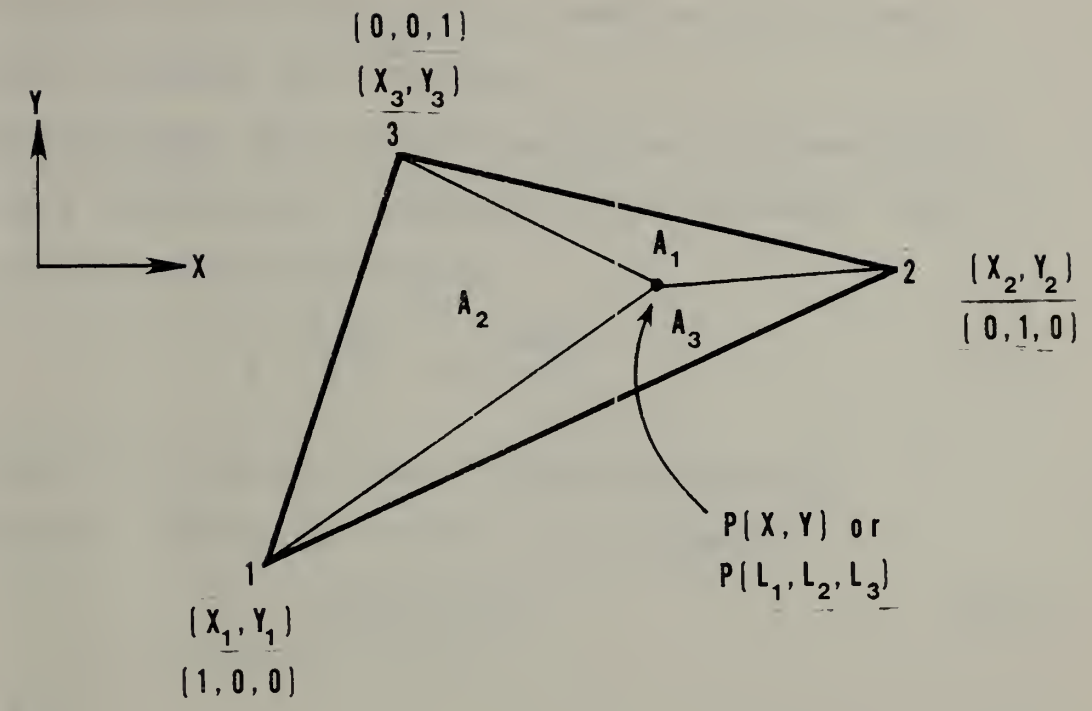


Fig. 54. Cartesian coordinates vs. natural coordinates.

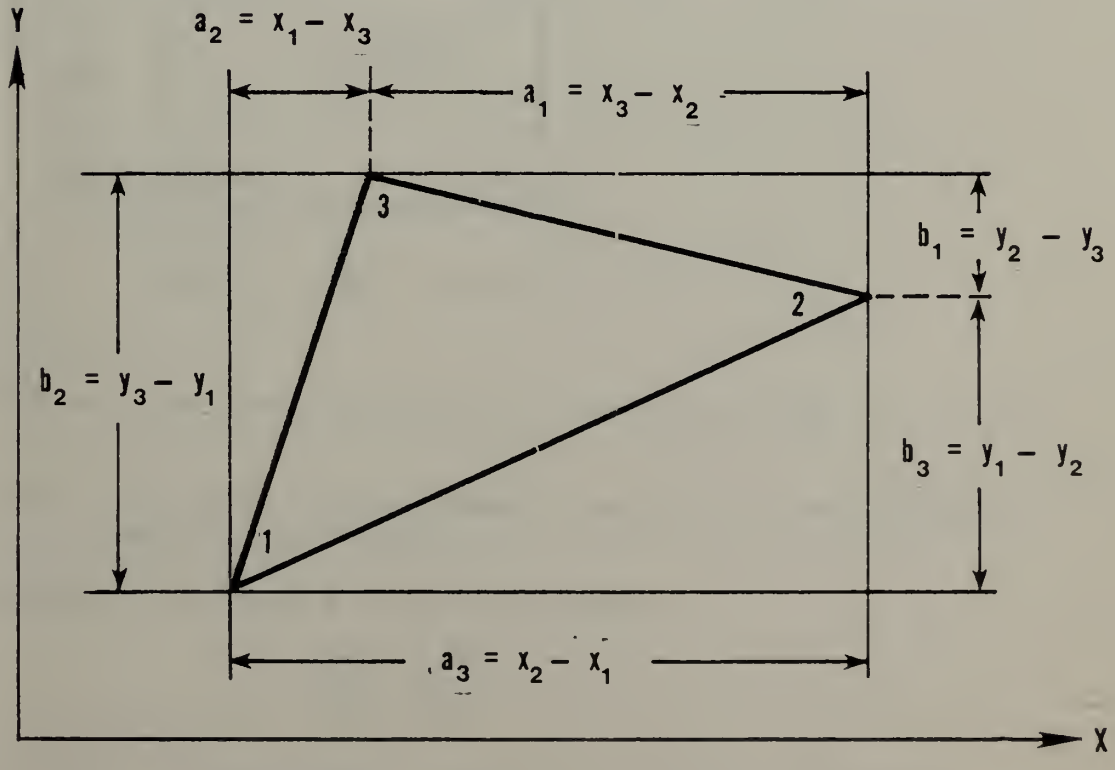


Fig. 55. Triangle definitions for area coordinates.

All integrals can be evaluated by combination of these quadrature formulas for triangles.

An orthogonal axis transformation will allow similar quadrature formulas for rectangles. The rectangle shown in Figure 56 can be transformed by

$$\zeta = \frac{x-x_o}{a} \qquad \eta = \frac{y-y_o}{b} \tag{B-9}$$

The values of $\zeta$ and $\eta$ at each corner are shown in parentheses. The basis function, $V_i$, becomes

$$V_i = \frac{(1+\zeta_i\zeta)(1+\eta_i\eta)}{4} \tag{B-10}$$

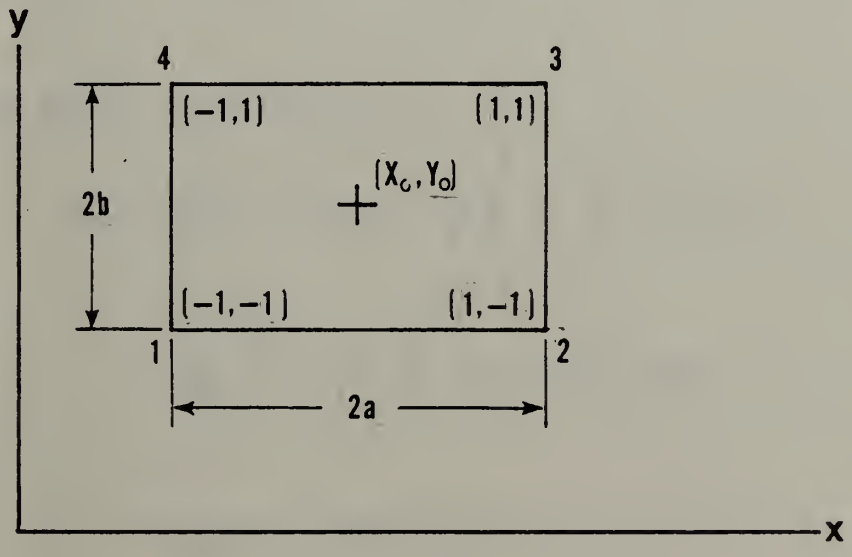


Fig. 56. Orthogonal axis transformation for rectangular integration formulas.

Derivatives of the basis function become

$$\frac{\partial V_i}{\partial x} = \frac{1}{a}\frac{\partial V_i}{\partial \zeta}$$

and

$$\frac{\partial V_i}{\partial y} = \frac{1}{b}\frac{\partial V_i}{\partial \eta} \tag{B-11}$$

By substituting and integrating, the 4 x 4 matrix with the interaction coefficients can be determined for a derivative or straight inner product. For instance, the straight inner product is

$$c_{ij} = \iint V_i V_j dxdy = ab \int_{-1}^{1}\int_{-1}^{1} V_i V_j \, d\zeta d\eta$$

$$= \frac{ab}{16} \int_{-1}^{1} (1+\zeta_i\zeta)(1+\zeta_j\zeta)d\zeta \int_{-1}^{1} (1+\eta_i r)(1+\eta_j\eta)d\eta$$

$$= \frac{ab}{16}(2+\frac{2}{3}\zeta_i\zeta_j)(2+\frac{2}{3}\eta_i\eta_j) \qquad \text{(B-12)}$$

and the mixed derivative is

$$d_{ij} = \iint \frac{\partial V_i}{\partial x} \frac{\partial V_j}{\partial x} dxdy = \frac{b}{a} \int_{-1}^{1}\int_{-1}^{1} \frac{\partial V_i}{\partial \zeta} \frac{\partial V_j}{\partial \zeta} d\zeta d\eta$$

$$= \frac{b}{16a} \int_{-1}^{1} \zeta_i\zeta_j d\zeta \int_{-1}^{1} (1+\eta_i\eta)(1+\eta_j\eta)d\eta$$

$$= \frac{b}{16a}(2\zeta_i\zeta_j)(2+\frac{2}{3}\eta_i\eta_j) \qquad \text{(B-13)}$$

These quadrature rules allow the evaluation of any integrals when using rectangles.

# LIST OF REFERENCES


Bathe, K. J., and E. L. Wilson, 1976: Numerical methods in finite element analysis. Prentice-Hall, Inc., 528 pp.

Cullen, M. J. P., 1974a: A finite element method for a non-linear initial value problem. J Inst Math Its Appl 13, 233-247.

_____, 1974b: Integrations of the primitive equations on a sphere using the finite element method. Q J R Meteorol Soc, 100, 555-562.

_____, 1979: The finite element method numerical methods used in atmospheric models, Vol. II Garp Publication Series Number 17, pp. 300-337.

_____, and C. D. Hall, 1979: Forecasting and general circulation results from finite element models. Q J R Meteorol Soc, 105, 571-592.

Haltiner, G.J., and R. T. Williams, 1980: Numerical prediction and dynamic meteorology. John Wiley & Sons, Inc., 477 pp.

Harrison, E. J., Jr., 1973: Three-dimensional numerical simulations of tropical systems utilizing nested finite grids. J Atmos Sci, 8, 1528-1543.

Hinsman, D. E., 1975: Application of a finite element method to the barotropic primitive equations. M.S. Thesis, Naval Postgraduate School, Monterey, California, 116 pp.

Kelley, R. G., and R. T. Williams, 1976: A finite element prediction model with variable element sizes. Naval Postgraduate School Report NPS-63WU76101, 1-109.

MacPherson, A. K., and M. H. Aksel, 1980: A study of frontogenesis using finite-element and finite-difference methods. Mon Wea Rev, 108, 1183-1196.

Older, M. E., 1981: A two-dimensional finite element advection model with variable resolution. M. S. Thesis, Naval Postgraduate School, Monterey, California, 84 pp.

Sasaki, Y. K., and J. N. Reddy, 1980: A comparison of stability and accuracy of some numerical models of two-dimensional circulation. Int J Numer Methods Eng, 16, 149-170.

Schoenstadt, A., 1980: A transfer function analysis of numerical schemes used to simulate geostrophic adjustment. Mon Wea Rev, 108, 1245-1259.

Staniforth, A. N., and H. L. Mitchell, 1977: A semi-implicit finite-element barotropic model. Mon Wea Rev, 105, 154-169.

_____, and R. W. Daley, 1977: A finite-element formulation for the vertical discretization of sigma-coordinate primitive equation models. Mon Wea Rev, 105, 1108-1118.

_____, and H. L. Mitchell, 1978: A variable resolution finite-element technique for regional forecasting with the primitive equations. Mon Wea Rev, 106, 439-447.

_____, and R. W. Daley, 1979: A baroclinic finite-element model for regional forecasting with the primitive equations. Mon Wea Rev, 107, 107-121.

Williams, R. T., and A. L. Schoenstadt, 1980: Formulation of efficient finite element prediction models. Naval Postgraduate School Report NPS63-80-011, 1-37.

_____, 1981: On the formulation of finite element prediction models. Mon Wea Rev, 109, 463-466.

_____, and O. C. Zienkiewicz, 1981: Improved finite-element forms for the shallow-water wave equations. Int J Numer Methods Fluids, 1, 81-97.

Woodward, E. T., 1981: Development of improved finite element formulation for shallow water equations. M.S. Thesis, U.S. Naval Postgraduate School, Monterey, California, 168 pp.

Zienkiewicz, O. C., 1971: The finite element method in engineering science. McGraw-Hill, 521 pp.

INITIAL DISTRIBUTION LIST

| | | No. Copies |
|---|---|---|
| 1. | Defense Technical Information Center<br>Cameron Station<br>Alexandria, VA 22314 | 2 |
| 2. | Library, Code 0142<br>Naval Postgraduate School<br>Monterey, CA 93940 | 2 |
| 3. | Chairman (Code 63Rd)<br>Department of Meteorology<br>Naval Postgraduate School<br>Monterey, CA 93940 | 1 |
| 4. | Director<br>Naval Oceanography Division<br>Naval Observatory<br>34th and Massachusetts Avenue, NW<br>Washington, D.C. 20390 | 1 |
| 5. | Commander<br>Naval Oceanography Command<br>NSTL Station<br>Bay St. Louis, MS 39522 | 1 |
| 6. | Commanding Officer<br>Fleet Numerical Oceanography Center<br>Monterey, CA 93940 | 1 |
| 7. | Commanding Officer<br>Naval Environmental Prediction<br>Research Facility<br>Monterey, CA 93940 | 1 |
| 8. | Chief of Naval Research<br>800 N. Quincy Street<br>Arlington, VA 22217 | 1 |
| 9. | Professor R. T. Williams (Code 63Wu)<br>Department of Meteorology<br>Naval Postgraduate School<br>Monterey, CA 93940 | 3 |

10. CDR Donald E. Hinsman — 5
Naval Environmental Prediction
Research Facility
Monterey, CA 93940

11. Professor R. L. Elsberry (Code 63Es) — 1
Department of Meteorology
Naval Postgraduate School
Monterey, CA 93940

12. Associate Professor R. L. Haney (Code 63Hy) — 1
Department of Meteorology
Naval Postgraduate School
Monterey, CA 93940

13. Associate Professor A. L. Schoenstadt — 1
(Code 53Zh)
Department of Mathematics
Naval Postgraduate School
Monterey, CA 93940

14. Professor R. E. Newton (Code 69Ne) — 1
Department of Mechanical Engineering
Naval Postgraduate School
Monterey, CA 93940

15. Associate Professor C. P. Chang (Code 63Cp) — 1
Department of Meteorology
Naval Postgraduate School
Monterey, CA 93940

16. CAPT John L. Hayes, Code 63 — 1
Department of Meteorology
Naval Postgraduate School
Monterey, CA 93940

17. Dr. David A. Archer — 1
Douglas DuPont Rachford, Inc.
8150 Chevy Chase
Houston, TX 77027

18. Dr. M. J. P. Cullen — 1
Meteorological Office
Bracknell, Berks, United Kingdom

19. Dr. Robert L. Lee — 1
Atmospheric and Geophysical Science Division
University of California
P. O. Box 808
Livermore, CA 94550

20. Professor A. K. MacPherson 1
Lehigh University
Department of Mechanical Engineering
Bethlehem, PA 18015

21. Dr. N. A. Phillips 1
National Meteorological Center/NOAA
World Weather Building
Washington, DC 20233

22. Professor I. Salinas, Code 69Zc 1
Department of Mechanical Engineering
Naval Postgraduate School
Monterey, CA 93940

23. Dr. Y. Sasaki 1
Department of Meteorology
University of Oklahoma
Norman, OK 73069

24. Dr. Andrew Staniforth 1
Recherce-en-Prevision Numerique
West Isle Office Tower, 5 ieme etage
2121 route Trans-Canada
Dorval, Quebec H9P1J3, Canada

25. Professor O. C. Zienkiewicz 1
Head of Civil Engineering Department
Applied Science Building
Singleton Park
Swansea SA2 8PP
United Kingdom

26. Dr. F. J. Winninghoff, Code 63 1
Department of Meteorology
Naval Postgraduate School
Monterey, California 93940

27. Dr. Paul Budgell, Code 68 1
Department of Oceanography
Naval Postgraduate School
Monterey, CA 93940

28. Dr. Eugene S. Takle 1
Department of Climatology and Meteorology
310 Curtiss Hall
Iowa State University
Ames, Iowa 50011

200603

Thesis
H5733
c.1 Hinsman
Numerical simulation of atmospheric flow on variable grids using the Galerkin finite element method.